Universität Rostock
Fakultät für Informatik und Elektrotechnik
Institut für Nachrichtentechnik

Master-Arbeit

Analysis and Optimisation of Medium Gain X-Yagi Antennas for the EISCAT_3D 237.5 MHz Incoherent Scatter Radar Active Array

vorgelegt von
Toralf Renkwitz
Matrikel 1201026

Betreuer:
Prof. Dr.-Ing. habil. Tobias Weber (Universität Rostock)
Dr. Gudmund Wannberg (EISCAT Scientific Association)
Dr. Werner Singer (Leibniz-Institut für Atmosphärenphysik an der Universität Rostock)

Bearbeitungszeitraum 25.10.2007 – 25.04.2008

M. Sc. Eng. Project

Analysis and Optimisation of Medium Gain X-Yagi Antennas for the EISCAT_3D 237.5 MHz Incoherent Scatter Radar Active Array

Description of the problem

A phased array is subject to the principle of superposition, that is, its radiation pattern is the product of the interferometer pattern defined by the array geometry and the element pattern defined by the characteristics of the individual radiating element. As in optical gratings, multiple interferometer lobes pointing in different directions may form simultaneously once the element-to-element spacing is increased beyond some critical distance. The extra lobes are termed grating lobes and are normally unwanted. Assuming that the array elements are isotropic radiators, grating-lobe-free pointing out to 40° requires that the element-to-element spacing is no greater than 0.6 wavelengths.

Using a simple, physically realisable element antenna, e.g. two crossed dipoles above a ground-plane, the spacing can be increased to about 0.65 wavelengths without introducing severe grating lobes; as the main lobe is tilted beyond approximately 35° the grating lobes beginning to appear at 90° zenith angle are suppressed to some extent by the sharp dip in the element antenna pattern at 90°.

The active part of the EISCAT_3D incoherent scatter research radar system now being planned for eventual deployment in northern Scandinavia will be a very large phased array. Many of the target performance specifications for this array are very challenging. This is particularly true of the beam steering and pointing. To accommodate user requests, it must be possible to steer the main beam freely within a 40° cone centred on the vertical, while at the same time not running into grating lobe problems. At the same time, the array should be designed to provide maximum gain at an elevation angle = 77° and azimuth 180°, that is, along the local terrestrial magnetic field line, which is an important reference direction for the electrodynamics of the ionospheric plasma being studied.

As the envisaged array will comprise in the order of 10000 transmit/receive units, each comprising a medium-gain antenna, a 600-watt transmitter and a direct-digitising receiver, it is very important for logistical and cost reasons to keep the number of units as low as possible without impairing the basic performance of the overall system. As an example, if the unit-to-unit spacing could be increased from, say, 0.65λ to 0.75λ while retaining the pointing performance inside the specified field-of-view, the number

of transmit/receive units could be reduced by 25% and the overall investment cost would drop in proportion!

Scope of M.Sc. project

The present M.Sc. project shall identify at least one, if possible two, medium-gain unit antennas optimised under the constraints posed by the 3D performance specifications, and for each of these investigate by numerical simulation the overall array behaviour as a function of the unit-to-unit spacing and orientation.

In particular, the possible advantages and drawbacks of orienting the booms of the unit antennas to an elevation of 77° as a means of optimising the gain along the local geomagnetic field line shall be investigated. This design concept has not been tried before to our knowledge. It may bring in a whole new set of problems, particularly as regards mutual coupling, which will be substantially different from that found in a conventional / orthogonally aligned array, but it is definitely worth of further consideration if it can be proven to work.

Because the EISCAT_3D system will be located in northern Scandinavia and operating in a sub-Arctic climate, the selected element antenna must be insensitive to climatic effects as far as possible, retaining its radiation pattern and electrical characteristics even when covered by a moderately thick layer of snow or ice. These aspects must also be verified in the analysis phase.

Detailed specification of M.Sc. project:

1. Specification and analysis of at least one, if possible two, short (3-4 elements), X-Yagi antenna(s) having the following characteristics:
   (a) Center frequency 235.0 MHz
   (b) Feed-point impedance 50+j0 ohms at center frequency
   (c) Bandwidth (specified as s_{11} < -20 dB) > +/- 6 MHz
   (d) Circularity better than -1 dB out to 30° off-boresight, in all azimuth directions and over full bandwidth,
   (e) Gain at angles > 75° off-boresight as low as possible, but at least -16 dB,
   (f) Element lengths < 0.4λ while maintaining all other characteristics,
   (g) Maximum relative gain at 40° off-boresight, consistent with all above points.

2. Analysis of the characteristics and performance of a large phased-array employing the specified Yagi(s) as element antennas, using element spacings from 0.6λ to 0.9λ and element alignment angles of 77 and 90 degrees:

   (a) Mutual coupling effects as a function of pointing angle out to 40° off-boresight, assuming that the array is laid out as a rectangular grid,

   (b) Optimum orientation of element antennas relative to one another to minimise mutual coupling (Yagi elements oriented parallel to the rows and columns of the array or at 45° to these ?),

   (c) Performance on the array at large off-boresight pointing angles (40°) close to the grating-lobe limit.

3. Simulation of weather effects by introducing a 3 mm sheet of clear sweet-water ice on all antenna elements,

4. Iteration of 1-3 above until a mechanically and electrically reproducible and relatively weather-immune design is found.

Note: The intrinsic antenna impedance can be selected freely, as long as it can be conveniently transformed to 50+j0 ohms at the feedpoint.

Contents

List of figures

List of tables

Partial list of symbols and abbreviations

β	Phase constant
Δr	Way difference
ϵ	permittivity
ϵ_A	Aperture efficiency
ϵ_L	Loss efficiency
ϵ_p	Polarization loss efficiency
Γ	Reflection coefficient
λ	Wavelength
ϕ	Azimuth angle
ϕ_Z	Phase of impedance Z
ψ	Phase-offset for beamforming off-broadsight
σ	Radar cross section
θ	Zenith angle
θ_3	Beamwidth
θ_{FN}	First Null beamwidth
θ_g	Zenith angle of grating lobe
A	Aperture area
A_E	Effective area
a	Logarithmic attenuation, Column spacing distance
b	Row spacing distance
D_0	Directivity
$D(\theta, \phi)$	Directive gain
d	Spacing distance
g_{kor}	Gain correction
$\mathbf{E}$	Electric field vector
k	Free-space wave number
L	Length of aperture
N_{min}	Minimum array elements per aperture length
P_{rad}	Radiated power
$\mathbf{p}$	Polarization vector
pos_r, pos_c	Array element positions row/column
R	Radial distance
r_i	Position vector
s	Voltage Standing Wave Ratio
s_{11}	Scatter parameter
S	Power density
t_ψ	Time-offset
u, v	direction cosine
Z	Impedance

ALWIN	ALomar WINd radar
AMISR	Advanced Modular Incoherent Scatter Radar
AMP	Antenna Modeling Program
EISCAT	European Incoherent SCATter, Scientific Association
EISCAT_3D	Project name of the currently planned new EISCAT radar
GNEC	Windows based NEC software package
IAP	Leibniz-Institute of Atmospheric Physics e.V. at University of Rostock
MoM	Method of Moments (NEC)
MST	Mesosphere Stratosphere Troposphere
NEC	Numerical Electromagnetic Code
OSWIN	OStsee WINd radar
SLA	Sidelobe Attenuation
SLL	SideLobe Level
UHF	Ultra High Frequency
VHF	Very High Frequency
VSWR	Voltage Standing Wave Ratio

Chapter 1

Introduction

In this chapter an introduction to this thesis work with its motivation and the project related incoherent scatter technique is briefly described.

In chapter 2 general definitions of the array and antenna theory are introduced, which will be used in the progress of this work. The basic theoretical characteristics of an array including off-boresight beamforming and the therefore resulting effects on the radiation pattern are presented.

The chapter 3, Modelling with NEC, describes the simulation software used in this thesis work.

Within chapter 4 the individual array element is presented. In the first step three different yagi designs are evaluated and afterwards the most promising single array element is chosen based on the given requirements, defined in the thesis tasks.

The theme of mutual coupling is evaluated in chapter 5. In this chapter the mutual coupling for different grid structures, on which the array elements are placed, are evaluated depending on the spacing of the elements and their orientation to each other.

In chapter 6 various array structures, based on the results of the earlier chapters, are presented and analyzed. The evaluated arrays are selected by its grid structure and aperture, while consisting of 100 up to 10000 array elements.

In the last chapter 7 a summary for the earlier chapters is given and after all the optimum array within the given limits and requirements is presented.

1.1 Motivation

To study the earth's ionosphere and its interaction with the upper atmosphere, the magnetosphere and solar wind, very powerful ground based radars are needed. EISCAT (European Incoherent SCATter) - founded in 1975 - is operating incoherent scatter radars in northern Scandinavia.

With the current incoherent scatter radar systems in northern Scandinavia, consisting of one VHF-system and two UHF-systems, EISCAT is able to use monostatic VHF-measurements and mono-, bi- and even tristatic UHF-measurements. With the UHF-system tristatic measurements have already been done since years from the three EISCAT sites in the proximity of Tromsø (Norway), Kiruna (Sweden), Sodankylä (Finland). Each site operates for the UHF-system a parabolic dish with a diameter of roughly 32 m to provide the necessary high gain to emit a powerful radar signal (Tromsø), while the other mentioned sites are receive-only stations. The VHF-system consists of four 30x40 m parabolic cylinders placed at Tromsø-site. As such big parabolic antennas are connected to a high weight and thus any movement of the main beam and thus rotation of the dish itself to a point in the sky needs a significant amount of time even for rather small deviation of the actual beaming position.
This drawback limits the possible research as only a rather small volume in the sky may be illuminated during one measurement.
A fast beam-swinging like it is done e.g. in a lot of mesosphere-, stratosphere- and troposphere (MST) radar systems, swinging from pulse to pulse with angular separation of e.g. 40° is far out of the current EISCAT VHF and UHF-systems capabilities.
Most of the MST-radars are arranged in large arrays of antennas, simple dipole or more directive antennas, to provide the needed directivity which offers additionally beam-swinging, if each single antenna or at least small groups are separately steered in phase.
To add a fast freely chosen beam-swinging to the EISCAT system, it is needed to add additional radiating sources in the antenna system. This can be realized for small angular deviation with an additional feed of the parabolic antenna, but is still in no shape to the abilities of an active array. There is furthermore no feasibility to achieve greater angular deviation without significant loss of directivity.
Additionally one may establish, under some limiting terms, with an active phased array a rather freely chosen distribution of radiated power. This becomes an important item if not only one highly directive so called pencil beam is needed. The ability to change the distribution of radiated power instantly provides a high degree of freedom to every experiment that will be held.
Additionally the chosen frequency of this new radar is planned for approximately 235 MHz, which is close to the currently used frequency of roughly 224 MHz. Therefore the new EISCAT_3D would expand the current monostatic VHF-system to a fivestatic radar as additional to the transmit-receive main system, with its active array evaluated in this thesis work, four receive-only stations shall be allocated in northern Scandinavia.
Additionally immense changes in the radar structure are connected to a phased array. Providing the high-frequency power signal, accurate in phase and magnitude for each

single array element. Allocating transmit-receive-units for each single array element including necessary data acquisition and transfer and operation controllers, grouped for a number of array elements around and placed in thermal cabinets out in the array field. Arrangement of the transmit-receive-units separated from the array would lead to intolerable high loss of power in the feeding cable network.

Therefore a very large active phased array would provide a significant amount of new abilities, which is currently planned in the EISCAT_3D project, but is also associated with challenging efforts.

Depending on the single array element and its specific arrangement within the array a total amount of approximately 10000 elements will be needed to achieve or maybe improve the current directivity of the existing VHF-system.

An array arranged with it's plane parallel to the ground surface with its elements oriented orthogonal to the array plane, the absolute possible maximum gain is always induced in broadside. Beamforming off-broadsight lead to deterioration of gain and beamwidth of the array.
The idea to evoke the maximum possible radiation energy off-zenith for a phased array has been implemented e.g. by the Advanced Modular Incoherent Scatter Radar (AMISR), where the whole plane of array structure itself has been mechanically tilted. Thus the array may form the maximum radiating energy as usual at broadside, but off-zenith. The resulting array geometry naturally does not limit any possible beamforming off-broadside.
However for the EISCAT_3D project such a way is quite difficult to realize as due to the wavelength and the designated amount of array elements the plane of the array would have to be elevated on one side by 35 m to 40 m above ground level, contrary to AMISR with just about 13 m height.
Thus the idea evolved to tilt each single array element physically 23° off-zenith, while keeping the array plane parallel to the ground surface. This seems to be a new realization of an array for an atmospheric radar with potential of yet unknown limiting parameters.

Summarized it can be quoted, the design of the antenna array itself, which is evaluated in this thesis work, plays an important role for the whole projected EISCAT_3D system, as the structure and amount of e.g. transmit-receive-, data acquisition and transfer units are restricted to the structure of the antenna array.

1.2 Incoherent scatter

The following information are partially taken from [HKH+97], an EISCAT information brochure [EIS96] and presentations regarding the EISCAT_3D project.

1.2.1 The incoherent scatter mechanism

The radar emits electromagnetic energy as a coded transmission which is scattered by electrons in the ionospheric plasma, which are controlled by massive positive ions. The power of the scattered echo is mainly determined by the electron density fluctuations caused by the presence of these ions. The received frequency spectrum provides information on the temperature, composition of the plasma and the velocity.
Furthermore the characteristic double-peaked ion-line spectrum of the incoherent scatter echo also gives knowledge of the electron temperature. Additionally the scattered signal spectrum contains plasma- or electron-lines, which are normally weaker than the ion-line. The electron-line illustrates scattering processes where the electrons act as no ions would be present.
As quoted above the total returned power depends on the number of electrons and gives an estimate of the ionospheric electron density. With aid of spectrums width one obtains the ratio of the ion temperature to ion mass. The overall shift of the spectrum corresponds to the bulk motion of the ions. The shape of the ion line spectrum is a sensitive function of the ratio of the electron and ion temperatures.
Furthermore EISCAT quotes with suitable assumptions about the concentrations of different ions in the ionosphere, the basic parameters of electron density, electron temperature, ion temperature and ion velocity are routinely derived by all incoherent scatter radars. In altitudes below 120 km, collisions between the ions and the neutral atmosphere affect the incoherent scattering process and result in a single-humped spectrum from which the frequency of ion collisions with the neutral molecules of the upper atmosphere can also be deduced.
From these basic results, many further ionospheric and upper atmospheric parameters can be deduced, though not all together nor in all altitude regimes. These include: ion composition, electric field strength, conductivity and current, Joule and particle heating rates, neutral air temperature, composition and wind speed, fluxes of heat and plasma along the earth's magnetic field lines and, with additional information from the electron lines, electric current density in the direction of the magnetic field and part of the spectrum of supra-thermal electrons.
Additionally, powerful radars such as EISCAT can observe scattering from ionization

irregularities set up by plasma and neutral atmosphere instabilities, allowing a range of E-region and mesospheric phenomena to be observed directly. These observations, and planned expansions to study tropospheric and stratospheric phenomena, have recently added a substantial new component to the observing programmes of several radars, particularly in the case of the EISCAT VHF system where the capabilities of the radar support important investigations into the coupling between the lower atmosphere and the ionosphere.

1.2.2 Incoherent scatter radars

Typical incoherent scatter radars radiate effective powers measured in gigawatts, but the returned signals normally represent only picowatts.
Powerful multi-mega-watt transmitters, large high-gain antennas (typically at least $1000\,m^2$ in area), sensitive receivers, sophisticated radar control and data acquisition systems are all necessary for the successful detection and evaluation of the weak incoherent scatter echoes received from the ionosphere.
The EISCAT radars can currently make measurements covering all altitudes from about 50 km to more than 2500 km. Structures smaller than 200 m can be resolved and studied on time scales ranging from tens of minutes to well under a second, depending on the geophysical phenomena. The measurements describe many of the fundamental characteristics of the ionosphere and upper atmosphere and support a wide range of scientific investigations aimed at understanding the complex effects of the sun on our environment.
Incoherent scatter radar systems provide a wealth of observational data and are complemented by detailed observations from balloons, rockets and satellites as well as a wide range of ground-based instruments including magnetometers, all-sky cameras, ionosondes and coherent (auroral) backscatter radars. Incoherent scatter radars have attracted many such instruments to their vicinity and will continue to provide the focus of substantial research efforts for the foreseeable future.

Further information on the EISCAT_3D project will be added to the attached CD.

Chapter 2

Theoretical considerations for the antenna design

The following generally used definitions are summarized to classify the characteristics of antennas.

2.1 Fundamentals of antenna theory

The radiated power density in $\frac{W}{m^2}$ watts per square meter at a distance R from a transmitter with an omnidirectional antenna is given by

$$S = \frac{P_{rad}}{4\pi R^2} \tag{2.1}$$

due to the principle of power conservation. P_{rad} is the total radiated power in watts.
Figure 2.1 indicates the coordinate system, which will be used in the following progress

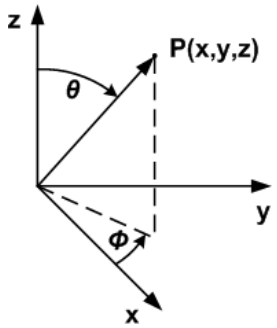

Fig. 2.1. Coordinate system

of this thesis work. The zenith angle and the azimuth angle are marked by θ and ϕ respectively.
For an existing directional pattern the antenna pattern directive gain $D(\theta, \phi)$ is given by

$$D(\theta, \phi) = \frac{4\pi R^2 S(\theta, \phi)}{P_{rad}} \tag{2.2}$$

due to power density $S(\theta, \phi)$ at a some distant spherical surface with distance R from the origin.

The total radiated power may be written as

$$P_{rad} = R^2 \int_{\Omega} S(\theta, \phi) d\Omega \tag{2.3}$$

and generally as

$$P_{rad} = R^2 S(\theta, \phi) sin\theta \int_0^{2\pi} d\phi \int_0^{\pi} d\theta \tag{2.4}$$

The directive gain $D(\theta, \phi)$ is accordingly defined as

$$D(\theta, \phi) = \frac{4\pi S(\theta, \phi)}{\int_{\Omega} S(\theta, \phi) d\Omega} \tag{2.5}$$

The directivity D_0 is the maximum value of the directive gain

$$D_0 = max[D(\theta, \phi)] \tag{2.6}$$

which is used often to characterize antenna attributes especially for antenna arrays due to its resulting narrow beamwidths.
Due to losses the radiated power is less than the input power P_{in} which may be described by an efficiency factor ϵ_L and the reflected signal power by the reflection coefficient Γ

$$P_{rad} = \epsilon_L P_{in}(1 - |\Gamma|^2) \tag{2.7}$$

where Γ is defined as

$$\Gamma = \frac{Z_l - Z_s}{Z_l + Z_s} \tag{2.8}$$

with Z_s as the impedance of the feeder toward the source and Z_l is the impedance toward the load in this case the antenna impedance. The antenna impedance and therefore Γ is measured at the feed point of the antenna.
Usually the voltage standing wave ratio (VSWR) s is used to characterize the match of a transmission line to a load e.g. an antenna. The VSWR s can be calculated by

$$s = \frac{1 + |\Gamma|}{1 - |\Gamma|} \tag{2.9}$$

or

$$s = \frac{V_{max}}{V_{min}} \tag{2.10}$$

where V_{max} and V_{min} are the maximum and minimum voltage which are e.g. measured on a transmission line or at the feed point of an antenna.
Furthermore the term return loss is used frequently and is calculated by

$$a = -10\log_{10}\left(\frac{P_{ref}}{P_{in}}\right) \tag{2.11}$$

where P_{ref} and P_{in} are the reflected and incident power. Additionally the return loss may be calculated directly from the impedances of the transmission line and load

$$a = -20\log_{10}\left(\left|\frac{Z_l - Z_s}{Z_l + Z_s}\right|\right) \tag{2.12}$$

or by the voltage standing wave ratio

$$a = -20\log_{10}\left(\left|\frac{1-s}{1+s}\right|\right) \tag{2.13}$$

Additionally one should consider the phase of the impedance

$$\phi_Z = \arg\{Z\} \tag{2.14}$$

which should be as constant as possible in the envisaged frequency domain. Setting a maximum magnitude of phase deviation may be used in term of phase bandwidth.
Generally at the usage frequency impedance match to a real impedance is aimed, therefore the impedance argument is kept small. Furthermore it's benefiting to have as most as possible flat impedance phase across the whole usage frequency to keep the phase differences minimized. This is obviously more challenging as more frequency bandwidth is desired.
Considering the losses a gain function $\mathrm{G}(\theta, \phi)$ may be defined with the aid of directive gain $\mathrm{D}(\theta, \phi)$ as

$$G(\theta, \phi) = \epsilon_L(1 - |\Gamma|^2)D(\theta, \phi) \tag{2.15}$$

In the far field the power density can now be written as

$$S(\theta, \phi) = \frac{P_{in}}{4\pi R^2}G(\theta, \phi) \tag{2.16}$$

The peak value of the gain function is called the gain G_0 and analogue to the directivity D_0

$$G_0 = max[G(\theta, \phi)] \tag{2.17}$$

Depending on the amplitude and phase illumination of the aperture various values for the directivity are possible. The maximum directivity of a planar aperture array is achieved, not considering superdirectivity, by a uniform phase and amplitude illumination and is defined by

$$D_{max} = 4\pi\frac{A}{\lambda^2} \tag{2.18}$$

with the aperture area A and the wavelength λ.
Additionally one may estimate the maximum directivity for a single main lobe pattern due to the width of main lobe as [Bal05] with [Kra88] quoted

$$D_{max} = \frac{4\pi(180/\pi)^2}{\theta_{3,1}\theta_{3,2}} \tag{2.19}$$

where $\theta_{3,1}$ and $\theta_{3,2}$ are the half-power beamwidth in one plane and the orthogonally. Alternatively [TP76] stated for the maximum directivity

$$D_{max} = \frac{32\ln(2)}{\theta_{3,1}^2 \theta_{3,2}^2} \tag{2.20}$$

Furthermore the resulting half-power beamwidth θ_3 may be calculated by

$$\theta_3 = \arcsin\left(0.886 \cdot \frac{\lambda}{L}\right) \tag{2.21}$$

where λ is the wavelength and L the aperture length.
Alternatively sometimes the beamwidth is defined between the first nulls around the main lobe and thus called First-Null-beamwidth and can be calculated by

$$\theta_{FN} = 2 \cdot \arcsin\left(\frac{\lambda}{L}\right) \tag{2.22}$$

The last assumptions are made for a uniform illumination of a regular array.

Considering the planar aperture of antenna arrays consisting of a distribution of large numbers of elements (single antennas) it is suitable to define the aperture efficiency ϵ_A. Due to this the gain may be described with

$$G_0 = \epsilon_A \epsilon_L (1 - |\Gamma|^2) D_{max} \tag{2.23}$$

for a two-dimensional aperture antenna array with the assumption of a large number of elements.
The received power P_r of an antenna by an incident wave field is depending on the amount of energy it collects. It's convenient to define an effective area A_E of an antenna. Using this term A_E while the receiving antenna and the incident wave have the same polarization it can be written for the received power

$$P_r = A_E S(\theta, \phi) \tag{2.24}$$

With the directivity D_0 it may be written

$$A_{E_{max}} = \frac{\lambda^2}{4\pi} D_0 \tag{2.25}$$

where $A_{E_{max}}$ is the maximum value of the effective area.
Assuming match of polarization and including losses the effective area is

$$A_E = \frac{\lambda^2}{4\pi} D_0 \epsilon_{ER} (1 - |\Gamma_r|^2) = \frac{\lambda^2}{4\pi} G_R \tag{2.26}$$

with the loss efficiency ϵ_{ER}, reflection coefficient and gain for the receiving antenna.
The polarization of an electromagnetic wave is defined with the orientation of the electric field $\mathbf{E}$ as

$$\underline{\mathbf{p}} = \frac{\mathbf{E}}{E} \tag{2.27}$$

In general the polarization of an incident wave and the receiving antenna doesn't have to be the same so that one can use a polarization loss efficiency ϵ_p defined by

$$\epsilon_p = \left| \underline{\mathbf{p_r}} \cdot \underline{\mathbf{p_w}}^* \right|^2 \tag{2.28}$$

with the unit polarization vector $\underline{\mathbf{p_w}}$ and $\underline{\mathbf{p_r}}$ of the incident wave and receiving antenna respectively. Consequently the total power received is given by

$$\begin{aligned} P_r &= S A_E \epsilon_p \\ &= S \frac{\lambda^2}{4\pi} D_0 \epsilon_{ER} \epsilon_p (1 - |\Gamma_r|^2) \\ &= S \frac{\lambda^2}{4\pi} \epsilon_p G_R \end{aligned} \tag{2.29}$$

The total power received may be written by recapitulating the effective aperture, power density (equation 2.1) and polarization efficiency

$$P_r = P_T G_T \left[\frac{\lambda}{4\pi R} \right]^2 G_R \epsilon_p \tag{2.30}$$

where the squared term in brackets represents the free-space loss factor as a result of the spherical spreading of energy radiated by the antenna. Index T denotes the transmitter depended variables.
For a monostatic radar system the received power can be defined analogue to the above as

$$P_r = \frac{P_T G_T}{4\pi} \sigma \left[\frac{\lambda}{4\pi R} \right]^2 G_R \epsilon_p \tag{2.31}$$

where σ is the scattering cross section of the target. It is assumed the target intercepts power equal to its cross section multiplied by the incident power and isotropic reradiation. The factor $P_T G_T$ is called effective isotropic radiated power EIRP.
Each array element radiates a vector directional pattern which is angle and radial dependent in closer proximity to the element itself.
For a very far distance from the element the radiation has a $\frac{\mathrm{e}^{-jKR}}{R}$ dependence of a spherical wave multiplied by the element pattern which is a vector function of angle $\mathbf{f_i}(\theta, \phi)$. Thus one can write the far-field of an array element as

$$\mathbf{E_i}(r, \theta, \phi) = \mathbf{f_i}(\theta, \phi) \frac{\mathrm{e}^{-jkR_i}}{R_i} \tag{2.32}$$

where

$$k = \frac{2\pi}{\lambda} \tag{2.33}$$

is the free-space wave number and

$$R_i = [(x - x_i)^2 + (y - y_i)^2 + (z - z_i)^2]^{1/2} \tag{2.34}$$

With the position vector of each array element

$$\mathbf{r_i} = \mathbf{x}x_i + \mathbf{y}y_i + \mathbf{z}z_i \tag{2.35}$$

where **x**, **y**, **z** are the unit vectors respectively.
The unit vector **r** to any point in space can be written

$$\mathbf{r} = \mathbf{x}u + \mathbf{y}v + \mathbf{z}cos\theta \tag{2.36}$$

where u and v are the direction cosines

$$u = sin\theta cos\phi \tag{2.37}$$
$$v = sin\theta sin\phi \tag{2.38}$$

Further considerations are related to the far-field (Fraunhofer) region, which is for small antenna structures usually set at a distance R of

$$R > 2\lambda \tag{2.39}$$

but for aperture antennas where its largest dimension L is significantly greater than the wavelength λ is given by

$$R \geq \frac{2L^2}{\lambda} \tag{2.40}$$

while partially a five times larger distance is suggested for far-field measurements of extremely low sidelobe or deep nulled pattern.
In addition to equation 2.40 the region up to R is called respectively near-field, which is furthermore subdivided into reactive near-field

$$R \leq 0.62\sqrt{\frac{L^3}{\lambda}} \tag{2.41}$$

and radiating near-field region, between the reactive near-field (2.41) and the far-field (2.40).
Figure 2.1 shows exemplary the field regions where R_1 is the radius of reactive near-field, R_2 limits the radiating near-field and for distances greater R_2 respectively the far field region.
The radiation pattern for an array can be written by the aid of superposition

$$\mathbf{E}(r,\theta,\phi) = \frac{\mathrm{e}^{-jKR}}{R}\sum_i a_i \mathbf{f_i}(\theta,\phi)\mathrm{e}^{jk\mathbf{r_i}\mathbf{r}} \tag{2.42}$$

where a_i are the elements weights. This equation implies different radiation pattern for each element in the array. Assuming well sized aperture array and equal spacing of each element one can neglect the differences between the individual elements pattern

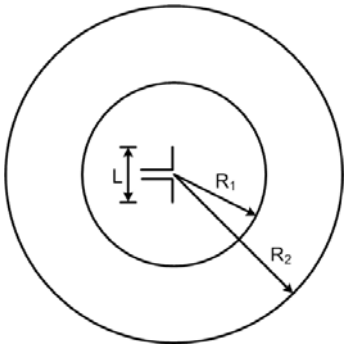

Fig. 2.2. Field regions

as the influence of the edge elements deteriorate with the increase of aperture size. Thus it can be written

$$\mathbf{E}(r,\theta,\phi) = \mathbf{f}(\theta,\phi)\frac{\mathrm{e}^{-jKR}}{R}\sum_i a_i \mathrm{e}^{jk\mathbf{r_i}\mathbf{r}} \tag{2.43}$$

However not specially marked general and worthwhile additional information could be taken from [ZB00], [Gro01] for the fundamentals regarding antennas and special radar related knowledge from [Goe01], additional array-referring basics may be taken from [Mai94] or [LBM82].

2.2 Sidelobes

Attenuation of sidelobes depends on the array aperture and its illumination. For a uniform illumination of a rectangular array aperture the attenuation on the first sidelobe is only 13.3 dB relative to the main lobe [Bal05]. However for a circular array aperture with uniform illumination the first sidelobe is attenuated by 17.6 dB.
From the above stated one may suggest that additional sidelobe attenuation may be achieved by using amplitude taper. Amplitude taper may significantly enhance sidelobe attenuation at the expense of beam broadening and associated gain loss. Table 2.1 shows a selection of illuminations with their characteristics for a line source, where θ_3 is the 3 dB-beamwidth, θ_{FN} is the angle of first null next to the main lobe (equation 2.22) and SLL the shortcut for sidelobe level. The values shown in table 2.1 may immediately be transferred to planar arrays with rectangular aperture for each broadside plane respectively.
In table 2.2 similar illuminations of first three rows of table 2.1 are presented for a circular array aperture.

Tab. 2.1. Amplitude tapering line source array, [Bal05] and [Mai94]

distribution	directivity pattern	θ_3 [°]	θ_{FN} [°]	SLL [dB]	gain factor
$f(x) = 1$	$l \cdot \mathrm{sinc}\,(u)$	$50.8\frac{\lambda}{l}$	$57.3\frac{\lambda}{l}$	13.2	1
$f(x) = \cos\left(\frac{\pi x}{2}\right)$	$\frac{\pi l}{2} \cdot \frac{\cos(u)}{\left(\frac{\pi}{2}\right)^2 - u^2}$	$68.8\frac{\lambda}{l}$	$85.9\frac{\lambda}{l}$	23	0.81
$f(x) = \left(\cos\left(\frac{\pi x}{2}\right)\right)^2$	$\frac{l}{2} \cdot \frac{\pi^2}{\pi^2 - u^2} \cdot \mathrm{sinc}\,(u)$	$83.2\frac{\lambda}{l}$	$114.6\frac{\lambda}{l}$	32	0.667
$f(x) = 1 - \lvert x \rvert$	$\frac{l}{2} \cdot \left(\mathrm{sinc}\left(\frac{u}{2}\right)\right)^2$	$73.4\frac{\lambda}{l}$	$114.6\frac{\lambda}{l}$	26.4	0.75

Tab. 2.2. Amplitude tapering circular-aperture, [Bal05] and [Mai94]

distribution	directivity pattern	θ_3 [°]	θ_{FN} [°]	SLL [dB]	gain factor
$f(r) = 1$	$\pi\sigma^2 \frac{J_1 u}{u}$	$58.9\frac{\lambda}{D}$	$69.8\frac{\lambda}{D}$	17.6 dB	1
$f(r) = (1 - r^2)$	$2\pi\sigma^2 \frac{J_2 u}{u}$	$72.7\frac{\lambda}{D}$	$93.6\frac{\lambda}{D}$	24.6 dB	0.75
$f(r) = (1 - r^2)^2$	$8\pi\sigma^2 \frac{J_3 u}{u}$	$84.3\frac{\lambda}{D}$	$116.2\frac{\lambda}{D}$	30.6 dB	0.56

For example using a triangular instead of uniform illumination one gains about 13 dB sidelobe attenuation while increasing the beamwidth by a factor of roughly 1.45 and losing 25 percent of gain.

The sidelobe attenuation mentioned in table 2.1 and 2.2 respectively is only considering the first sidelobe, while the increase of attenuation for further disposed sidelobes deteriorates. The second sidelobe is suppressed by only 17.8 dB to the main lobe and is therefore only 4.9 dB greater than the first sidelobe. The attenuation from second to third sidelobe reaches even only 3.9 dB.

Additionally one has to be aware of the positions where sidelobes appear. For a rectangular aperture sidelobes containing the most energy emerge directly aligned to the edges of the aperture like shown in figure 2.3(a). However sidelobes for a circular aperture array are mainly formed as rings around the main lobe which is shown in figure 2.3(b).

As pointed out earlier for a circular aperture the sidelobe attenuation is improved by 4.4 dB, however the sidelobe energy is radially spread instead of being concentrated in four single lobes. Nevertheless the radially spread sidelobe energy is generally advantageous as an equal maximum sidelobe attenuation for every azimuth direction is

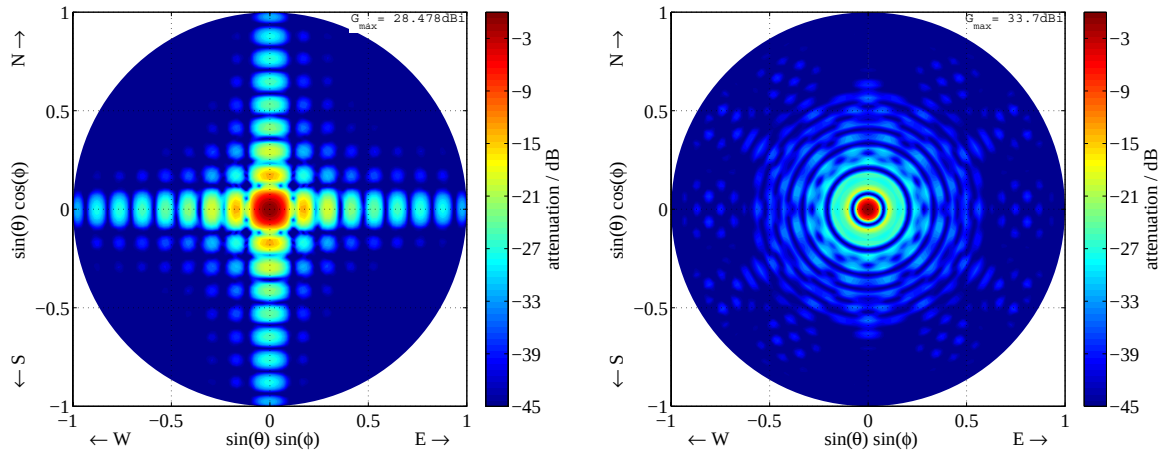

(a) ALWIN array

(b) ALWIN2 array study

Fig. 2.3. Sidelobe radiation pattern comparison

achieved.
Additional to the announced illuminations in table 2.1 and 2.2, further Tschebyscheff-polynomials may be used. By the selection of the coefficients of Tschebyscheff-polynomials one may improve the sidelobe attenuation up to 50 dB and more. However this results in broadening of the main beam by a factor of 1.5 and thus deteriorate the maximum directivity. As this way of sidelobe-attenuation improvement at cost of beamwidth and/or power decrease is in principle not wanted by EISCAT this item will not be evaluated any further, however additional information may be taken from e.g. [Bal05].

As analogy to sidelobes of radiation in array theory exactly same characteristics can be observed at optical slit or acoustic sonar diffraction. Depending on the amount and aperture of slits the intensity pattern due to optical diffraction equals characteristics described for antenna array radiation.

2.3 Beam broadening

Due to beamforming at off-broadside angles θ_b the half-power beamwidth increases depending on the steering angle.

[Mai94] stated for a linear or rectangular array of length L consisting of N elements in scan plane

$$\theta_{3b} = \left[\arcsin\left(sin(\theta_b) + 0.443 B_b \frac{\lambda}{L}\right) - \arcsin\left(sin(\theta_b) - 0.443 B_b \frac{\lambda}{L}\right)\right] \qquad (2.44)$$

where B_b is the beam broadening factor and L the length of the array defined by

$$L = Nd_x \tag{2.45}$$

the total number of elements N with spacing d_x in direction of x-axis. The broadening factor depends on the illumination of the array (section 2.2). For equal illumination of the array B_b is defined as unity. Nonuniform illumination of the array is used to enhance sidelobe attenuation and is called amplitude taper.

2.4 Evaluation of grating lobes

Grating lobes are special sidelobes that may arise up to equal scale as the wanted main lobe. In some cases next to the wanted main lobe a significant amount of power may be radiated or received far away from main beam. Thus special treatment has to be performed to this theme.
Grating lobes occur due to regular repetition of element structures in the array, depending on the spacing of the array elements and the grid structure. For array element spacings of greater than half wavelength grating lobes develop in real space when high off-boresight or at least end-fire, beam-forming perpendicular to broadside, is used.
The occurrence of grating lobes is calculated by

$$\pi \frac{d}{\lambda} \left[\sin\left(\theta_g\right) - \sin\left(\theta_0\right)\right] = \pm n\pi \tag{2.46}$$

where θ_g and θ_0 are the zenith angles of grating and main lobe respectively [Mai94]. Considering the EISCAT_3D planned beam steering up to $\theta_0 = 40°$ and condition

$$\left|\sin\left(\theta_0\right)\right| \leq 1 \tag{2.47}$$

leads to an element spacing

$$d \leq 0.6087\lambda \tag{2.48}$$

for grating-lobe-free beam steering for a regular line array.
Thus one can obtain the minimum necessary number of array elements per line by

$$\begin{aligned} N_{min} &= \frac{L}{d_{max}} \\ &= \frac{L}{\lambda}(1 + \sin\left(\theta_0\right)) \end{aligned} \tag{2.49}$$

where θ is the off-boresight angle, in this case the zenith angle, and L the length of one side of the considered array. Due to equation 2.49 it is needed at least an amount of 129 array elements in one 100 m row on a squared array grid structure for the claimed

grating-lobe-free 40° off-zenith bearing and given wavelength. Contrary to this result one would alternatively, considering an equilateral grid structure, need only 116 array elements on the same lengths which nearly comes along with a spacing of $d = 0.7\lambda$.
While the spacing of the array elements and the desired scan off-zenith angle itself determine the appearance as a function of zenith angle θ. Although the array geometry, in detail the exact position of the next closest array elements to each other, determines the azimuth appearance angle. Thus for a rectangular grid structure the grating lobes appear at orthogonally angles of $\phi = 0°$, 90°, 180°, 270° relative to the main beam at ϕ_0 and θ_0. Contrary to this an equilateral grid structure evokes the next grating lobes at azimuth angles of $\phi = 30°$, 150°, 210°, 330° relative it the main lobe. Analogical is valid for any other array grid structure.
One solution to this issue is the avoidance of any grating lobes in principle by not using larger array element spacings as equation 2.47 allows for the desired maximum off-broadside beam.
On the other hand a change of array grid structure has severe influence to the grating lobes as pointed out earlier. Figure 2.4(a) shows the radiation pattern in top view of the OSWIN radar system, evaluated in [Rub98], operated by the Leibniz-Institute of Atmospheric Physics e.V. at University of Rostock (IAP), if every row would be phased separately. One can clearly see the appearance of a grating lobe with its maximum at $\theta = 73°$, $\phi = 180°$ in the main axis, while the main beam is formed at an off-zenith angle of $\theta = 26°$ and azimuth $\phi = 0°$.
In contrast in a triangular equilateral grid structure the next close-by grating lobes

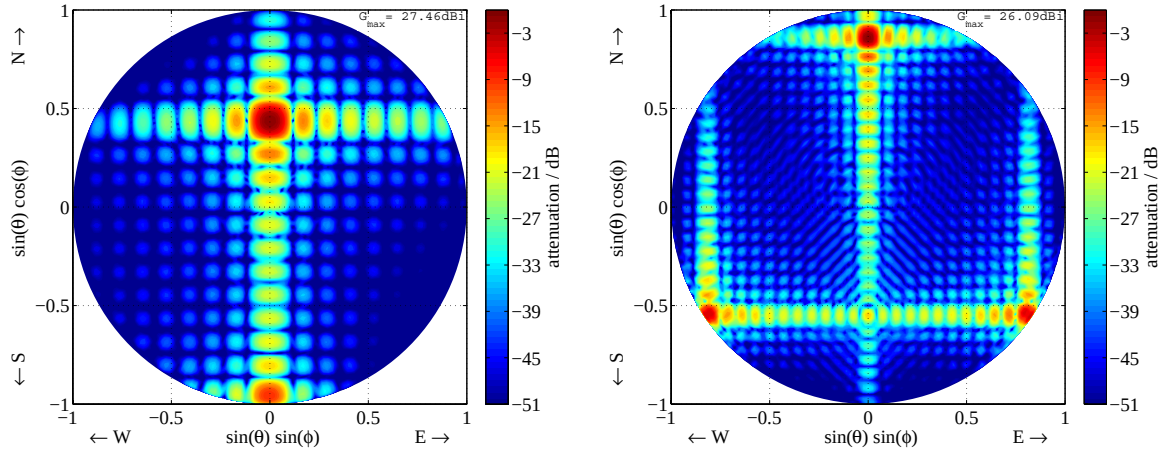

(a) OSWIN array (b) EISCAT 3D study array

Fig. 2.4. Grating lobe radiation pattern comparison

occur in $\phi = \pm 30°$ relative to the main lobe opposed to the azimuth of beam forming. Figure 2.4(b) shows a top view plot of a radiation pattern generated within this thesis work for the almost same spacing but array elements oriented on equilateral grid.

The simulated array in figure 2.4(b) consists of 449 array elements (see also figure 6.7(a)) and main beam is steered to $\theta_0 = 60°$. One clearly sees the two induced grating lobes outlying the main axis, but appear at a far greater angle of main beam as they are evoked in figure 2.4(a).
Ancillary it has to be added that currently within the OSWIN-system not every array element is fed separately in phase, but this limitation of phasing the array elements and thus the resulting deterioration of antenna radiation pattern has not been included in the shown figure.
Additionally the earlier announced sidelobes due to the chosen rectangular aperture of the array are clearly visible in both figures.
Due to the equilateral grid structure one gains an additional grating-lobe-free steering angle as the grating lobe is still not emitted as it would be for a squared grid structure, which is depicted in figure 2.5 .
Figure 2.5(a) schematically shows the approach of a grating lobe at the horizon for a

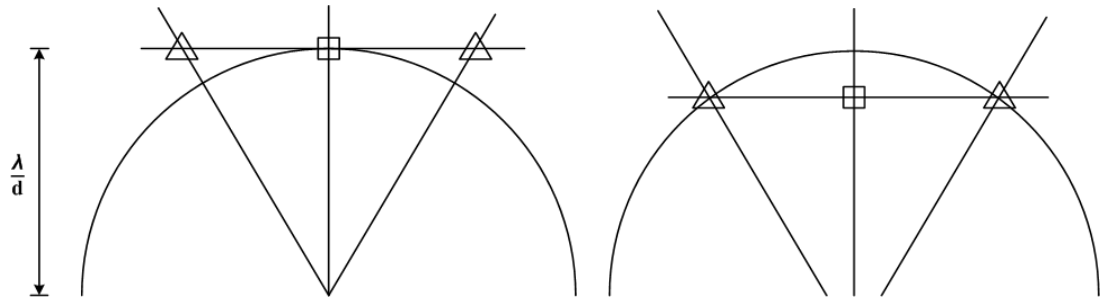

(a) for squared aperture (b) for circular aperture

Fig. 2.5. Approach of grating lobes

squared grid structure(marked with a square), while for an equilateral grid structure (marked with triangle) both nearest grating lobes are still not emitted. Figure 2.5(b) shows the event, when both nearest grating lobes of a equilateral grid structure are emerged, however for the same spacing the grating lobe of the squared grid structure is yet about 12° over the horizon.
Another way to solve the grating lobe issue is to generate nulls in the radiation pattern of each array element which exactly fit the direction of grating lobe appearance. Due to resulting overall radiation pattern is the product of array and element characteristic, the grating lobe might be suppressed significantly. For any freely steered radar beam this task is almost impossible to achieve as the positions of grating lobes are steered with the main beam and the element radiation pattern has to be adaptively modified simultaneously. A possible solution to this is the setup of additional small scale subelements in which the necessary attenuation is formed in determined direction.
As for EISCAT_3D pulse-to-pulse beam steering is envisaged this mentioned method

seems very challenging and evokes a far more complex and highly cost-intensive antenna array.
For this thesis work first two methods are considered, a triangular grid structure and avoidance of grating lobes in general.
Due to equilateral triangular grid structure and planned beam steering up to $\theta_0 = 40°$, element spacings up to 0.7 wavelengths may be used for grating-lobe-free radiation pattern.

2.5 Thinned array

The term of a thinned array stresses the idea of decreasing the amount of array elements per area with the radius.
The advantage of thinned arrays is the evocation of a narrow beamwidth with only a relative low amount of resources needed since the beamwidth is related to the largest dimension of aperture. However the array gain is directly related to the illuminated aperture and thus the amount of array elements.
Compared to a completely filled a thinned array will have almost the same beamwidth, but the array gain will approximately drop in proportion to the fraction of elements removed. Therefore it is possible to establish a highly directive array within the related gain loss but to a fraction of costs of a completely filled array.
Another advantage of thinned array is the manipulation of the sidelobes of a given array. As quoted in section 2.2 sidelobes and their attenuation to the main lobe are directly related to the aperture which may be combined with thinned arrays.
The method of thinning involves the deterioration of gain and pattern. Next to others [Lo93], [Ste73] and [Sko64] evaluated thinned arrays and presented summaries of thinning methods for regular and statistically distributed array elements.
For the EISCAT_3D project it has to be carefully elicited if any further advantage may be obtained from thinning the array beside improve of sidelobe attenuation.
The aspect of mutation of radiation pattern by the aid of a thinned array is evaluated within this thesis work in section 6.4.

2.6 Superdirectivity

Generally the maximum directivity is achieved for uniformly, phase constant, illumination of an array. For certain non-uniform phase distribution higher directivity values may be achieved, which is called superdirectivity.
According to [Mai94] superdirectivity is evoked by rapid phase variations across the array of closely spaced elements ($d < 0.5\lambda$). The higher directivity refers to an interference process of sidelobes while the main beam is partially or totally outside visible space. [Han85] quotes the resulting ratio of stored-to-radiated energy is extremely high and therefore the bandwidth is very small. Furthermore it's quoted a low radiation resistance and thus a poor efficiency leading to a high antenna noise temperature in the presence of losses. The superdirectivity theory is dependent on highly accurate current determination, therefore small errors may deteriorate its advantage.
In summary superdirectivity is no option for the EISCAT_3D active array and therefore this thesis work, as several limiting parameters can't be achieved for any serious advantage.

2.7 Phased array theory

The resulting main beam of an array may be formed in other directions than broadside by feeding the array elements with adequate phase- or time-offset.
The necessity of phase differences appears due to way differences Δr from a distant point P to the specific array elements or otherwise, which is shown in figure 2.6. The

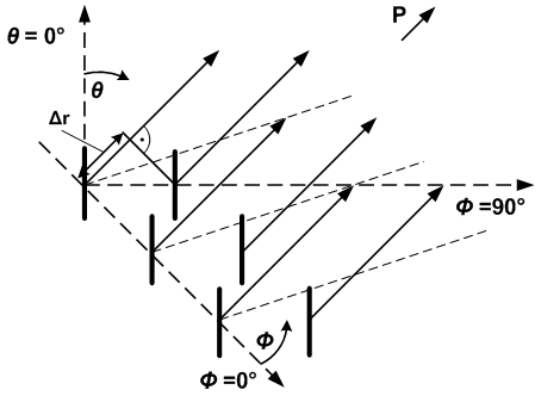

Fig. 2.6. Beamforming array schema

main beam is always moved into the directions of increasing negative (delayed) phase.

In this thesis work generally phase-offset is used, but can easily be converted to the alternatively possible time-offset by

$$t_\psi = \frac{1/f}{360} \cdot \psi \tag{2.50}$$

which leads with the operating frequency f of 235 MHz and phase angle $\psi = 1°$ to 11.8 ps for 1° resolution. Time-delay is projected to be used in the realization of EISCAT_3D.
For a specific off-broadside beam the necessary phase- or time-offset is depending on the structure of the array by means of relative positions of the elements in the array.

When main beam is formed at azimuth angle ϕ and zenith angle θ the phase of a single array element can be calculated by

$$\begin{aligned} \psi[°] = -360° \cdot \quad & [(pos_c - 1) \cdot \tfrac{a}{\lambda} \cdot \sin(\theta)\cos(\phi) \\ & +(pos_r - 1) \cdot \tfrac{b}{\lambda} \cdot \sin(\theta)\cos(\phi)] \end{aligned} \tag{2.51}$$

where a and b are the spacing of array elements in direction of column and row respectively, which generally don't have to be equal. Furthermore the observed array element is defined by its relative position, as a multiplier of the spacing, within the array in terms of column and row, pos_c and pos_r respectively. A reference element, e.g. at the center or an edge of the array, has to be defined from where pos_c and pos_r are counted. In equation 2.51 the columns are aligned to $\phi = 0°$ and therefore the rows orthogonal ($\phi = 90°$).

In the following of this thesis work the spacing may be marked as d, which refers to the general spacing, actually the spacing in orthogonal plane depends on the considered grid structure.

For a rectangular grid structure the parameters a and b in equation 2.51 depend on the actual geometry of the array.

$$\begin{aligned} d &= a \\ b &= x \cdot a \end{aligned} \tag{2.52}$$

where x is a array geometry dependent multiplier determining the relation of columns and rows.
For the special case of a squared grid structure both spacings are equal in row and column direction.

$$d = a = b \tag{2.53}$$

An example of an array with squared grid structure is shown in figure 6.4(a).

For an equilateral grid structure like shown in figure 6.4(b) the spacing b is given by

$$\begin{aligned} d &= a \\ b &= \frac{\sqrt{3}}{2} \cdot a \end{aligned} \tag{2.54}$$

due to the geometry of an equilateral triangle.

Beamforming on an irregular grid, where is no general spacing d to be considered anymore, which determines the geometry and thus the radiation characteristics, may naturally also be induced.
For an irregular grid structure one certainly may also use the same equation 2.51, while defining a and b as the lowest spacing between the elements in column and row respectively. The position of the element is obtained analog to the other grid structures by spacings a and b and an appropriate multiplier.

2.7.1 Principle of superposition

If at least two waves of same frequency are submitted from different points in an observed volume the transmitted waves will interfere with each other. This interference of two waves induces a new wave affected by the characteristics of the initial waves. Depending on the magnitude, phase and direction of propagation of the two incident waves the superposed wave is manipulated.
Superposition may be deployed to electromagnetic waves and thus to the superposition of waves induced by radiating waves from different antennas in an observed volume.
As pointed out the parameter of superposition are the magnitude of the waves and their belonging phases at a chosen point. The magnitude and phase of the wave at a chosen point moreover depend on the relative position, the propagation medium in terms of attenuation and phase rotation, the amount of energy provoking the wave and its distribution.

With general equations from [MG86], [Mai94], [Bal05] and [Sti84] one may start with the electric field vector $\mathbf{E}$ of two different origins at a point P, that may be described as

$$\begin{aligned} \mathbf{E_1} &= |\mathbf{E_1}|\mathrm{e}^{j\omega t} = |\mathbf{E_0}|\mathrm{e}^{-j\beta_1}\mathrm{e}^{j\omega t} = |\mathbf{E_0}|\mathrm{e}^{-j2\pi r_1/\lambda}\mathrm{e}^{j\omega t} \\ \mathbf{E_2} &= |\mathbf{E_2}|\mathrm{e}^{j\omega t} = |\mathbf{E_0}|\mathrm{e}^{-j\beta_2}\mathrm{e}^{j\omega t} = |\mathbf{E_0}|\mathrm{e}^{-j2\pi r_2/\lambda}\mathrm{e}^{j\omega t} \end{aligned} \tag{2.55}$$

where β_1 and β_2 are phase angles of $\mathbf{E_1}$ and $\mathbf{E_2}$ respectively, λ the wavelength, r_1 and r_2 the vector from the source to point P, ω is the angular frequency due to

$$\omega = 2\pi \cdot f \tag{2.56}$$

with frequency f.
The characteristic of a single antenna can be described by

$$C_E(\phi, \theta) = \left| \frac{\mathbf{E_e}}{\mathbf{E_0}} \right| = \frac{E_e}{E_0} \tag{2.57}$$

where $\mathbf{E_e}$ is the electric field of a single element.

In the following progress the superposition for an rectangular grid structure is evaluated.

2.7.2 Column aligned radiators

Figure 2.7 depicts a number of radiating dipole antennas (elements) oriented in a column aligned to $\phi = 0°$. Each vector r_1 to r_n from the antennas to a point P in a large distance relative to $(n-1)\Delta r$ has approximately same length.

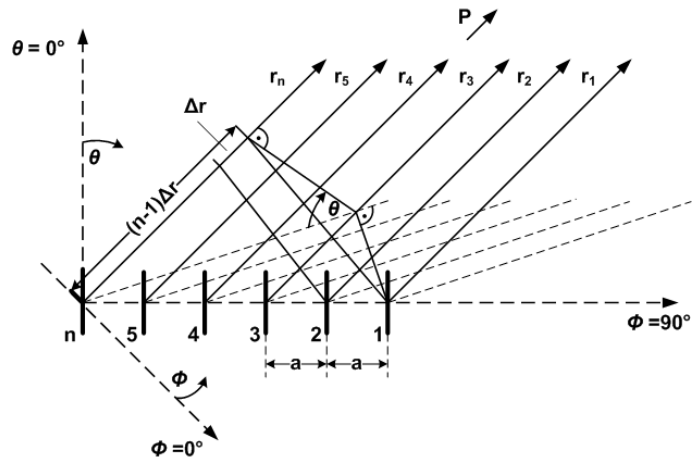

Fig. 2.7. Horizontal column aligned radiators

$$r_1 \approx r_2 \approx ... \approx r_n \tag{2.58}$$

Thus also the magnitude of the electrical field at point P evoked by the antennas 1 to n are approximately the same

$$|\mathbf{E_1}| \approx |\mathbf{E_2}| \approx ... \approx |\mathbf{E_n}| \tag{2.59}$$

as they are roughly only differ in a phase difference β

$$\beta = \frac{2\pi\Delta r}{\lambda} \tag{2.60}$$

due to the difference Δr, which can be written as

$$\Delta r = a\cos(\phi)\sin(\theta) \tag{2.61}$$

At point P the electric field components of two chosen Δr separated antennas superpose to $\mathbf{E_{sum}}$ and thus one gets with 2.57

$$|\mathbf{E_{sum}}| = \left|2 \cdot \cos\left(\frac{\beta}{2}\right) \cdot \mathbf{E_e}\right| = |C_e\mathbf{E_0}|\left|2 \cdot \cos\left(\frac{\beta}{2}\right)\right| \tag{2.62}$$

and by the aid of 2.60

$$|\mathbf{E_{sum}}| = |C_e\mathbf{E_0}|\left|2 \cdot \cos\left(\frac{\pi a}{\lambda}\cos(\phi)\sin(\theta)\right)\right| \tag{2.63}$$

for the electric field of two similar antennas aligned to $\phi = 0°$. Therefore compared to equation 2.57 one defines the group characteristic generally to

$$C_g(\phi,\theta) = \left|\frac{\mathbf{E_{sum}}}{\mathbf{E_e}}\right| = \left|\frac{\mathbf{E_{sum}}}{C_e\mathbf{E_0}}\right| \tag{2.64}$$

and thus for two $\phi = 0°$ aligned antennas in a column to

$$C_{g2c} = \left|2 \cdot \cos\left(\frac{\pi a}{\lambda}\cos(\phi)\sin(\theta)\right)\right| \tag{2.65}$$

The total characteristic refers to the characteristic of the group and the single element and therefore

$$C_{tot_c} = C_e \cdot C_{g2c} = C_e\left|2 \cdot \cos\left(\frac{\pi a}{\lambda}\cos(\phi)\sin(\theta)\right)\right| \tag{2.66}$$

in the example of 2 column antennas.
For a group of more than two elements the phase difference β_n between radiator 1 and n is derived by

$$\beta_n = \frac{2\pi(n-1)\Delta r}{\lambda} = (n-1)\beta \tag{2.67}$$

and for $\phi = 0°$ aligned elements by

$$\beta_n = (n-1)\frac{2\pi a}{\lambda}\cos(\phi)\sin(\theta) \tag{2.68}$$

For the electric field at point P one now writes

$$\mathbf{E_{sum}} = \sum_{k=1}^{n} \mathbf{E_0} C_e \mathrm{e}^{-j(k-1)\beta} \tag{2.69}$$

with

$$\mathbf{E_k} = \mathbf{E_0} C_e \mathrm{e}^{-j(k-1)\beta} \tag{2.70}$$

with $k = 1...n$. Expanding equation 2.69 by $(1 - \mathrm{e}^{-j\beta})$ one gets

$$\mathbf{E_{sum}}(1 - \mathrm{e}^{-j\beta}) = \mathbf{E_0} C_e (1 - \mathrm{e}^{-jn\beta}) \tag{2.71}$$

Therefore one may now write the group characteristic according to 2.64 to

$$C_{g_c} = \left| \frac{\mathbf{E_{sum}}}{C_e \mathbf{E_0}} \right| = \left| \frac{1 - \mathrm{e}^{-jn\beta}}{1 - \mathrm{e}^{j n\beta}} \right| = \sqrt{\frac{1 - \cos(n\beta)}{1 - \cos(\beta)}} \tag{2.72}$$

and with $(\sin(x))^2 = \frac{1}{2}(1 - \cos(2x))$ finally

$$C_{g_c} = \left| \frac{\sin\left(\frac{n\beta}{2}\right)}{\sin\left(\frac{\beta}{2}\right)} \right| = \left| \frac{\sin\left(\frac{n\pi a}{\lambda} \cos(\phi) \sin(\theta)\right)}{\sin\left(\frac{\pi a}{\lambda} \cos(\phi) \sin(\theta)\right)} \right| \tag{2.73}$$

and for the total characteristic for a group of n antennas arranged in a column $\phi = 0°$

$$C_{tot_c} = C_e \cdot C_{g_c} = C_e \left| \frac{\sin\left(\frac{n\pi a}{\lambda} \cos(\phi) \sin(\theta)\right)}{\sin\left(\frac{\pi a}{\lambda} \cos(\phi) \sin(\theta)\right)} \right| \tag{2.74}$$

The indeterminate forms for e.g. $\phi = 90°$ and $\theta = 0°$ may be solved by the L'Hospital's rule to

$$\lim_{\phi \to 90°, \theta \to 0°} C_{tot_c}(\phi, \theta) = C_e \frac{n \cdot \cos\left(\frac{n\pi a}{\lambda} \cos(90°) \sin(0°)\right)}{\cos\left(\frac{\pi a}{\lambda} \cos(90°) \sin(0°)\right)} = n \cdot C_e \tag{2.75}$$

2.7.3 Row aligned radiators

For row aligned radiators ($\phi = 90°$) generally same equations can be written. The difference is the orientation of the antenna group relative to the point P, which is shown in figure 2.8. Thus one gets in principle the same equation for the phase angle 2.60, but due to a disparate way difference

$$\Delta r = b \cdot \sin(\phi) \sin(\theta) \tag{2.76}$$

and therefore the phase difference

$$\beta_m = (m-1)\beta = (m-1)\frac{2\pi b}{\lambda} \sin(\phi) \sin(\theta) \tag{2.77}$$

between radiator 1 and m.

Analogical to section 2.7.2 one now finds

$$C_{g_r} = \left| \frac{\sin\left(\frac{m\beta}{2}\right)}{\sin\left(\frac{\beta}{2}\right)} \right| = \left| \frac{\sin\left(\frac{m\pi b}{\lambda} \sin(\phi) \sin(\theta)\right)}{\sin\left(\frac{\pi b}{\lambda} \sin(\phi) \sin(\theta)\right)} \right| \tag{2.78}$$

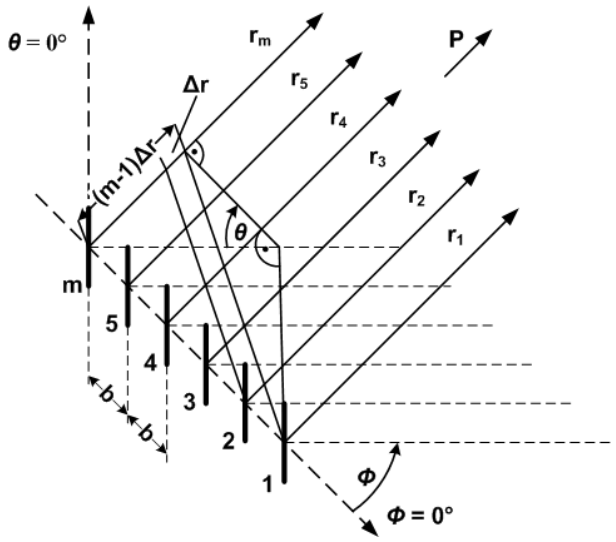

Fig. 2.8. Horizontal row aligned radiators

for the group characteristic of m radiators aligned in a row ($\phi = 90°$) and the total characteristic

$$C_{tot_r} = C_e \cdot C_{g_r} = C_e \left| \frac{\sin\left(\frac{m\pi b}{\lambda}\sin(\phi)\sin(\theta)\right)}{\sin\left(\frac{\pi b}{\lambda}\sin(\phi)\sin(\theta)\right)} \right| \tag{2.79}$$

while the indeterminate forms for e.g. $\phi = 0°$ and $\theta = 0°$ may again be solved by the L'Hospital's rule to

$$\lim_{\phi \to 0°, \theta \to 0°} C_{tot_r}(\phi, \theta) = C_e \frac{m \cdot \cos\left(\frac{m\pi b}{\lambda}\sin(0°)\sin(0°)\right)}{\cos\left(\frac{\pi b}{\lambda}\sin(0°)\sin(0°)\right)} = m \cdot C_e \tag{2.80}$$

2.7.4 Array characteristic

The observed array in this thesis will be placed in the plane of x- and y-axis thus one achieves the overall array characteristic by the product of equations 2.74 and 2.79

$$C_a(\phi, \theta) = C_e(\phi, \theta) \cdot \left| \frac{\sin\left(\frac{n\pi a}{\lambda}\cos(\phi)\sin(\theta)\right)}{\sin\left(\frac{\pi a}{\lambda}\cos(\phi)\sin(\theta)\right)} \right| \left| \frac{\sin\left(\frac{m\pi b}{\lambda}\sin(\phi)\sin(\theta)\right)}{\sin\left(\frac{\pi b}{\lambda}\sin(\phi)\sin(\theta)\right)} \right| \tag{2.81}$$

and for the indeterminate form for $\theta = 0°$ due to equations 2.75 and 2.80

$$\lim_{\theta \to 0°} C_a(\phi, \theta) = nm \cdot C_e \tag{2.82}$$

Equation 2.81 equals to the considerations in [Sti84], [Mai94] and [Bal05].

2.7.5 Planar array with element phase offset

As the point P not mandatory has to be placed in direct broadside of the array, thus a phase difference between Δr separated elements may now be written as

$$\beta = \psi + \frac{2\pi\Delta r}{\lambda} \tag{2.83}$$

where ψ is the phase-offset needed to steer the main beam to point P.
Therefore for electric beam-steering a distinct distribution of phase or time delay over the whole array for the single array elements is needed.
With consideration of a phase delay the total array characteristic may be written as

$$C_a(\phi,\theta) = C_e \left| \frac{\sin\left(n(\frac{\psi_c}{2} + \frac{\pi a}{\lambda}\cos(\phi)\sin(\theta))\right)}{\sin\left(\frac{\psi_c}{2} + \frac{\pi a}{\lambda}\cos(\phi)\sin(\theta)\right)} \right| \left| \frac{\sin\left(m(\frac{\psi_r}{2} + \frac{\pi b}{\lambda}\sin(\phi)\sin(\theta))\right)}{\sin\left(\frac{\psi_r}{2} + \frac{\pi b}{\lambda}\sin(\phi)\sin(\theta)\right)} \right| \tag{2.84}$$

Alternatively the necessary phase-offset may also be evoked by time delay.

2.7.6 Sidelobe level

Additional to section 2.2 now the sidelobe attenuation for an array basing on a squared grid structure with its superposition equation 2.84 is evaluated.

The group characteristic in equation 2.73 determines besides the maximum and nulls also the position and attenuation of the sidelobes depending on the amount of elements. The maximum of the numerator of the normalized equation 2.73

$$C_g = \left| \frac{\sin\left(\frac{n\beta}{2}\right)}{n \cdot \sin\left(\frac{\beta}{2}\right)} \right| \tag{2.85}$$

besides the main lobe is achieved for

$$\frac{\pi a}{\lambda} = \pm\frac{(2l+1)\pi}{2n} \tag{2.86}$$

where l is the order of the sidelobe relative to the main lobe. Thus one may write now

$$C_{gsl} = \left| \frac{\sin\left(n\frac{(2l+1)\pi}{2n}\right)}{n \cdot \sin\left(\frac{(2l+1)\pi}{2n}\right)} \right| = \left| \frac{1}{n \cdot \sin\left(\frac{(2l+1)\pi}{2n}\right)} \right| \tag{2.87}$$

For the first sidelobe ($l = 1$) of an array of $n = 100$ elements one gets

$$C_{gsl_1} = \left| \frac{1}{100 \cdot \sin\left(\frac{3\pi}{200}\right)} \right| = 0.21229 \tag{2.88}$$

and thus a sidelobe attenuation of

$$a_{sl} = 20\log_{10}\left(C_{gsl_1}\right) = -13.46\,dB \tag{2.89}$$

This attenuation is yet the greatest possible for a uniformly illuminated line source or a squared grid structure respectively. The proof is done for an infinite amount of elements $n \to \infty$ where one may write

$$a_{sl_\infty} = 20\log_{10}\left(\lim_{n\to\infty} C_{gsl}\right) = 20\log_{10}\left(\left|\frac{1}{\frac{(2l+1)\pi}{2}}\right|\right) \tag{2.90}$$

and therefore for the first sidelobe a maximum attenuation of again

$$a_{sl_\infty} = 20\log_{10}\left(\frac{2}{3\pi}\right) = -13.46\,dB \tag{2.91}$$

which agrees well with the value in table 2.1.

Chapter 3
Modelling with NEC

The following chapter deals with the used simulation software for the evaluation of antenna structures, starting in chapter 4 with an individual array antenna and continued in chapter 6 with various array structures.

3.1 Numerical Electromagnetic Code

The Numerical Electromagnetic Code (NEC) is a user-oriented software package developed by Lawrence Livermore National Laboratory. NEC bases on Method of Moments (MoM) code for analyzing the interaction of electromagnetic waves. Within NEC arbitrary conducting structures, formed by wires and subdivided in segments, may be modelled.

The purpose of NEC has been the analyze of electromagnetic response of antennas and scatterers. The code bases on the numeric solution of integral equations by the Method of Moments with the combination of integral equation of electric-field modelling thin wires and of magnetic-field for conducting surfaces.
The antenna structures in the models may be excited by voltage sources, which will be used within this thesis work, plane waves, lumped or distributed loadings, networks and transmission lines.
The output data of NEC contains current distributions, impedances, power input,

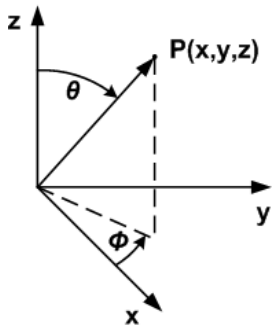

Fig. 3.1. Coordinate system

dissipation, efficiency and radiation patterns with gain or cross section.
The used coordinate system is equal to the earlier introduced in this thesis work and shown in figure 3.1.

3.2 Program history

The NEC-4-kernel, used at the Leibniz-Institute of Atmospheric Physics and kindly provided for this thesis work, has several improvements to the earlier used NEC-2-kernel, e.g. in [Ren06].

The NEC Method of Moment code grew out of an advanced version of the Antenna Modeling Program (AMP), which has been developed as research project in the early 1970's by MBAssociates for several U.S. military organizations.
Since the NEC-2-kernel the software is capable of lossy ground consideration (Sommerfeld-integral), which especially has significant influence to an antenna structure without reflector in relative its considered wavelength proximity to e.g. the earth's surface or other medium relative.
NEC-3-kernel included enhancements for modelling totally or partially ground buried wires and methods to decrease necessary computation time.
Within the NEC-4-kernel accuracy has been improved and e.g. further improvements of electrically small models were included.

3.3 Method of Moments

The integral equations for electric and magnetic field are solved numerically with the Method of Moments, by point matching of the fields, which is also represented by the Green's-function. The distribution of sources and the evaluation of their fields is the computational core, together with the solution of the matrix equation.
The Method of Moments applies to a general linear-operator equation with a known excitation, a linear operator and the unknown response, which is a sum of basis functions and linear equations, including weighting functions. The choice of basis and weighting functions determines the efficiency and accuracy of the Method of Moment solution. Basis functions are generally chosen as rectangular pulses of linear or sinusoidal functions or polynomials.
The intent of NEC is to generate a likely distribution of currents on the modelled wires, subdivided into segments, and thus obtain the evoked fields.
Depending on the distribution of the voltage sources and their resulting currents and the interaction with other sources the distribution of electric field is calculated. Within NEC electric far field as well as near field can be calculated.
With the aid of an optimized interpolation of pre-computed Sommerfeld integrals NEC2

reduces the necessary computation time, otherwise a double integration over the current distribution of the whole model would be needed. These pre-computed Sommerfeld integrals are used as table look-up in the numerical integral computation.
The Moment Methods resulting matrix equation is solved by factoring the matrix into a product of upper and lower triangular matrices by Gauss elimination. The two matrices are afterwards solved by forward and backward substitution. The computation time for matrix factoring is proportional to the matrix order cubed. In case of symmetry structures decomposing the solution into a sum of eigenmodes, which decrease solution time and needed memory. Solving the smaller eigenmode matrix equations derives the solution of the greater matrix. The matrix furthermore may be solved by the aid of LU-decomposition leading to a partitioned-matrix solution, called Numerical Green's Function (NGF).

3.4 Simulation process

For all models simulated during this thesis work the double precision (64 Bit) mode of NEC-4 has been used.
The models have been created and error checked in the GNEC Windows based version of NEC-4 and mainly been calculated on the IAP's SGI linux scalar computer mainframe consisting of up to 64 CPU cores and 192 GB main memory with the compiled fortran NEC-4 code, depending on the parameter of the model.
The analysis and evaluation of NECs output raw data been processed by the aid of MATLAB.

In the original NEC-code provided by Lawrence Livermore National Laboratory, the maximum definable amount of input lines in the models and thus also the number of radiating sources is restricted to 999, which leads to maximum of less than 500 array elements. This limit has been modified after correspondence with Gerald Burke, main developer of the NEC-code.

3.5 NEC statistics

This section shall present a small statistic on the amount models and their necessary calculation time depending on the complexity.

During this M. Sc. thesis work a total number of roughly 300 NEC models have been generated, resulting in about 400 output data files and about 3.2 GB data including derived pictures.

Figure 3.2 shows a graph of the time and memory consumption for a selection of models that have been evaluated during this Master thesis.
The time consumption for the computing of NEC models rises exponential with their

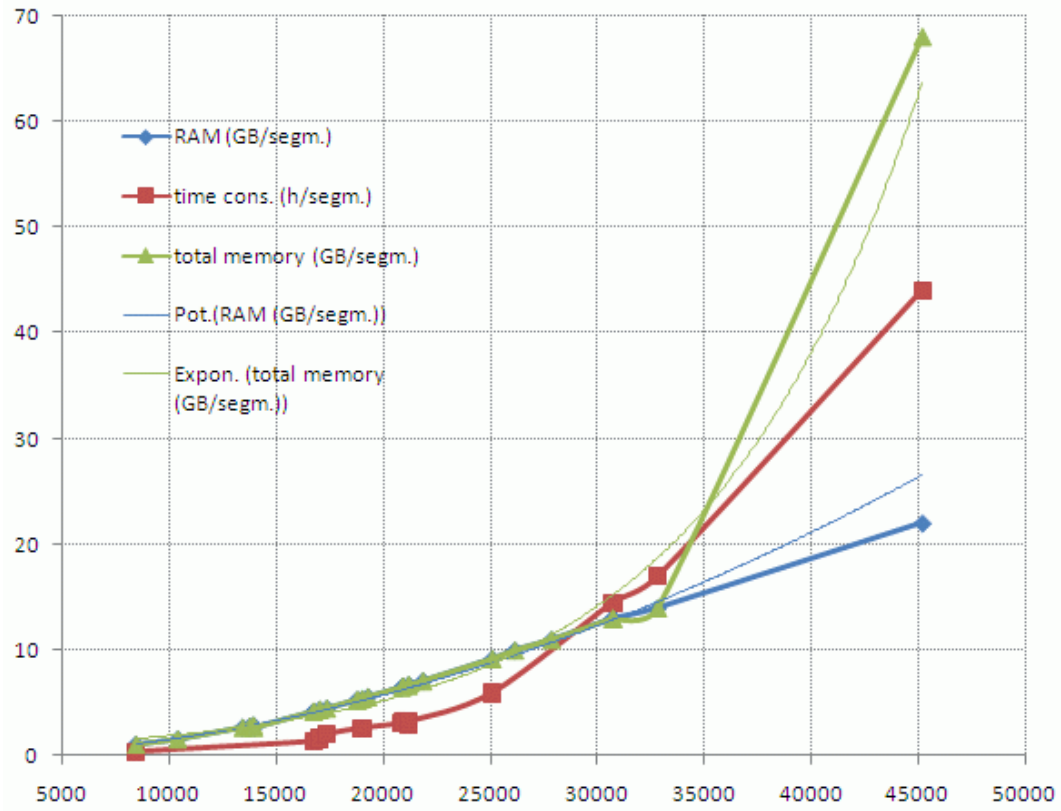

Fig. 3.2. Time and memory consumption for NEC-models

complexity. The necessary amount of main memory increases with a square dependency. The total memory for the largest models, 2500 array elements and respectively approximately 45000 NEC wire segments, increased rapidly, as main memory and hard disk memory had to be used, leading to an exponential dependency.
With the aid of this results one may suggest the necessary memory and time consumption for the envisaged array of 10000 elements.

Chapter 4

Modelling of a single array element

The following section deals with the design of a single array element, actually a yagi antenna, that finally was used for the antenna array discussed in chapter 6.
In this thesis work neither the characteristic and genesis of an antenna in principle nor of a yagi style antenna is discussed.
Details for it can be found in e.g. [MG86], [Bal05], [Kar06], [Sko70], [JJ93], [Sti84] and a summary is given in [Ren06].
The typical characteristics of an antenna have been introduced in chapter 2.

The objectives of this thesis work have been given as to design a small broadband yagi with the following parameters:

- Specification and analysis of at least one, if possible two, short (3-4 elements), X-Yagi antenna(s) having the following characteristics:
  - Center frequency 235.0 MHz
  - Feed-point impedance 50+j0 ohms at center frequency
  - Bandwidth (specified as s_{11} < -20 dB) > +/- 6 MHz
  - Circularity better than -1 dB out to 30° off-boresight, in all azimuth directions and over full bandwidth,
  - Gain at angles > 75° off-boresight as low as possible, but at least -16 dB,
  - Element lengths < 0.4 while maintaining all other characteristics,
  - Maximum relative gain at 40° off-boresight, consistent with all above points.

Furthermore it shall be induced circular polarization. Generating circular polarization may be achieved by usage of two linear orthogonally phased antennas. In case of orthogonally phased antennas both linear components should have the same point of emission. Generally this task is rather difficult to achieve, especially for higher frequencies, therefore one has to deploy a phase or time offset in the feeding network corresponding to the mechanical separation of the linear components.

$$\phi = \frac{ds}{\lambda} \cdot 360° \tag{4.1}$$

Not considering phase offset in this manner a mechanical offset of fed antenna elements leads to generation of an elliptical polarized wave.
To characterize antenna design properties the earlier introduced match indicating terms voltage standing wave ratio and the argument of the impedance itself are examined in closer detail.
In the tasks for the above repeated design limits for the single array element the desired bandwidth is mentioned as the scatter parameter s_{11}, which refers to the input return loss of the incident wave from the transmitter to the antenna. The input return loss may be converted to an voltage standing wave ratio by equation 2.13 and leads to

$$s = \left| \frac{(1 + 10^{\frac{a}{20}})}{(1 - 10^{\frac{a}{20}})} \right| \approx 1.22 \tag{4.2}$$

Additonally one may set a magnitude of e.g. 5 or 10 degrees of impedance argument to describe the phase bandwidth. In the following considerations a phase bandwidth of 5 degrees will be presented.
Considering the radiation pattern of an antenna design the gain, front/back- or front/rear-ratio and sidelobe attenuation are the most determining parameters and are therefore investigated.
Maintaining the above written characteristics three different designs have been created and are analyzed in the following. As the gain of the single antenna in a big array is of rather few importance it has been chosen to concentrate on 3-element yagi design. Nevertheless there have been valuable designs of 2- and 4-element yagi structures, which have been discarded during the design process. The reason to reject a 2-element design has been the lack of degrees of freedom to achieve the specific demands claimed for the single antenna. A 4-element yagi design appeared to be of less worth for the whole array as its gain may be significantly higher than of the chosen 3-element yagi. The more the single antennas 3 dB-beamwidth is narrowed the less degrees off bore-sight array beam steering permits under tolerable gain degradation. A 3-element yagi with a broadband design and moderate gain appeared to be the best compromise to achieve a good feasibility for off-boresight beam steering.
The radiation pattern of all three designs are shown in the appendix. In the first step the characteristics of the following designs are simulated for free space. The after all chosen design will be presented in section 4.2 including simulations for real ground environment.

4.1 Yagi designs

4.1.1 Yagi antenna design with a straight dipole as exciter

The dimensions of the first useful design are shown in table 4.1. Exciter of this design is a straight dipole as shown in figure 4.1, which leads to a low antenna impedance that has been set by the antenna structure to about 50 Ω. Both linear antenna structures are separated by 10 cm. This separation will be needed in the practical realization for mounting the dipole with the housing for the dipole terminals and eventually used balancing circuit at the antenna boom. Thus a feeding phase offset of 28° is needed to achieve circular polarization. Main focus at this design has been put to obtain a broadband antenna using a mechanical construction as simple as possible.
Table (4.2) shows major characteristics of this design.

Tab. 4.1. Mechanical structure - yagi with a straight dipole

element	mechanical length	position	diameter
reflector	66.0 cm	0.0 cm	3.0 cm
dipole	57.58 cm	22.8 cm	3.0 cm
director	46.32 cm	41.0 cm	3.0 cm

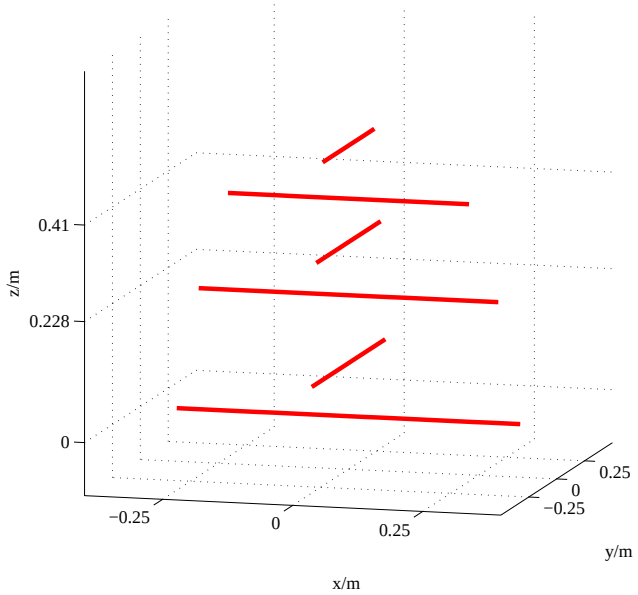

Fig. 4.1. Yagi design with a straight dipole, geometry 3D

Tab. 4.2. Characterstics - yagi with a straight dipole

impedance Z	50 Ω
gain	7.11 dBi
θ_3	89°
$attenuation_{40°}$	2.50 dB
$attenuation_{75°}$	7.85 dB
front/back-ratio	20,09 dB
bandwidth (a=-20 dB)	15.75 MHz (-8.50 / +7.25 MHz)
bandwidth ($\phi_Z = 5°$)	7.00 MHz (-3.75 / +3.25 MHz)

4.1.2 Yagi antenna design with a folded dipole as exciter

The first design with a simple straight dipole showed promising characteristics. Thus the main focus for further improvement has been to enlarge the broadband aspect. Therefore the exciter has been changed in this design to a folded dipole as shown in figure 4.2.

The dipole has been aligned vertically along the boom of the antenna as simulations

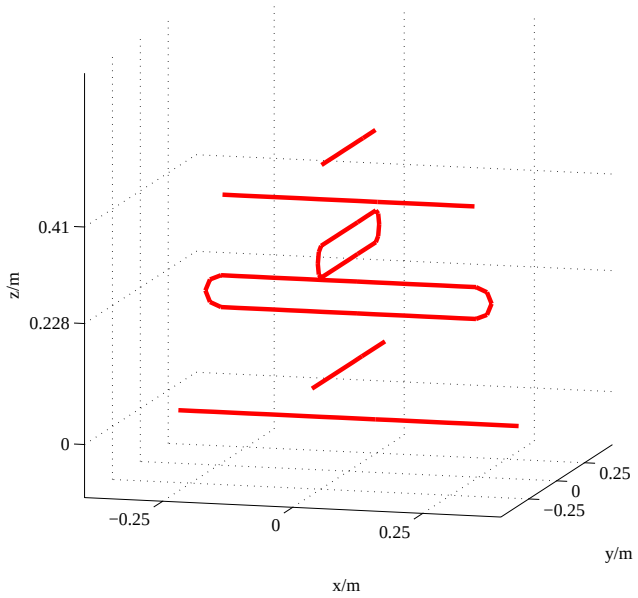

Fig. 4.2. Yagi design with a folded dipole, geometry 3D

pointed out a horizontally placed folded dipole has a significant influence on the orthogonally plane resulting in a mutation of impedance. The reason is obvious due to the dimensions of the folded dipole itself as it has a total length of 55 cm out of 2 cm thick tubular profiles with a separation of 6 cm which leads to a total width of 8 cm. Even the half of the width is occupied by the tubular aluminium profile. Such a described

structure within another orthogonally aligned linear antenna has a severe influence on the impedance, in terms of mutation, and the antennas radiation characteristics.
Due to the use of a folded dipole as radiator the antenna impedance is about 200 Ω, depending on the exact geometry of the involved antenna elements. The both linear antenna structures that form a circular polarization are separated 10 cm, which will be needed for the folded dipole itself and the weatherproof housing of the dipole terminals and feeding network. As a result of this 10cm separation a phase offset of almost 28° feeding phase-offset has to be used to obtain a circular polarization.
The major characteristics of the yagi design with a folded dipole are shown in the following table 4.4.

Tab. 4.3. Mechanical structure - yagi with a folded dipole

element	mechanical length	position	diameter
reflector	65.7 cm	0.0 cm	2.0 cm
dipole	55.0 cm	22.8 cm	2.0 cm
director	48.4 cm	41.0 cm	2.0 cm

Tab. 4.4. Characterstics - yagi with a folded dipole

impedance Z	200 Ω
gain	7.11 dBi
θ_3	89°
$attenuation_{40°}$	2.52 dB
$attenuation_{75°}$	7.79 dB
front/back-ratio	20,09 dB
bandwidth (a=-20 dB)	24.00 MHz (-12.75 / +11.25 MHz)
bandwidth ($\phi_Z = 5°$)	15.75 MHz (-9.00 / +6.75 MHz)

4.1.3 Yagi antenna design with angulated elements

The third design emerged from the desire to reduce the gain loss at higher off-boresight angle like 45°. Another aspect has been to create a physically small antenna in terms of its volume requirement. As a result the elements of the design three antenna have been severely angulated by −45° as shown in figure 4.3. Due to this style of element the necessary overall length of the antenna along the boom increased from almost 0,5 m to 0,7 m. While table 4.5 shows the physical length and position of the elements, table

Tab. 4.5. Mechanical structure - yagi design with angulated elements

element	mechanical length	position	diameter
reflector	66.0 cm	0.0 cm	3.0 cm
dipole	56.0 cm	22.8 cm	3.0 cm
director	46.2 cm	41.0 cm	3.0 cm

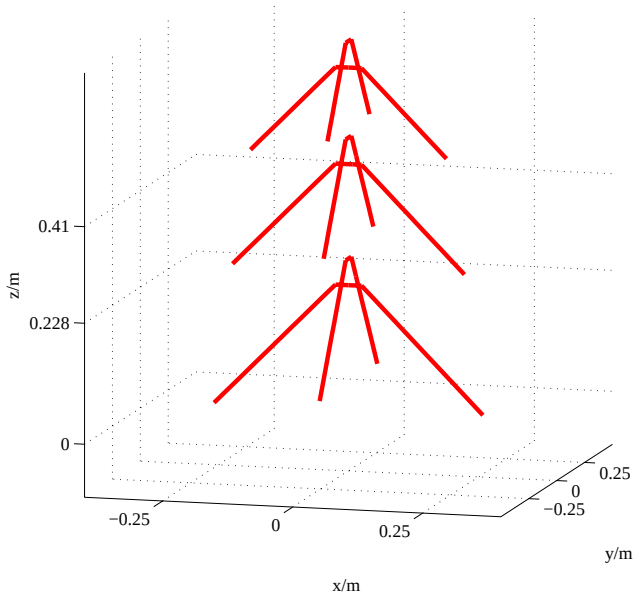

Fig. 4.3. Yagi design with angulated elements, geometry 3D

Tab. 4.6. Characterstics - yagi design with angulated elements

impedance Z	50 Ω
gain	4.84 dBi
θ_3	100°
$attenuation_{40°}$	1.91 dB
$attenuation_{75°}$	6.22 dB
front/back-ratio	17,34 dB
bandwidth (a =-20 dB)	10.75 MHz (-5.50 / +5.25 MHz)
bandwidth ($\phi_Z = 5°$)	5.50 MHz (-2.70 / +2.80 MHz)

4.6 summarizes the electromagnetic characteristics.

Table 4.6 reveals the influence of the antenna structure to its characteristics. Due to the angulated elements the maximum gain drops to 4.84 dBi while the beamwidth θ_3 rises by more than 10° in contrast to the design with a folded dipole. Consequently the attenuation at 75° off-boresight is quite low.
Enhancing the bandwidth of this antenna design by using a folded dipole as radiator

is obviously possible however this leads to a mechanical complicate and therefore cost intensive antenna structure as additional troubles in electrical and mechanical way are to be suspected.

4.2 Results of the design process for the single array element

The first design with a straight dipol is quite auspicious as it shows good pattern like gain, front/back-ratio, however attenuation of roughly 2.5 dB at 40° has to be considered. The bandwidth, defined by the return loss of -20 dB, of almost 16 MHz is considerably fair for an antenna with a straight dipole and thus yet achieves the given designing bandwidth limit.
Additional to this good characteristics of the first design, the secondly presented design with a folded dipole has been improved in terms of bandwidth by more than 8 MHz due to selection of a different radiator while other characteristics kept almost unchanged. The bandwidth required in the design tasks for the single array element has been ± 6 MHz, while $+11.25$ MHz and -12.75 MHz respectively could be achieved with the folded dipole yagi design.
The third design with its angulated antenna elements provides the lowest attenuation at 40° relative to the antenna boom of the three designs, which has been improved by 0.6 dB compared to the other designs. This is obviously favorable, but contrary to this a deficient attenuation at 70° appeared, which has been deteriorated by 1.5 dB compared to the other designs. Furthermore the worse front/back-ratio and the low bandwidth of 10.75 MHz in contrast to the earlier designs are major reasons to decline this design implying angulated elements.

In the design requirements an attenuation of at least 16 dB relative to the maximum radiation at high zenith angle ($> 75°$) have been claimed, which could not be achieved in any design model.
The greatest attenuation for $\theta = 75°$ could be derived for the first two designs with approximately 7.8 dB. However the demanded attenuation of 16 dB in general appears to be far out of any possibility for such an simple antenna geometry. To achieve attenuation levels such as 15 dB yagi antenna structures with at least 4 elements are needed to provoke nulls in the radiation pattern at the desired off-boresight angle.

Contrary to the demand of high attenuation at 75° off main beam is the claim of maximum gain for 40°. This is a limiting parameter for the complexity of the single

array element. To avoid severe losses at 40° off-boresight the single array element should not focus the emitted radiation severely. The consequence of this demand is a relative broad half-power beamwidth. With the first two designs with its straight and folded dipoles as excited element, a half power beamwith of roughly 90° could be achieved. In design with angulated elements 100° beamwidth could be reached. This results lead to an attenuation at 40° of -2.5 dB and -1.9 dB respectively relative to the maximum gain.

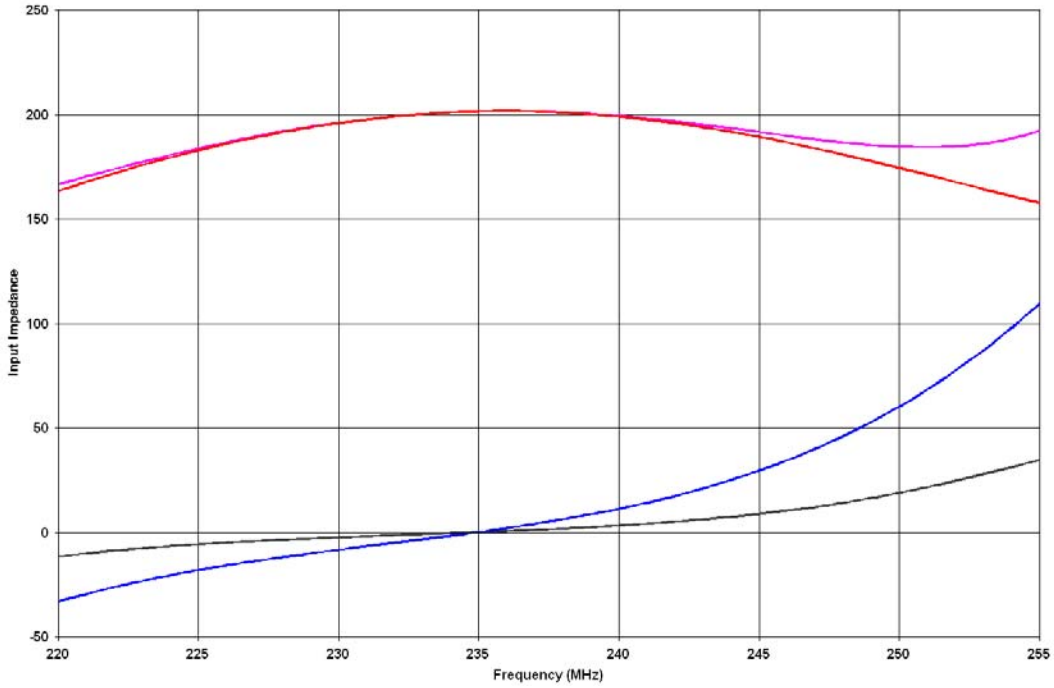

Fig. 4.4. Impedance and phase of the yagi design with a folded dipole

With a rather low attenuation of radiated power at zenith angles greater than 75°, for the single array element, the pattern of the whole array characteristic might be compromised likewise.
As for the considered zenith angles the radiation power is evoked close to the ground, is important for the evaluation of possible electromagnetic interference (EMI). In case of precautions due to EMI alternative methods might be necessary to consider depending on the resulting overall radiation pattern for the desired off-boresight beamforming.
A significant improvement for EMI would only be derived for far more complex single array elements, but on the other hand this leads to a smaller half-power beamwidth and thus to severe attenuation even at 23° off-boresight, where overall the greatest interest is appointed to. Additionally one has to be aware of modifying the antenna, in terms of optimizing its radiation pattern for a smaller beamwidth and improved gain,

leads simultaneously to a modification of the impedance and thus a loss of bandwidth.

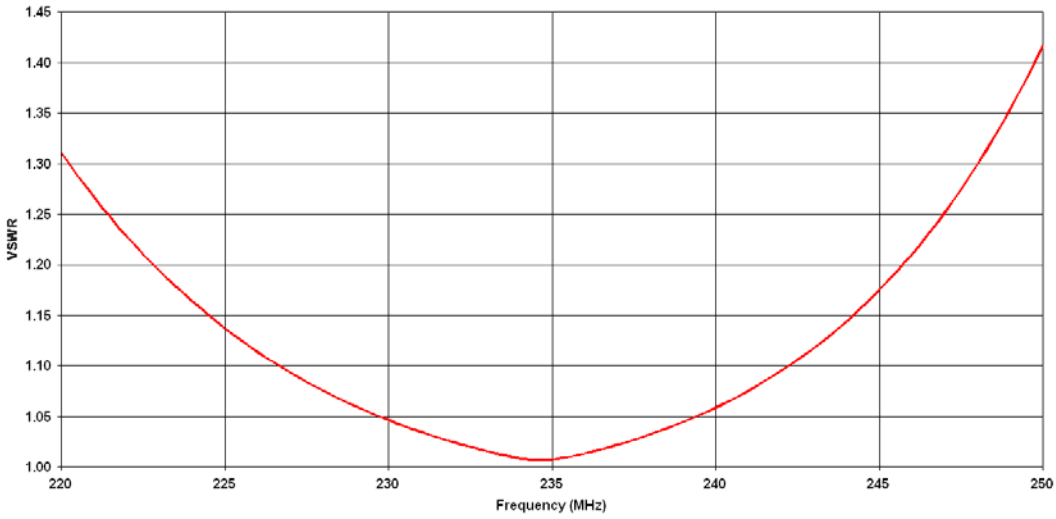

Fig. 4.5. VSWR of the yagi design with a folded dipole

After all considerations of the above quoted results and in agreement with Dr. Wannberg, the design with a folded dipole been chosen as it merges the demands for the best compromise.

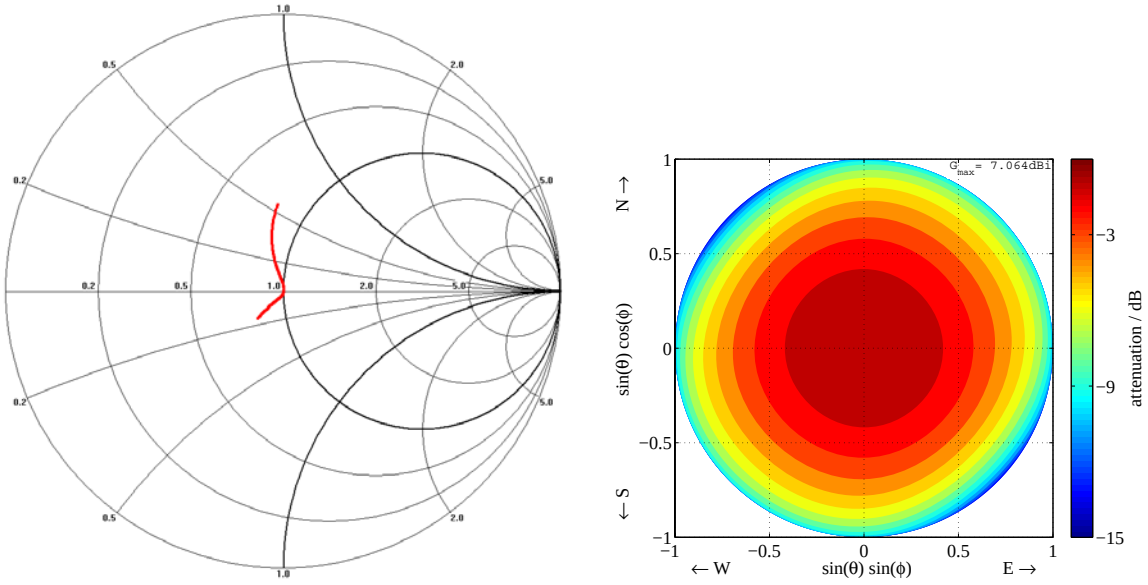

(a) Smith-chart impedance

(b) Radiation pattern, top view

Fig. 4.6. Characterstic of the yagi design with a folded dipole

Figure 4.4 depicts the impedance and phase chart over the frequency, where the blue, red and magenta graphs are the imaginary, real part and magnitude of impedance in Ω respectively, while the black graph depicts the impedance phase in °.
Around the desired frequency a quite flat section for real and imaginary part of the impedance could be achieved with the folded dipole yagi design.
Even more benefiting appears the phase distribution over the frequency. The phase drift between -9 MHz and +6 MHz referable to the center frequency is relatively low ($< \pm 5°$). Same impression can be taken from the smith chart in figure 4.6(a).
The resulting bandwidth, considering scatter parameter $s_{11} = -20\,\text{dB}$ and therefore VSWR $s \approx 1.22$, can be seen in figure 4.5.

The resulting radiation pattern of the chosen yagi design with its folded dipole exciter is shown in figure 4.6(b), where one can recognize an almost equal illumination. In figure 4.7 two radiation pattern for the cross section $\phi = 0°$, 4.7(a) for free space environment and 4.7(b) for real ground (arctic land), with its parameter $\epsilon_r = 3$ and $\sigma = 0.3 \cdot 10^{-3} \frac{S}{m}$, are shown. The change of angular scale has to be noted, referring to the fact that in the proximity of any ground no radiation in the far field can be evoked. The influence of the real ground appears to be seriously high, however it yet has to be quoted the ground influence to the whole array due to its higher directivity is less. The other cross sections are almost equal to $\phi = 0°$ as can be seen in figure 4.6(b).

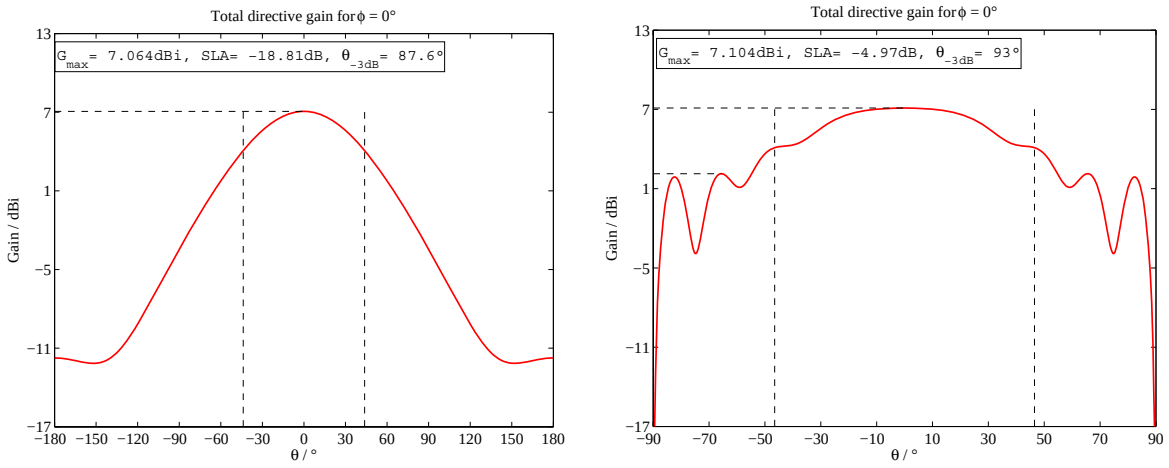

(a) Free space (b) Real ground

Fig. 4.7. Radiation pattern for yagi design with a folded dipole

The impedance Smith-Charts for the yagi designs with a straight dipole and with angulated elements are shown in figure A.4, the radiation pattern in top view are shown respectively in A.5.

4.3 Impedance match

The impedance $Z = 200\,\Omega$ of the chosen design may be transformed by a 4:1 wideband half-wave balun (balanced-unbalanced) made of coaxial cable (impedance $Z = 50\,\Omega$) to the typical coaxial feeding system of $Z = 50\,\Omega$. This kind of half-wave transformer is known since years in principle and spread in literature. Thus once the impedance is transformed to a fourth of its input magnitude and additionally is converted from balanced (dipole) to unbalanced (coaxial cable). The genesis and its practical layout of a 4:1 half-wave balun is shown in figures 4.8(a) and 4.8(b) corresponding to [Bor05] while figure 4.8(c) shows a practical realization for the folded dipole. The bandwidth of

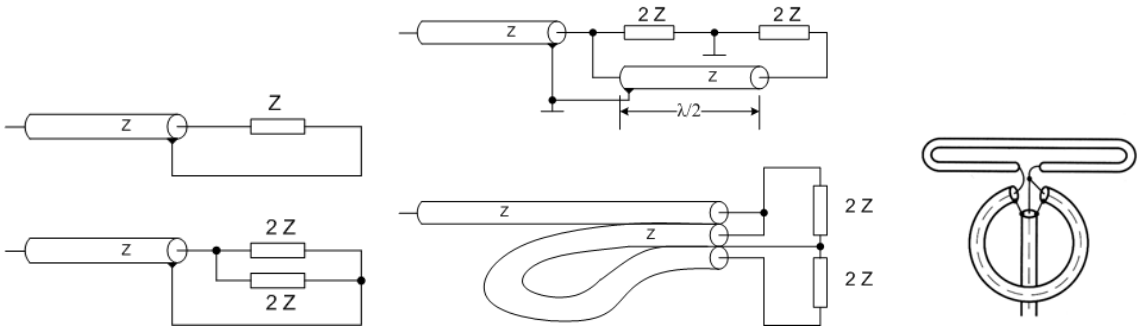

(a) (b) (c)

Fig. 4.8. Genesis of half-wave balun

this kind of 4:1 baluns is typically more than 100 MHz in the VHF-frequency spectrum.

Alternatively a quarter wavelength transformation in series with additional balancing. For this purpose the transforming coaxial cable with an impedance of

$$Z_{tr} = \sqrt{Z_{ant} \cdot Z_{sys}} = \sqrt{200\,\Omega \cdot 50\,\Omega} = 100\,\Omega \tag{4.3}$$

with Z_{sys} the feeding system impedance and Z_{ant} the antenna impedance, is needed, which is a rather unusual impedance of a coaxial cable, however e.g. $92\,\Omega$ impedance coaxial cable are available.
The alternative solution to use two parallel $200\,\Omega$ feeding cables, each could be realized with parallel open wires, is also not recommended.

4.4 Phase feeding

The needed phase-offset ψ_m due to mechanical offset mentioned in equation 4.1 and the additive phase-offset of $\psi_c = 90°$ between both linear parts to induce circular polarization has to be created. The needed phase-offset may e.g. be achieved by phase-shifters in form of coaxial cable of adequate length. Thus the higher mounted element may be fed by an electrically 38° longer feeding cable. Additionally for the EISCAT_3D project it's intended to use for every single linear antenna a separate transmitter, a waveform-generator and time delay units. Thus every linear element may be fed by almost every phase of the desired signal. This should make any additional phase-shifters needless and simplify the array feeding network.

4.5 Element correction due to proximity of boom

This section shall stress the need of correct the length of the mechanical elements of a single array element if it is passed through the metal boom, where all elements are mounted at.
This item has been evaluated in [Gra95] for VHF- and UHF-frequencies for boom diameter smaller than 0.055λ and presented a correction formula

$$c_b = 12.5975 \left(\frac{d_b}{\lambda}\right) - 114.5 \left(\frac{d_b}{\lambda}\right)^2 \tag{4.4}$$

where c_b is the correction factor for the elements as a fraction of the boom diameter, the booms diameter d_b given in meters.
Table 4.7 gives the resulting needed corrections for various boom diameter d_b where c_e is the needed element correction for the frequency 235 MHz.

Tab. 4.7. Element corrections

$d_b[mm]$	c_b	c_e [mm]
10	0.092	0.92
15	0.132	1.98
20	0.169	3.38
25	0.203	5.08
30	0.233	6.99

4.6 Weather effects to the antenna characteristic

As the EISCAT_3D radar shall be placed in high northern latitude the arctic influences of harsh weather have to be considered.
The potential risk of an antenna structure with a folded dipole aligned vertically in arctic surrounding - when antenna boom is almost or absolute vertical - is coverage of elements by highly humid snow. Such weather might lead to snow surfaces droop in the plane of the folded dipole from the upper tubular and even electrically shorten to the lower. But as in reality it mechanically won't be possible to align the dipole strictly vertical as the terminals have to be protected in a housing. Thus the probability of such an event is far less. If the antennas are even tilted to $\theta_t = 23°$ as claimed in the thesis tasks one no longer has to be concerned with this issue.
Another aspect of such snow surfaces across the dipole is the additional weight and wind load. However the additional wind load is almost to neglect as dipoles for the desired frequency are quite small and, depending on the elements mechanical mounting, should be very rugged. Obviously last considerations are valid as well for every antenna element with any kind of structure.
Snow and/or ice coverage leads to severe thickening of antenna elements which generally leads to a shift of resonance frequency. In the best case the resonance frequency just declines, but also the whole impedance and radiation pattern mutates depending on the thickness and electrical parameter of elements icing. Thus additional simulations of the chosen antenna have been done to determine the influence of ice layer on the antennas elements.

For the simulations sweet-water ice with a thickness of 3 mm, electrical parameters relative permittivity $\epsilon_r = 5$ and conductance $G = 0.0004\,\frac{S}{m}$ were used. These parameters have been taken from [DA89] and [Dan96] which have been measured at a frequency of 100 MHz.
The result of the simulation is presented in figure 4.9 as chart of the impedance and phase.
Considering the above written parameters the effect to the impedance is rather low. The real part drops by about 11 Ω while resonance frequency is almost unchanged which leads to a reflection coefficient (2.8) of

$$\Gamma = \left|\frac{200 - 188}{200 + 188}\right| \approx 0.031 \tag{4.5}$$

The resulting chart for the voltage standing wave ratio is shown in figure 4.10. As the bandwidth of the antenna is greater than necessary one could think about resonance shift of the antenna to a slightly higher frequency, by modification of the antenna structure, to obtain a greater spare bandwidth to higher frequencies. This also comes along

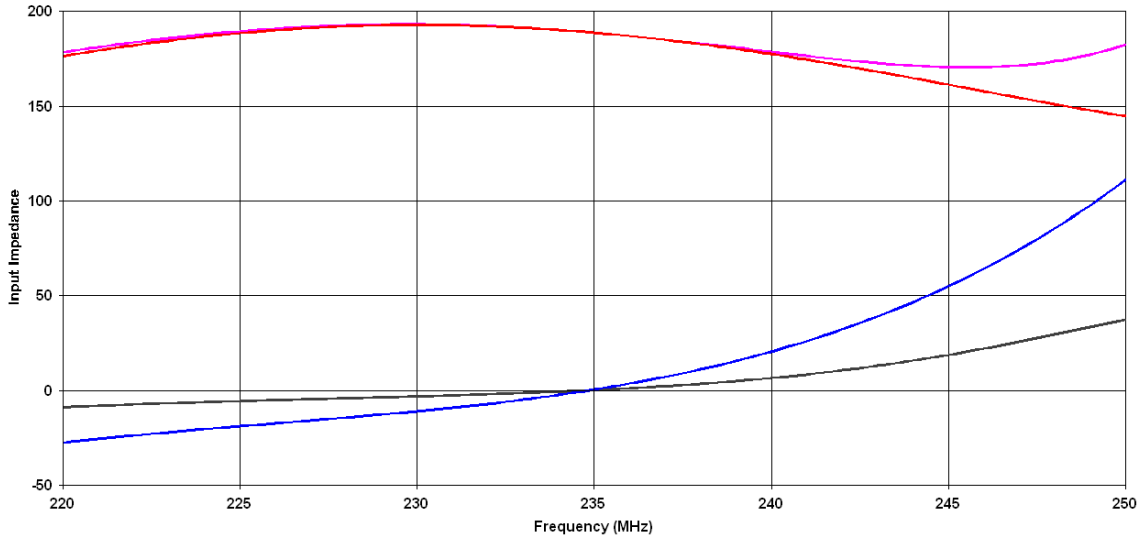

Fig. 4.9. Impedance and phase of the yagi design with a folded dipole and ice cover

with the typical greater increase of VSWR or contrariwise for the return loss for higher frequencies than for lower frequencies for optimized yagi antennas and would therefore arrange a more central positioning of the desired usage frequency within the VSWR or equivalent return loss graph.

Significantly higher influence and de-tuning of the antenna appears for a greater rela-

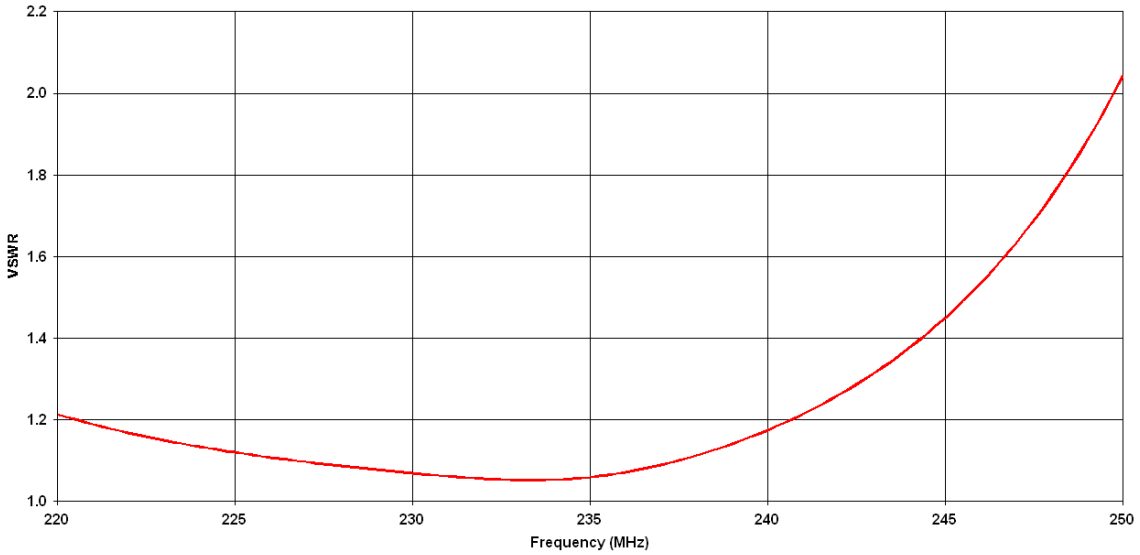

Fig. 4.10. VSWR of the yagi design with a folded dipole and ice cover

tive permittivity ($\epsilon_r = 30 - 80$) like water has. But as it's almost impossible the whole antenna sustains a uniform water cover thus such a severe de-tuning may be neglected. Far more likely high humidity like fog provokes water drops on the elements which don't

have cognizable influence considering the ratio of element diameter to wavelength

$$\frac{d}{\lambda} = \frac{0.02m}{1.2757m} \approx 0.016 \tag{4.6}$$

which is considerable high and therefore only few influences are to expect. Furthermore the large overall bandwidth of 24 MHz ensures sufficient spare if impedance gets mutated and thus the optimum match spectrum is displaced.

In the following the yagi design with the folded dipole is used as single antenna for any further considerations and evaluation of the array structure.

4.7 Polarization error

NEC offers the calculation of polarization for a given geometry of a radiating source for a spherical surface. The polarization have been simulated for a distance of almost 40 wavelength and thus the results clearly belong to the far-field.

The chosen individual antenna (section 4.1.2) has been excited by a phase of 0° on one linear part and the other linear part by 62° of same magnitude to induce circular polarization. The phase of 62° for on linear part refers to the necessary phase-offset due to mechanical offset of both linear antenna parts.

The magnitude of polarization angle varies in the maximum for zenith beaming ($\theta = 0°$) between almost 90° around the azimuth angle $\phi = 0°$ to 86.47° for e.g. azimuth $\phi = 66°$ and $\phi = 246°$, where the polarization error reaches 4%.
For $\theta = 30°$ off-zenith the magnitude of polarization angle changes to 84.21° e.g. for the azimuth $\phi = 157.5°$, which means an polarization error of 6.5%.

A graph of the polarization results is shown in figure 4.11 as polarization angle over the azimuth angle ϕ for the zenith angle $\theta = 0°$ and $\theta = 30°$.

4.8 Practical realization

All elements and mounting of the antenna should be made of stainless material. The elements of the antenna made of aluminium alloy, providing good stability, flexibility, corrosion resistance. A possible alloy is the derivative AlMgSi, an alloy of aluminium,

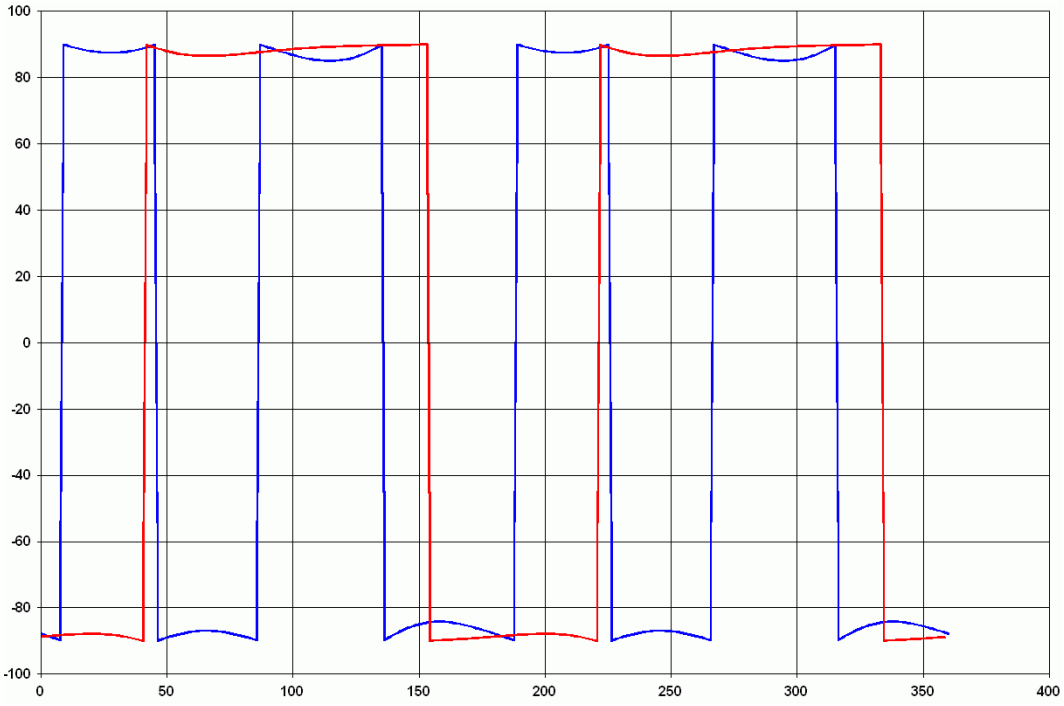

Fig. 4.11. Polarization of yagi design with a folded dipole, red: $\theta = 0°$, blue: $\theta = 30°$

magnesium, silicon. The exact derivative may be chosen on the need of corrosion resistance and flexibility.

The elements of the antenna may be mounted either isolated or not in terms of conductive mounting to the boom. In case of isolated elements its holders may be made of PTFE (Polytetrafluoroethylene) or any other polymer material electrically almost equal to it like POM (Polyoxymethylene), with additional good mechanical characteristics. Less qualitatively materials like e.g. PE (Polyethylene) shouldn't be used, as it's mechanically insufficient, especially if any element holders shall be milled.

If the elements are mounted electrically conductive to the boom, a permanent assembly has to be ensured.

The dipole may be mounted to the boom opposite to the feeding terminals without change of characteristics, which can be proved due to figure 4.8(b). The feeding terminals should be placed in a sealed weatherproof housing. If this housing is chosen in sufficient size, the half-wave balun may be placed inside. The half-wave balun should be made of a high quality coaxial cable with sufficient power handling capability and low seasoning. A useful coaxial cable for this purpose could be the standardized RG-142 B/U, with power ratings over 1000 W at the desired frequency, dielectric made of PTFE and double shielding. The only degradation is the solid inner conductor, which may break under periodic mechanical stress, however this is very unlikely if the balun is placed inside the housing.

As the dipole will likely be made of aluminium it has to be cared for a enduring conductive contact of the feeding and balun coaxial cable. Therefore leads could be soldered or crimped to the terminals of the dipole.
The connection from the dipoles terminal leading to the balun and the main coaxial cable may be done by a short piece of braid, which would reduce any mechanical stress on the leads and the inner conductor of the coaxial cable.
For the main coaxial cable coming from the transmit-receive cabinet a plug either mounted at the bottom side of the housing or performed as a coaxial cable plug on a short non-impedance-transforming cable weather-proof passed through the housing. Obviously each antenna should have the same electric length from the dipole terminals to the plug of the main coaxial cable. The same applies for the main coaxial cable from the antennas to the transmit-receive cabinets. High quality cable with low loss, e.g. 1/2 inch diameter or greater, of equal electrical length should be used. However within the transmit-receive units the original phase could be reestablished, but causes additional complexity.
The housing openings are to be sealed with washers. It additionally proofed worthwhile to drill a small hole in the most bottom part of the housing, antenna mounted in it's desired alignment, to obtain a marginal interchange of air to avoid any condensate inside the housing.
For all elements passed through the boom or are mounted very closely to a significant thick boom, a correction of element length as described in section 4.5 has to be taken into account.

4.9 Gain correction

As in equation 2.84 the gain variation depending on the spacing is not represented, a gain correction has been introduced.
Therefore simulation with NEC for various spacings between $0.5\,\lambda$ and $1.15\,\lambda$ for a group of the chosen single array element antenna provided a gain correction equation

$$g_{kor} = -0.6749d^2 + 1.1193d + 0.5355 \tag{4.7}$$

depending on the spacing d.

This gain correction has been used as an option within the superposition calculation with MATLAB, where simulations using NEC either have not been possible anymore or as comparison to the results of NEC.

Chapter 5

Mutual coupling of closely aligned antennas

This section deals with mutual coupling which outlines the relationship of closely aligned antennas.
Worthwhile basics regarding mutual coupling may be taken from [Bal05] and [TMB82].
The gain of an array is related to its individual elements. The behavior, especially the gain and the radiation pattern, of an isolated antenna may be significantly different from the same element being part of an array. This behavior also occurs for elements depending on their position in an array, being located in the center or opposed at the edges. Such effects are due to mutual electromagnetic coupling in the form of energy transport between the elements which leads to more or less element gain, modified element pattern or even impedance mutation in the array proximity.
Mutual coupling depends on the radiation characteristics, the relative separation between the elements, herein after referred to as spacing and the relative orientation of each array element and the strength of the directly or reradiated fields.
One way to observe and evaluate mutual coupling is to excite one element of an array while every element else is terminated in matched loads. The overall radiation pattern consists of the excited element pattern and the group pattern affected by the terminated elements, that has been illuminated by the excited element. Thus the terminated elements reradiate fields which are combined with the original excited wave to form the overall radiation pattern.
The mutual coupling depends on the element gain, radiation pattern, the spacing and orientation of the elements to each other.
To evaluate mutual coupling effects of array elements, one may observe the change of radiation pattern, which generally is a good indicator and visual proof for mutual coupling. Furthermore one may appraise the induced currents of the terminated elements by the excited one. The magnitude of the induced currents reveals a useful criterion to evaluate the mutual coupling.
For this thesis the lately mentioned method has been chosen and afterwards been proved by the NEC internal calculation of maximum coupling. The models are simulated by NEC initially for free space environment to distinguish the pure mutual coupling of the elements. Partially results of simulations for real ground environment (arctic land) using Sommerfeld/Norton method are presented and compared for the most interesting scenarios. The output file, especially the current distribution on the array, is read by MATLAB and the coupling is calculated. The excited element is always radiating a

circular wave. For almost equal but linear polarized array elements considerable differences in coupling may appear.
Successive the EISCAT_3D related most likely and most interesting orientations and spacings of the chosen single element antenna are evaluated.
The coupling rates for each element are shown in tables, which have been placed in the appendix. However the statistical data are shown within the following sections, which underline the general characteristics.

5.1 Array elements oriented to $\phi_e = 0°$ on a squared grid

The first investigated array is exemplary shown in figure 5.1(a), the crossed elements are aligned to $\phi = 0°$ (marked by ϕ_e as elements alignment) and orthogonally on a squared grid structure with spacings of 0.6 up to 0.75 wavelengths, while array elements are oriented to zenith, a schema is shown in figure 5.2.

Figure 5.1(a) shows the array with a spacing of 0.7 wavelength and elements are

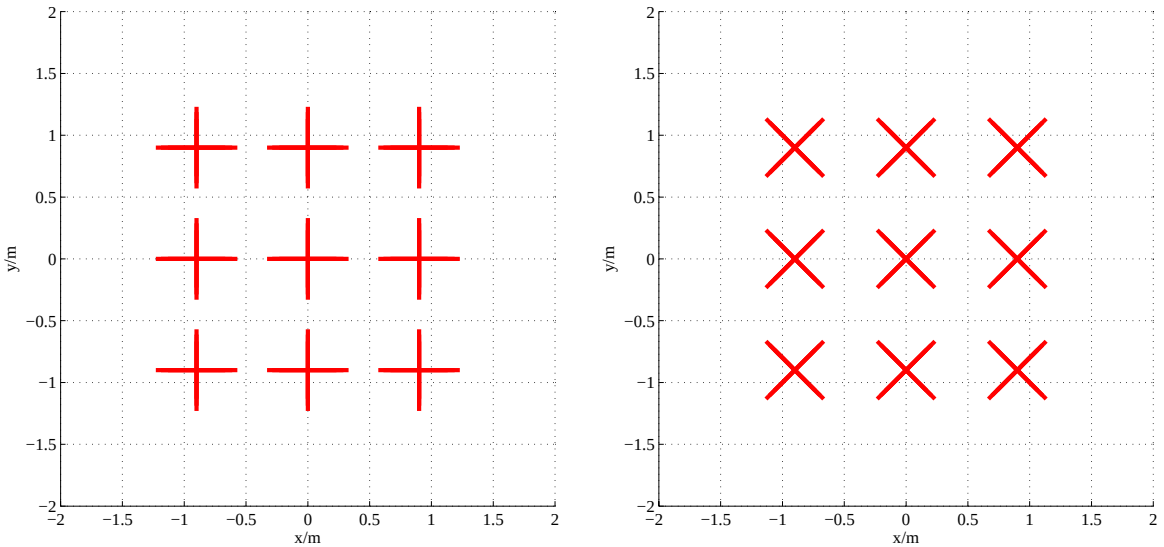

(a) $\phi_e = 0°$ (b) $\phi_e = 45°$

Fig. 5.1. Mutual coupling array, squared grid, top view

orientated to $\phi = 0°$ and $\phi = 90°$ respectively. The excited element is placed in the middle of the observed array, formed by linear elements 9 and 10, radiates a circular wave. Table A.1 shows the obtained coupling c_{fs} to all the remaining elements for free space environment while table 5.1 presents the minimum and maximum, mean value

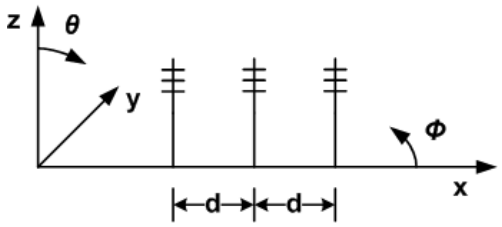

Fig. 5.2. Array elements oriented to zenith

of mutual coupling $\overline{c_{fs}}$ and its standard deviation $\sigma_{\overline{c_{fs}}}$.

In the beginning one may suggest the coupling in general decreases with distance to

Tab. 5.1. Mean value and standard deviation of mutual coupling for squared grid, elements oriented to $\phi = 0°$

spacing	$\max[c_{fs}]$	$\min[c_{fs}]$	$\overline{c_{fs}}$	$\sigma_{\overline{c_{fs}}}$
0.6 λ	-35.7 dB	-49.1 dB	-41.0 dB	5.8
0.65 λ	-38.3 dB	-52.4 dB	-46.0 dB	5.6
0.7 λ	-39.8 dB	-60.5 dB	-50.7 dB	7.0
0.75 λ	-39.8 dB	-69.6 dB	-53.4 dB	9.7

the radiating source. This is only particular true as elements are spaced very close and near electric field acts in a major role.

The mutual coupling is overall reasonably low, even for the lowest spacing distance of $d = 0.6\lambda$ the coupling exceeds only -35.7 dB in the maximum, while its minimum is about -49 dB with a mean value of -41 dB. As the lowest mutual coupling between the array elements is wanted it is advantageous to increase the spacing. At a spacing of $d = 0.7\lambda$ the maximum coupling saturates with -39.8 dB, while the minimum declines for even greater spacing as $d = 0.7\lambda$ to -69.6 dB. However the standard deviation attests the increase of mutual coupling differences over all elements.

The mean value $\overline{c_{fs}}$ of mutual coupling, shown in table 5.1, generally decreases with the spacing of elements (-35.7 dB to -39.8 dB), however the standard deviation $\sigma_{\overline{c_{fs}}}$ in principle rises likewise (5.8 to 9.7) which underlines the coupling differences between the linear parts of illuminated elements. While spacing is enlarged coupling to one linear part of an element is decreased but contrary the coupling to the orthogonally part is saturating or even increasing again, e.g. element 8. One can see the differences in mutual coupling from one element to its orthogonally aligned element with up to 22 dB, e.g. elements 15 and 16, these differences mainly increase with the spacing.

An array geometry like presented in figure 5.1(a) gives best (most equal) decoupling for the considered antenna element at a spacing of about 0.65λ as standard deviation of the mutual coupling is at its lowest.

The optimum of spacing for this array alignment one may choose between $d = 0.65\lambda$ and $d = 0.75\lambda$ depending on the other demands like beam swinging or maximum gain, while $d = 0.7\lambda$ shows a worthwhile compromise.
Any larger spacing in the observed range initiates a partially increased coupling.

For the excited element the maximum mutation of impedance in this array arose for a spacing of 0.7λ and reached $Z = (189.4 - j17.1)\,\Omega$. This impedance corresponds to a VSWR $s = 1.11$. The minimum mutation of impedance appeared for a spacing of 0.6λ to $Z = (210.2 - j2.1)\,\Omega$ and $s = 1.05$.
Conspicuous is the high capacitance, which might be interpreted as high coupling effects.

5.2 Array elements oriented to $\phi_e = 45°$ on a squared grid

For the next study each single element has been rotated by 45° as it's shown in 5.1(b), the linear elements are now aligned to $\phi = 45°$ and $\phi = 135°$ respectively. The spacing is again varied in the range of 0.6 to 0.75 wavelengths. The results for mutual coupling c_{fs} out from the radiating elements 9 and 10 are presented in table A.2.

Tab. 5.2. Mean value and standard deviation of mutual coupling for squared grid, elements oriented to $\phi = 45°$

spacing	max$[c_{fs}]$	min$[c_{fs}]$	$\overline{c_{fs}}$	$\sigma_{\overline{c_{fs}}}$
0.6 λ	-32.6 dB	-55.5 dB	-44.5 dB	7.8
0.65 λ	-35.5 dB	-57.9 dB	-47.5 dB	7.8
0.7 λ	-39.0 dB	-60.5 dB	-51.0 dB	7.7
0.75 λ	-41.1 dB	-62.9 dB	-53.1 dB	8.0

This array geometry provides a more equal coupling of the elements which underlines the standard deviation $\sigma_{\overline{c_{fs}}}$ of the calculated coupling in the mentioned range. However the standard deviation $\sigma_{\overline{c_{fs}}} = 7.7$ is greater than in structure 1 for the same spacing.
The mean of coupling $\overline{c_{fs}}$ decreases from almost -55 dB down to -63 dB, while spacing is increased. Thus the mean value of mutual coupling in this structure with elements aligned to $\phi = 45°$ is about 3.5 dB lower for a rather close spacing of $d = 0.6\lambda$. This gain drops with the spacing as the minimum of coupling doesn't exceed the level of structure 1. However the maximum coupling is improved by more than 1 dB for a

spacing of $d = 0.75\lambda$.
The advantage of this structure is the very equal coupling over all elements and different spacings, extraordinary coupling differences of 22 dB like found in structure 1 are not to be expected. Thus this structure exhibits to be a more reliable overall system.
Compared to geometry depicted in figure 5.1(a) the actually focused element alignment proves to be valuable for a spacing of $d = 0.7\lambda$ to $d = 0.75\lambda$.

The maximum impedance mutation in this array arose for a spacing of 0.6λ and reached $Z = (229.8 - j6.2)\,\Omega$. This impedance corresponds to a VSWR $s = 1.15$. The mutation of impedance decreased with the increase of spacing to $Z = (189.6 - j8.6)\,\Omega$ and $s = 1.07$.

5.3 Array elements oriented to $\phi_e = 45°$ on an equilateral grid

In this section follows the evaluation of an array basing on equilateral triangular grid as figure 5.3(a) presents. The linear elements are aligned to $\phi = 45°$ and $\phi = 135°$ respectively, the spacing is varied from 0.6 to 0.75 wavelengths. Elements 7 and 8 are excited to form a circular wave. The mutual coupling to the other elements is shown in table A.3 for free space environment c_{fs} and real ground (arctic land, $\epsilon_r = 3$ and $\sigma = 0.3 \cdot 10^{-3} \frac{S}{m}$) c_{rg} where elements are mounted at approximately 2 m above ground.
First of all the results for free space environment and real ground are mainly very

Tab. 5.3. Mean value and standard deviation of mutual coupling for equilateral grid, elements oriented to $\phi = 45°$

spacing	max$[c_{fs}]$	min$[c_{fs}]$	$\overline{c_{fs}}$	$\sigma_{\overline{c_{fs}}}$	max$[c_{rg}]$	min$[c_{rg}]$	$\overline{c_{rg}}$	$\sigma_{\overline{c_{rg}}}$
0.6 λ	-35.1 dB	-51.1 dB	-41.7 dB	6.1	-35.4 dB	-51.3 dB	-41.9 dB	6.1
0.65 λ	-37.1 dB	-59.6 dB	-44.9 dB	8.4	-37.5 dB	-59.9 dB	-45.1 dB	7.7
0.7 λ	-39.3 dB	-65.0 dB	-47.4 dB	8.6	-39.9 dB	-61.7 dB	-47.3 dB	7.3
0.75 λ	-41.1 dB	-60.6 dB	-48.2 dB	6.2	-41.7 dB	-60.0 dB	-48.6 dB	5.8

similar and differ partially only by 0.1 dB. Unfortunately the influence of the ground is not consistent, sometimes the ground effects advantageously as the coupling is reduced, but partially also increases the coupling by up to 3.3 dB. However generally one can state the ground influence is mainly rather marginal due to its little permittivity and conductivity of the considered arctic land.
In the results of table A.3 one sees an asymmetry of coupling provoked by not exact,

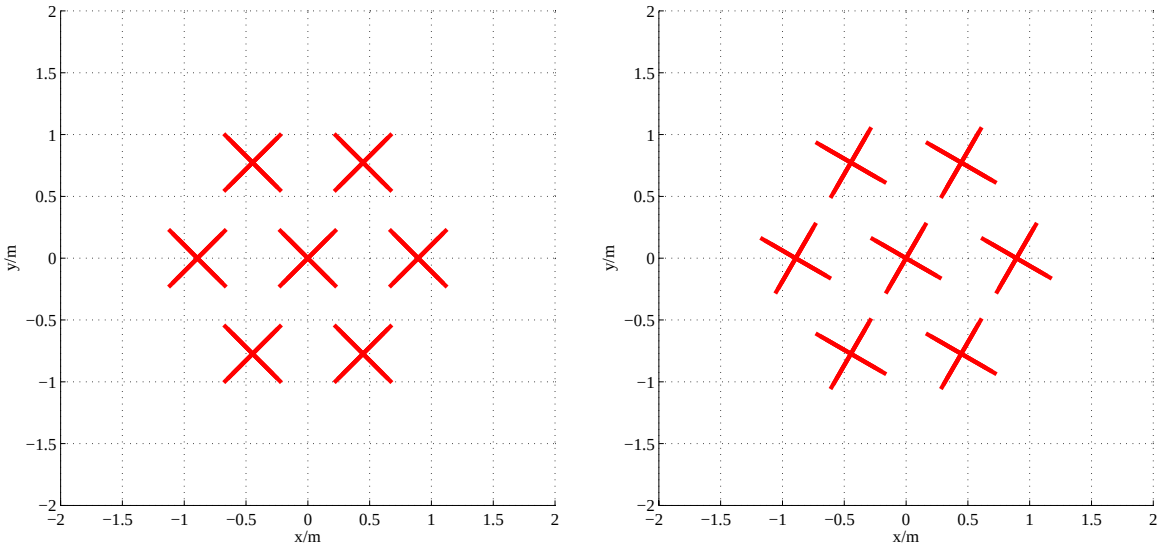

(a) $\phi_e = 45°$ (b) $\phi_e = 60°$

Fig. 5.3. Mutual coupling array, equilateral grid, top view

slightly diverse alignment of the elements to each other. Due to the equilateral grid structure and as the elements are aligned to $\phi = 45°$ the belonging parallel elements have partially different distance to each other, e.g. element 7 to 5 and 7 to 11.
The optimum decoupling for this geometry on an equilateral grid appears for the greatest observed spacing of 0.75 wavelength for both free space and real ground environment. The outstanding low coupling of element 6 and 10 of -65 dB , is deteriorated when spacing is increased above $d = 0.7\lambda$. This is the reason for the decrease of standard deviation of the mutual coupling for the mentioned spacings, which might mislead in this case. Even for a spacing of $d = 0.7\lambda$ the maximum coupling of -39.3 dB is reasonably low and thus competitive to the earlier analyzed structures.

In this model the maximum impedance mutation appeared for spacings of 0.7λ and 0.75λ and reached $Z = (185.4 - j9.1)\,\Omega$. This impedance corresponds to a VSWR $s = 1.10$. The minimum of mutation appeared for a spacing $d = 0.65\lambda$ with an impedance $Z = (198.7 - j6.9)\,\Omega$ and $s = 1.04$ respectively.

5.4 Array elements oriented to $\phi_e = 60°$ on an equilateral grid

Another option for the elements alignment is to rotate the linear elements to $\phi = 60°$ which is shown in figure 5.3(b). Elements 7 and 8 are excited to form a circular wave.

The mutual coupling for free space and real ground to the other elements for spacings of 0.6 to 0.75 wavelengths is shown in table A.4. The elements are mounted approximately 2 m above ground.

The orientation of the elements to $\phi = 60°$ evokes for free space environment partially

Tab. 5.4. Mean value and standard deviation of mutual coupling for equilateral grid, elements oriented to $\phi = 60°$

spacing	$\max[c_{fs}]$	$\min[c_{fs}]$	$\overline{c_{fs}}$	$\sigma_{\overline{c_{fs}}}$	$\max[c_{rg}]$	$\min[c_{rg}]$	$\overline{c_{rg}}$	$\sigma_{\overline{c_{rg}}}$
0.6 λ	-33.9 dB	-57.1 dB	-44.1 dB	9.9	-34.1 dB	-56.9 dB	-44.3 dB	9.9
0.65 λ	-38.1 dB	-60.5 dB	-46.3 dB	9.5	-38.5 dB	-60.3 dB	-46.6 dB	9.3
0.7 λ	-40.3 dB	-64.1 dB	-47.5 dB	10.2	-40.9 dB	-61.1 dB	-48.4 dB	8.0
0.75 λ	-41.6 dB	-63.1 dB	-49.5 dB	7.5	-42.3 dB	-59.7 dB	-49.5 dB	6.4

higher coupling of 1.2 dB and 1.3 dB for an element spacing of 0.6 wavelength in free space and real ground environment respectively than elements to $\phi = 45°$, although the absolute minimum for this spacing is about 6 dB less than in the earlier analyzed structure, where the elements are oriented to $\phi_e = 45°$. Thus also the mean values $\overline{c_{fs}}$ and $\overline{c_{rg}}$ show an overall decreased coupling. Nevertheless the greater coupling of 1.2 dB compared to the $\phi_e = 45°$ orientation denies a usage of this antenna alignment with a spacing of $d = 0.6\lambda$.

For greater spacings this array geometry improves the decoupling of the above presented $\phi_e = 45°$ orientation, for a spacing of $d = 0.7\lambda$ the $\phi = 60°$ aligned array elements gain 1 dB of decoupling, while the minimum coupling is 0.9 dB less than the $\phi = 45°$ aligned elements. Even for a spacing of $d = 0.75\lambda$ the alignment shown in figure 5.3(b) reveals some enhancements as maximum and minimum coupling is mainly improved, however these values are not that significant anymore.

This antenna alignment shows an almost similar influence of the ground like earlier in the structure with $\phi_e = 45°$ orientation with partially up to 3.4 dB on one hand and often only 0.2 dB on the other hand.

The influence of the ground may be considered as smoothing, which one can see in both structures with its elements oriented to $\phi_e = 45°$ and $\phi_e = 60°$ as the standard deviation mostly drops with the appearance of ground.

This structure may be used for spacings of $d = 0.65\lambda$ up to $d = 0.75\lambda$.

For a spacing $d = 0.75\lambda$ the maximum impedance mutation appeared in this model with $Z = (185.2 - j8.1)\,\Omega$ and $s = 1.09$ respectively, while the minimum could be derived a spacing $d = 0.65\lambda$ with an impedance $Z = (197.1 - j8.9)\,\Omega$ and $s = 1.05$ respectively.

5.5 Array elements oriented to $\phi_e = 45°$ on an equilateral grid and tilted to $\theta_t = 23°$

In this section the coupling of the $\phi = 45°$ aligned array elements, like evaluated in section 5.3 is simulated. The array elements are mounted approximately 2 m above real ground (arctic land, $\epsilon_r = 3$ and $\sigma = 0.3 \cdot 10^{-3} \frac{S}{m}$) and mechanically tilted off-zenith to $\theta_t = 23°$ as it has been proposed in the thesis description as a possible array layout and is shown in figure 5.4. Results are presented in table A.5.

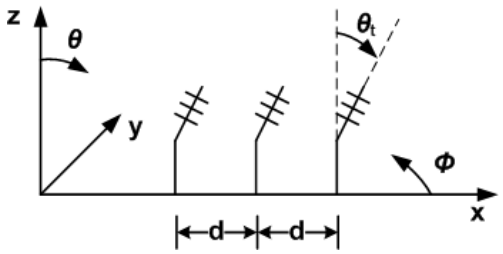

Fig. 5.4. Array elements oriented off-zenith

Tab. 5.5. Mean value and standard deviation of mutual coupling for equilateral grid, $\theta = 23°$ tilted elements, oriented to $\phi = 45°$

spacing	max[c_{fs}]	min[c_{fs}]	$\overline{c_{fs}}$	$\sigma_{\overline{c_{fs}}}$	max[c_{rg}]	min[c_{rg}]	$\overline{c_{rg}}$	$\sigma_{\overline{c_{rg}}}$
0.6 λ	-21.1 dB	-55.2 dB	-39.3 dB	8.9	-20.6 dB	-55.6 dB	-35.9 dB	9.6
0.65 λ	-23.2 dB	-63.2 dB	-43.7 dB	9.9	-22.0 dB	-60.0 dB	-43.2 dB	9.8
0.7 λ	-25.7 dB	-71.7 dB	-47.5 dB	11.1	-23.7 dB	-60.3 dB	-45.6 dB	9.5
0.75 λ	-28.2 dB	-66.6 dB	-48.2 dB	9.0	-25.3 dB	-59.6 dB	-45.8 dB	8.2

In table A.5 one can clearly see the elements in x-direction show higher coupling rates as earlier in the structure of $\phi_e = 45°$ and zenith oriented elements and contrariwise. This behavior is consistent to the rotation of the single array elements off-zenith, pointing to $\theta_t = 23°$, as the elements with higher coupling are partially stronger exposed to the radiation of the elements in the opposite direction.
Compared to the structure with array elements oriented to $\phi_e = 45°$ and pointing to zenith, the now analyzed structure with its maximum of element gain bearing to $\theta = 23°$ shows far higher coupling with a maximum of -21.1 dB at a spacing of 0.6 wavelength for free space and even -20.6 dB for real ground, which is 12.8 dB and 13.5 dB more than it is for zenith aligned array elements. This higher mutual coupling is comprehensible as parts of the array elements get in closer proximity to each other compared to

pointing into zenith.
Even for a rather large spacing like 0.7 or 0.75 wavelength, where the maximum mutual coupling decreases, however it is still considerably high with -28.2 dB or -25.3 dB respectively and again even up to 17 dB worse than in the zenith-aligned structure.
Additionally the influence of the real ground deteriorates the yet poor decoupling of the array elements by up to 3 dB.
Thus these alignment of array elements shouldn't really be used as the assumed benefit of gain at $\theta = 23°$ is in no relation to the deterioration of decoupling. With a maximum coupling of -28.2 dB one has to expect recognizable impedance mutation. Furthermore parts of the radiated energy from one array element might lead to a feedback of power onto another element and thus to a considerable high load on the transmitter chain.

For this model the maximum impedance mutation arose for a spacing $d = 0.7\lambda$ and $d = 0.75\lambda$ with $Z = (187.9 - j21.9)\,\Omega$ and respectively $s = 1.14$. The minimum mutation appeared at a spacing $d = 0.60\lambda$ with an impedance $Z = (200.6 - j14.6)\,\Omega$ and $s = 1.08$ respectively.

5.6 Array elements oriented to $\phi_e = 60°$ on an equilateral grid and tilted to $\theta_t = 23°$

As it turned out in section 5.4 an alignment of the elements to $\phi = 60°$ might be benefiting, thus analogical to the section 5.5 the coupling for array elements is simulated for real ground, but the elements are aligned to $\phi = 60°$ and $\phi = 150°$ instead of $\phi = 45°$ and $\phi = 135°$ respectively, while the antenna is mechanically fixed off-zenith to $\theta_t = 23°$. Table A.6 shows the consequential result.

Tab. 5.6. Mean value and standard deviation of mutual coupling for equilateral grid, $\theta = 23°$ tilted elements, oriented to $\phi = 60°$

spacing	max[c_{fs}]	min[c_{fs}]	$\overline{c_{fs}}$	$\sigma_{\overline{c_{fs}}}$	max[c_{rg}]	min[c_{rg}]	$\overline{c_{rg}}$	$\sigma_{\overline{c_{rg}}}$
0.6 λ	-26.2 dB	-62.3 dB	-40.7 dB	10.7	-25.0 dB	-61.3 dB	-37.0 dB	11.2
0.65 λ	-27.0 dB	-70.6 dB	-45.3 dB	11.5	-25.8 dB	-62.2 dB	-44.0 dB	10.2
0.7 λ	-28.3 dB	-69.8 dB	-47.8 dB	10.6	-26.2 dB	-59.1 dB	-46.0 dB	9.2
0.75 λ	-29.6 dB	-66.0 dB	-48.5 dB	9.0	-26.7 dB	-56.3 dB	-46.0 dB	7.7

The largest mean value of the mutual coupling appears for a spacing of $d = 0.75\lambda$ for free space, where also the most equal coupling to all elements is emerged due to

deterioration of the elements with the lowest coupling.
One can see the alignment of the array elements to $\phi = 60°$ decreased the coupling by up to 5 dB, but is with up to 29.6 dB for free space environment and even -26.7 dB for arctic land still seriously higher than in the structures with zenith-aligned array elements. Thus this array structure shouldn't be used as it can be assumed the actually about 10 dB greater coupling likely provokes impedance mutation and acts as power feedback on the transmitter chains of the other array elements.

In the herein analyzed model structure the maximum impedance mutation appeared for a spacing $d = 0.65\lambda$ with $Z = (192.8 - j25.9)\,\Omega$ and $s = 1.15$ respectively. The minimum could be derived for only one linear part of the excited element at a spacing $d = 0.60\lambda$ with an impedance $Z = (206.3 - j0.3)\,\Omega$ and $s = 1.03$ respectively, while the other linear part is again mutated to $Z = (201.2 - j28.9)\,\Omega$ and one thus gets $s = 1.15$. This high differences in the impedance of both linear parts of the excited element point at a high coupling rate.

5.7 Conclusion

The first model, presented in section 5.1, shows fair coupling rates of -35.7 dB in the maximum and down to -69.6 dB as the absolute minimum. As maximum of coupling is saturating when spacing reaches $d = 0.7\lambda$, but minimum still decreases, one may choose this array structure for all observed spacings, but optimum would be 0.7λ. The choice of spacing rather more depends on other demands like e.g. beam forming to greater off-zenith angles, avoidance of grating lobes, as the mutual coupling doesn't show really precarious levels. The only drawback appears as a high coupling difference between the linear parts of one crossed array element with up to -22 dB, which refers almost the absolute maximum and minimum of coupling on this single crossed element. On the other hand for the greatest observed spacing of $d = 0.75\lambda$ partially higher mutual coupling is initiated on some array elements, but as the influence is rather low, even the spacing of $d = 0.75\lambda$ may be used.
In the second model with array elements oriented to $\phi = 45°$, section 5.2, the severe coupling differences on the linear parts of one crossed array element are limited to 14 dB. The maximum coupling on this alignment of array elements is rather high for lower spacings as $d = 0.6\lambda$, but competitive and even profitable for greater spacings as $d = 0.7\lambda$ to $d = 0.75\lambda$ as the coupling rates of the first structure are achieved and even improved. Furthermore as stated earlier this structure shows mainly a very equal coupling of all array elements.
This array structure with its orientation of elements should be preferred for spacings

of $d = 0.7\lambda$ to $d = 0.75\lambda$, while still has to be cared about the influence of real ground. If a squared grid structure is demanded, the second structure with $\phi = 45°$ oriented elements, should be used as the spacing may be increased up to $d = 0.75\lambda$. However severe grating lobes appear above $d = 0.6\lambda$ which limits the possible beam steering angle.

As a triangular and in particular equilateral grid structure seems to be profitable in terms of grating lobes, this structure has been examined in greater detail. In the coupling model in section 5.3 an array organized on an equilateral grid has been evaluated. In terms of mutual coupling the equilateral grid structure appeared to be at least competitive or even better than a squared grid evaluated in section 5.2. However the minimum coupling doesn't reach the absolute minimum of the second squared grid arranged structure, but the lower standard deviation of mutual coupling exhibits an even more equal coupling of all array elements.

In the structure presented in section 5.4 with its elements aligned to $\phi = 60°$ the yet advantageous coupling rates of the $\phi = 45°$ oriented elements structure could be improved for spacings besides $d = 0.6\lambda$. The maximum coupling is decreased by 1 dB or 0.5 dB for spacings of $d = 0.65\lambda$ and $d = 0.7\lambda$ or $d = 0.75\lambda$ respectively. Additionally the influence of the real ground is benefiting, like it also has been in the earlier structure with its $\phi = 45°$ aligned element. The only drawback is a slightly less equal coupling of the array elements compared to the $\phi = 45°$ elements ($\sigma_{\overline{c_{rg}}} = 8.0$ to $\sigma_{\overline{c_{rg}}} = 7.3$ for $\phi = 60°$ to $\phi = 45°$ oriented elements respectively). However altogether arranging the elements to $\phi = 60°$ and orthogonally appears to be advantageous.

The coupling model structures with mechanically $\theta = 23°$ off-zenith tilted array elements show severely high coupling rates with always over -30 dB for all evaluated spacings. Thus even at most promising spacings the mutual coupling is approximately 10 dB greater than in any other array structure, which thus seems to be generally insufficient. Additionally the influence of the real ground increases the mutual coupling and this is exactly the opposite behavior than in the zenith-aligned array element structures. However the structure (section 5.6) with its array elements aligned to $\phi = 60°$ shows an improvement to the $\phi = 45°$ oriented elements described in section 5.5.

One has to weight the high mutual coupling with the advantage of higher gain at the desired main direction of $\theta = 23°$. However this gain advantage probably won't reach significantly more than 1 dB, which has to be evaluated in the further progress of this thesis work. Furthermore when the array elements are mechanically fixed to $\theta = 23°$ one has to consider the resulting different gain for the same magnitude of off-zenith beam steering in opposite azimuthal directions, e.g. $\phi = 0°$ to $\phi = 180°$.

Altogether from the point of view achieving as few coupling as possible to ensure the lowest element-interaction one is advised to choose one of the structures with its array elements pointing to zenith (sections 5.3 and 5.4).

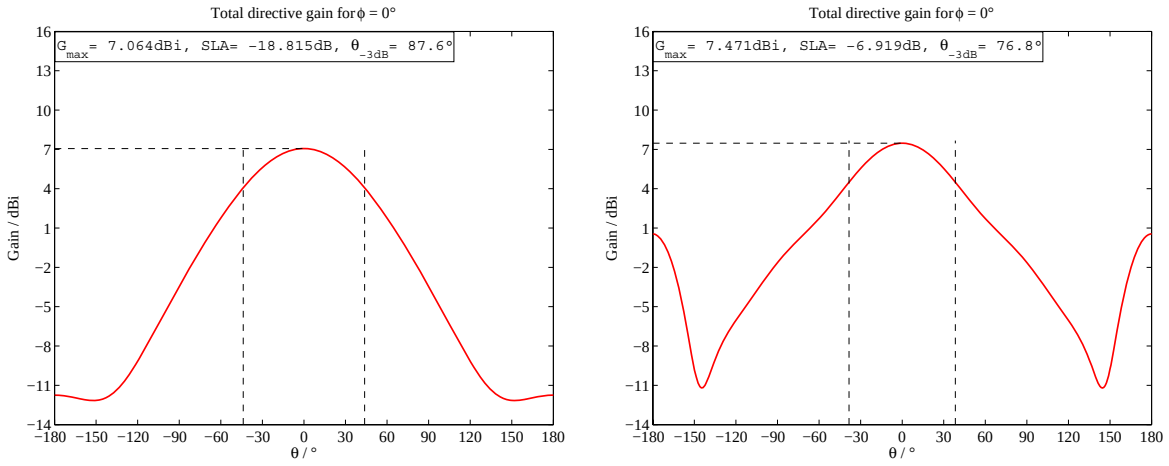

(a) Single element (b) Single element including mutual coupling

Fig. 5.5. Radiation pattern comparison due mutual coupling

As completion figures 5.5(a) and 5.5(b) show the radiation pattern for $\phi = 0°$ in free space as a comparison of the single yagi antenna and the array with its zenith pointing array elements presented in section 5.3 with a spacing of 0.7 wavelength. One can see the mutation of radiation pattern, where the gain is raised by 0.4 dB, while the beamwidth θ_{-3dB} is lowered by almost 11° and the shown sidelobe attenuation, actually a back lobe, is severely deteriorated by 11 dB.
Such results appear just due to the presence of additional resonant antennas in closer proximity, which are terminated and not fed with any power by the transmitter, as the mutual coupling is still recognizable and the terminated antennas reradiate their electromagnetic field in magnitude and phase, depending on their position relative to the transmitter fed center antenna, and the mutual coupling. The massive increase of back lobe compared to main lobe refers to the group characteristic that is yet introduced. If the currently terminated array elements are fed with equal phase and magnitude respectively to the center element, the back lobe reaches 1.6 dBi, which is close to the 0.5 dBi back lobe as shown in figure 5.5(b), where the outer elements are terminated. Furthermore in the practical application of the planned radar the antennas will be oriented more or less with the back lobe to the ground, where the emitted fields will only be partially reflected as the arctic ground shows poor electromagnetic characteristics. Actually even for a snow covered ground, where the relative permittivity and conductivity are lower than in the arctic ground model, the influence of the ground to the antenna itself is even less, whereas the arctic ground model yet proved to have mainly rather low effect as shown earlier.

Regarding the derived impedance mutations of the excited element, one may state the greatest influence seems to appear within the first structure (squared grid, elements

oriented to $\phi = 0°$) for spacing $d = 0.6\lambda$ and for both structures with tilted elements rather independent of the spacing. The generally lowest mutation of impedance for the excited element appeared in the both structures, where the array elements are placed on an equilateral grid, pointing to zenith. Although it has to be noticed the imaginary part of the impedance have been permanently negative. Thus the resonance frequency of the excited element seems to be continuously shifted in all models to a higher frequency.
In Figure 5.6 the impedance (red and blue for real and imaginary part, magenta for magnitude) and the phase distribution (black) is shown.
Obviously the resonance frequency of the antenna could be modified by changing the

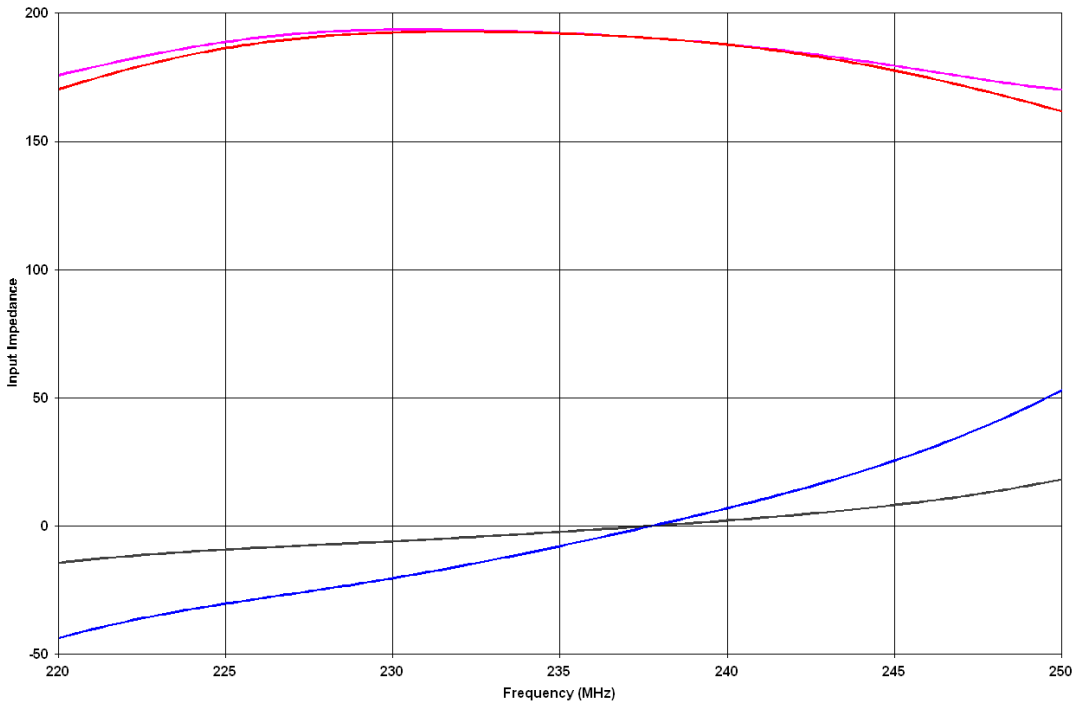

Fig. 5.6. Impedance and phase distribution of array elements oriented to $\phi_e = 45°$ on an equilateral grid

dimensions of the elements. Due to this results the designed antenna should be tested in reality with a similar setup to investigate the validity of the herein presented NEC deliverables.

Chapter 6

Array studies

In the following sections various array structures are observed and their characteristics are compared.
Every herein after presented model is basing on the chosen 3-element crossed yagi antenna evaluated in section 4.1.2 as a single array element.

Again circular polarization shall be induced, like it has been considered in the section 4 and is included in the following models.
A direct simulation of the overall characteristic of the whole array, consisting of about 10000 array elements, by the aid of NEC appeared to be very time and resource consuming and thus been impossible within meaningful limits of current computer architecture and resources. The calculation of the whole array with adequate accuracy would need for example at least 300 GB main memory (RAM) and an extraordinary computing time as long as no highly parallel multi processor code is available.
Thus the characteristics of smaller arrays have been evaluated in the first steps while concentrating on the effects of mutual coupling, grid structure, spacing and the therefore induced sidelobes and grating lobes.
All evaluated arrays are called broadside arrays as the main radiation is evoked directed normal to the plane of the array. This definition shall not limit the direction of the main beam, rather more announce the main beam is directed to the zenith and thus normal to the ideal earth surface, when all elements are equally fed in phase.

The presented radiation pattern are, if not otherwise marked, generated with an angular resolution of $\Delta_\theta = 0.1°$ and $\Delta_\theta = \Delta_\phi = 1.5°$ for the side and top view respectively. As the top view pattern are generated for 1.5° resolution in azimuth and zenith angle the total data amount of each top view pattern reaches 14701 sets of directivity data.

6.1 Array of 100 line elements

This section presents the evaluation of an array, which consists of 100 elements aligned in one row as it is depicted in figure 6.1(a). The number of elements arose from the projected total number of array elements for a rectangular aperture and thus leading to the root of the total elements amount.
The array elements are placed in this model aligned to zenith with the lowest reflector 2 m above real ground (arctic land, $\epsilon_r = 3$ and $\sigma = 0.3 \cdot 10^{-3} \frac{S}{m}$) with a spacing of approximately $d = 0.7\lambda$.
Figure 6.1(b) represents the radiation pattern of the mentioned line array out of 100

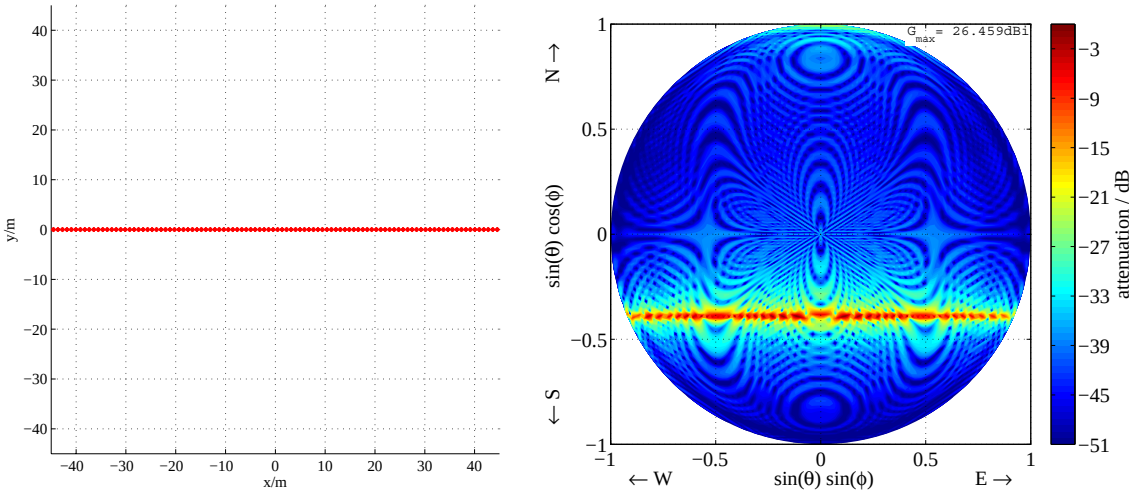

(a) Geometry (b) Radiation pattern, top view

Fig. 6.1. Model of a 100 elements line array

elements in top view. One clearly sees a high constriction of radiation in a cross section around $\phi = 0°$ while for a cross section parallel to $\phi = 90°$ the original pattern of the single element is almost untouched.
Figure 6.2 depicts the radiation pattern for a $\phi = 0°$ cross section for the observed model from zenith angle $\theta = -90°$ up to $\theta = 90°$.
Most important results have been the validation of the envisaged gain, beamwidth θ_3, sidelobe attenuation and the off-zenith beam forming to $\theta_0 = -23°$ as it's been claimed in the thesis tasks.
One can see from the cross section through $\phi = 0°$ the general distribution of radiation. The beamwidth including beam broadening due to beam forming off-broadside has been introduced in section 2.3. The beamwidth θ_3 with and without broadening may be calculated by equations 2.44 and 2.21 respectively. Thus the theoretical maximum

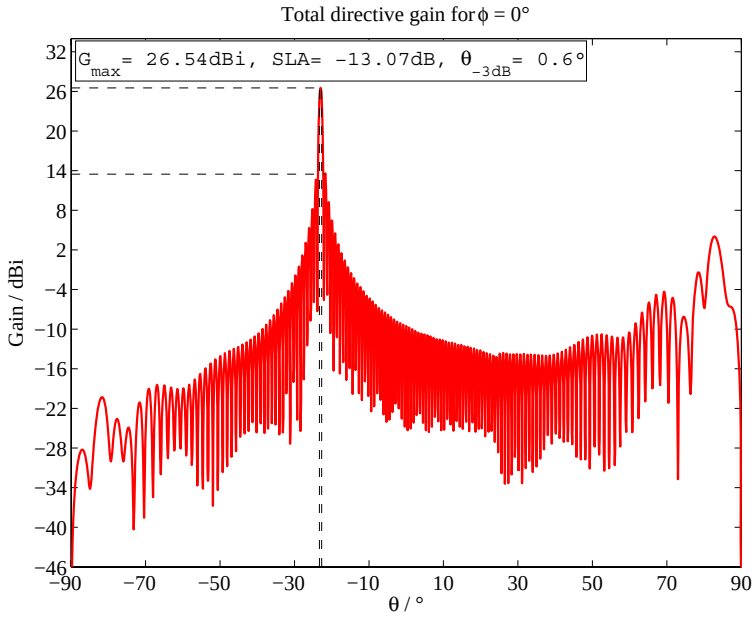

Fig. 6.2. Radiation pattern - line source of 100 3-element crossed yagi

beamwidths is calculated to

$$\theta_{3b} = [\arcsin(0.3970104) - \arcsin(0.3844519)] \approx 0.78^\circ \tag{6.1}$$

including and

$$\theta_3 = \arcsin(0.01238132) \approx 0.71^\circ \tag{6.2}$$

excluding broadening respectively.

The difference to the shown beamwidth in figure 6.2 is provoked by an angular resolution $\Delta_\theta = 0.1^\circ$ of the zenith angle for cross sections of ϕ in this simulation model, which has generally been used as with the angular resolution the needed calculation time increases significantly. Furthermore in the evaluation of the raw data using MATLAB the beamwidth has not been interpolated and thus gives the best possible, obviously optimistic, beamwidth.

For a more detailed resolution in the NEC raw output data a simulation limited to the angular spectrum of $\theta = -33^\circ$ to $\theta = -13^\circ$ resulted in a beamwidth of $\theta_3 = 0.76^\circ$, which is presented in figure 6.3(a) where an angular resolution of $\Delta_\theta = 0.02^\circ$ has been used. Thus the calculated maximum beamwidth from equation 2.44 shows a good match and high reliability.

Furthermore figure 6.3(b) shows a radiation plot for $\theta = -10^\circ$ to $\theta = 10^\circ$ where the main beam is evoked in broadsight. The resulting beamwidth $\theta_3 = 0.68^\circ$ matches quite well with the in equation 6.2 calculated beamwidth, hence one has to remember it gives the maximum beamwidth. The real beamwidth might be slightly lower as only the aperture is included, not the influence by the single elements characteristic. For

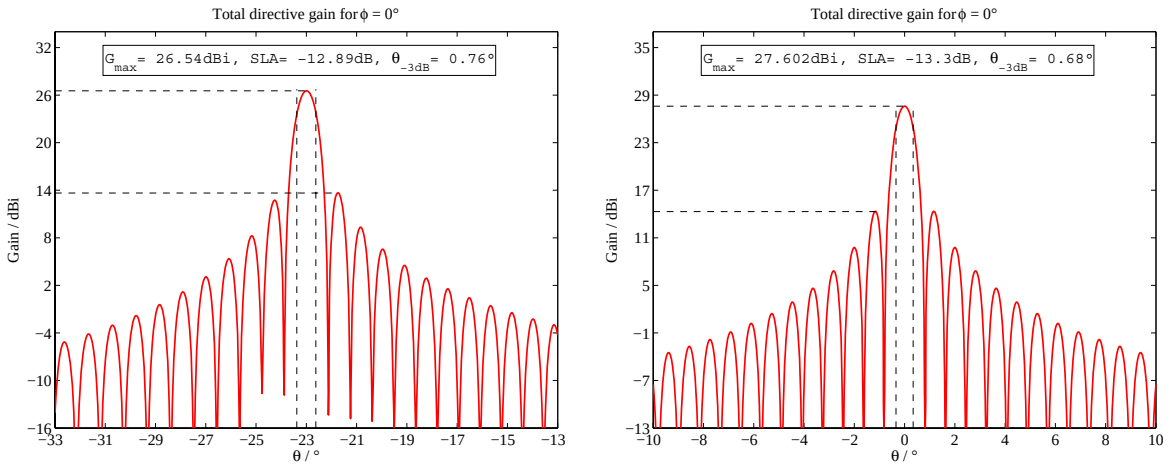

(a) $\phi = 0°$, $\theta_0 = -23°$ (b) $\phi = 0°$, $\theta_0 = 0°$

Fig. 6.3. Radiation pattern zoom for a line of 100 array elements

beaming broadside (figure 6.3(b)) a minimum sidelobe attenuation of -13.3 dB is achieved, which approximately equals the possible sidelobe attenuation like given in table 2.1 of section 2.2 for a line source array.
Furthermore figures 6.3(a) and 6.3(b) outline the main lobe gain loss of roughly 1 dB due to off-broadside beaming.
Additionally the partially introduction of grating lobes is illustrated as described in 2.4. With equation 2.47 one obtains the maximum spacing d for a grating-lobe-free beam forming at the chosen off-zenith angle to $d = 0.719\lambda$. Although the used spacing of this model is still below the equation limit, grating lobe induced sidelobes are introduced. Thus one has to be careful with grating lobe limit calculated by equation 2.47 as its sidelobes may already be in visible space and therefore evoke deterioration of the radiation pattern.
The simulated maximum gain of 27.6 dBi for this 100 element line source may be verified by estimating the overall gain considering the gain of the single element and the additive logarithmic gain due to additional 99 antennas

$$g_a = 10\log_{10}\left(\frac{N_a}{N_r}\right) \tag{6.3}$$

where g_a is the additive gain of the observed array with N_a the total amount of array elements compared to the number of reference elements N_r, actually the single element, for an almost optimum spacing.
Taking now the in section 4.1.2 quoted gain of the single element and about 20 dB additive array gain due to equation 6.3 one obtains a gain of 27.1 dBi.
Furthermore one may approximate the overall gain for the envisaged 10000 array elements of roughly 47 dBi gain for an optimum spacing.

6.2 Planar array of 400 elements

In this section the evaluation of both the rectangular, actually squared, and equilateral grid structure is presented which has been performed in simulations for this size of array in closer detail.

Two different array structures out of identically 400 elements, with 20 elements each row, and a general spacing of $d = 0.7\lambda$ are shown in figure 6.4.
In figure 6.4(a) the 400 array elements are aligned on a squared grid structure

$$d_x = d_y = d = 0.7\lambda \tag{6.4}$$

and thus aperture length is equal in x- and y-plane.
Contrary in figure 6.4(b) the 400 elements are aligned on an equilateral grid and thus height and width of the aperture differ. One recognizes every second row (in y-plane) is displaced by the half of the spacing ($\Delta_{d_x} = 0.35\lambda$) on the x-axis and the spacing between rows along the y-axis is reduced to

$$d_y = \frac{\sqrt{3}}{2} \cdot d_x \approx 0.606\lambda \tag{6.5}$$

which refers to the height of an equilateral triangle.

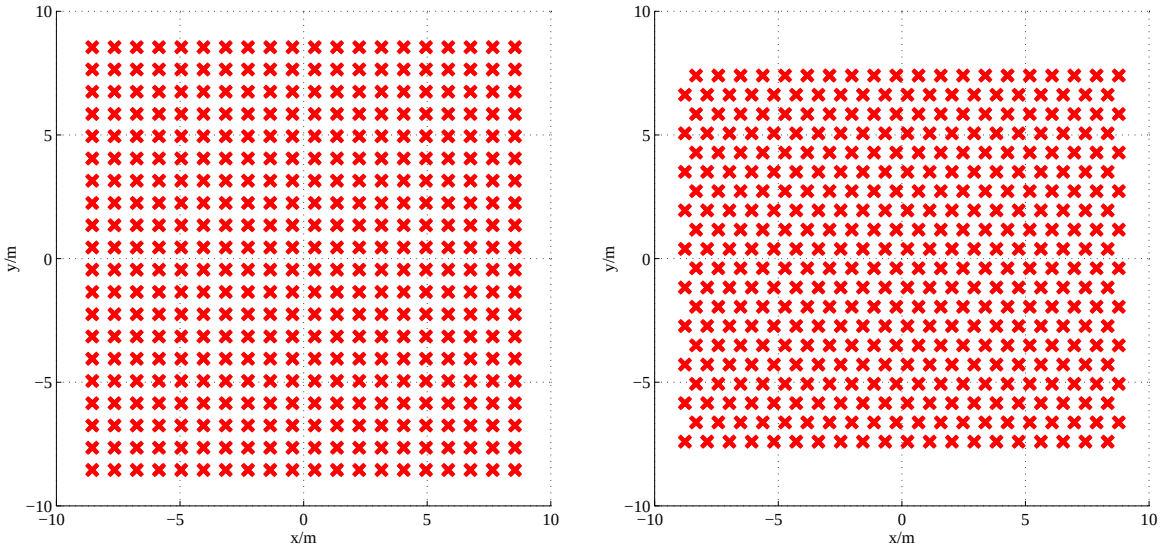

(a) Geometry, squared grid

(b) Geometry, equilateral grid

Fig. 6.4. Model of 400 element arrays

The differences in the aperture of the array structure determine variant radiation pattern. As the aperture of model with equilateral grid structure (figure 6.4(b)) is significantly smaller than for the squared grid structure (figure 6.4(a)), consequently the gain

is decreased by the amount of aperture decline respectively equation 6.5 and leads to

$$\Delta_g = 10\log_{10}\left(\frac{\sqrt{3}}{2}\right) \approx -0.625dB \tag{6.6}$$

where Δ_g describes the resulting gain loss.
Other consequences of the different aperture are variant radiation pattern along the x- and y-axis (cross sections of $\phi = 0°$ and $\phi = 90°$) and their belonging beamwidth respectively as it's shown in figure 6.6.
Analogical to the calculation in equation 6.2, the beamwidth for both planes can be estimated by equation 2.21 and 6.5 to

$$\begin{aligned} \theta_{3_x} &= \arcsin\left(0.06279\right) \approx 3.60° \\ \theta_{3_y} &= \arcsin\left(0.06279 \cdot \frac{2}{\sqrt{3}}\right) \approx 4.16° \end{aligned} \tag{6.7}$$

respectively.
In figure 6.5(b) one may see an imbalance of radiation, as the right part of the figure

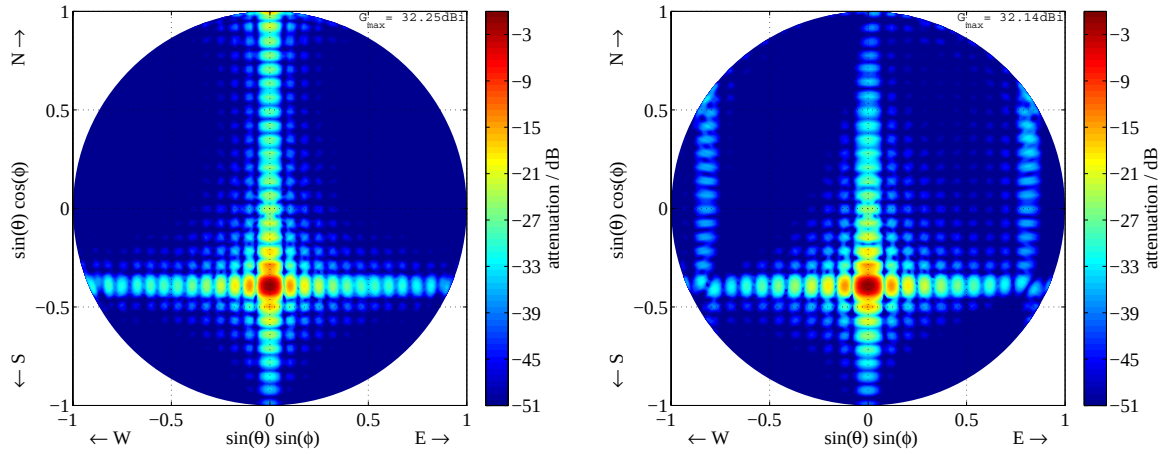

(a) Squared grid (b) Equilateral grid

Fig. 6.5. Model of 400 element arrays, radiation pattern top view

shows a slightly higher sidelobe-level than the left. This discrepancy in both halves is evoked by the imbalance of array elements in the aperture of x-plane (figure 6.4(b) correspondingly) due to the pure movement of every second row by the half of the spacing and perpetuation of the amount of row elements to achieve an equilateral grid structure. A simple solution to this imbalance is the decrease of elements in the causing rows, thus every second row by one. The result is shown in the following sections as the cause has been considered afterwards.
Furthermore one recognizes in figure 6.5(b) additional contingents of radiation provoked aside the main sidelobes aligned to $\phi = 0°$ direction, that are not present in the

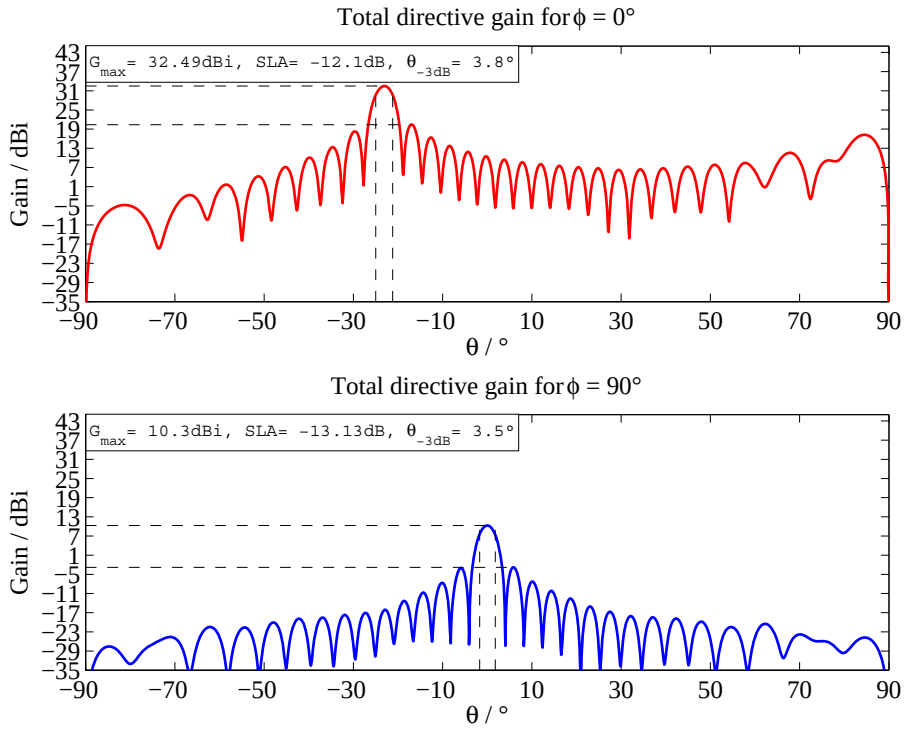

(a) Squared grid

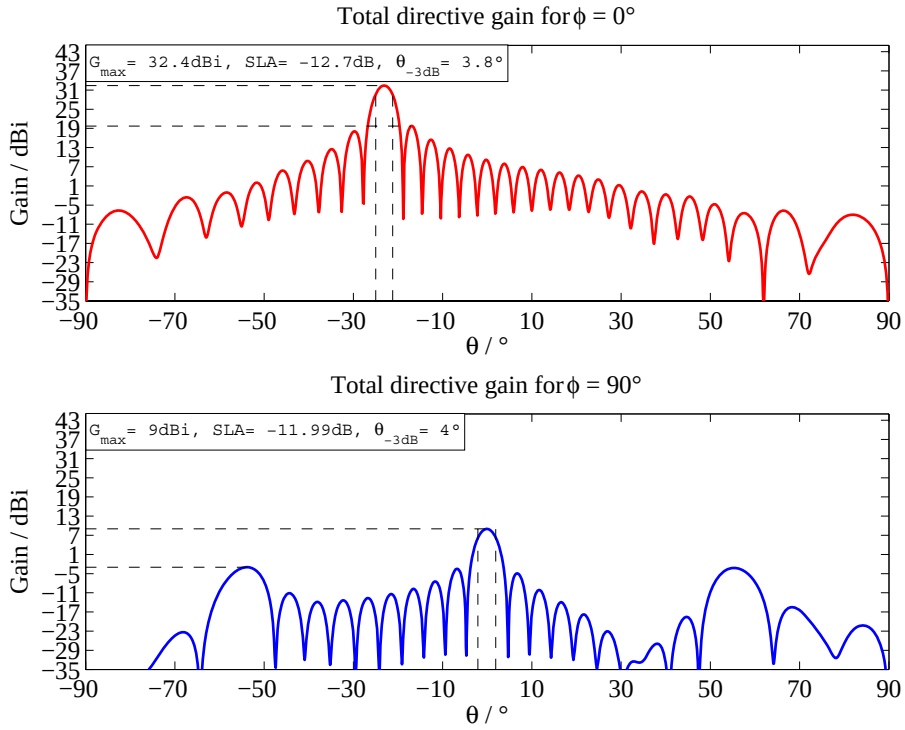

(b) Equilateral grid

Fig. 6.6. Model of 400 element arrays, radiation pattern side view

squared grid structure (figure 6.5(a)) and which refer to sidelobes of the next grating lobes. The context has been introduced in section 6.1 and even presented in figure 2.4(b). However this intrusion of sidelobes is obviously disadvantageous but is still attenuated by roughly 35 dB. Additionally a solution to avoid the amount of intruding sidelobes in that kind is presented afterwards in this thesis work.
At the end of this array evaluation it has to be quoted as follows. To prevent any drop of gain or variant radiation pattern in x- and y- plane one is forced to implement additional array elements to re-establish a symmetric aperture. Otherwise variant radiation pattern with dependency of azimuth angle ϕ will be evoked.

6.3 Planar array of approximately 440 elements

In this section two arrays, both basing on a equilateral grid structure are evaluated in which the earlier claimed improvements are involved.

The first array model consists of 449 elements (3-element crossed yagi, section 4.1.2) with an almost squared aperture like it is shown in figure 6.7(a). For a comparison in figure 6.7(b) is an almost circular aperture array with 433 elements depicted, where the geometry bases on a study of the design phase of IAPs successor of their MST-radar ALWIN.
Both apertures have an almost equal area of about 300 m^2, thus their characteristics

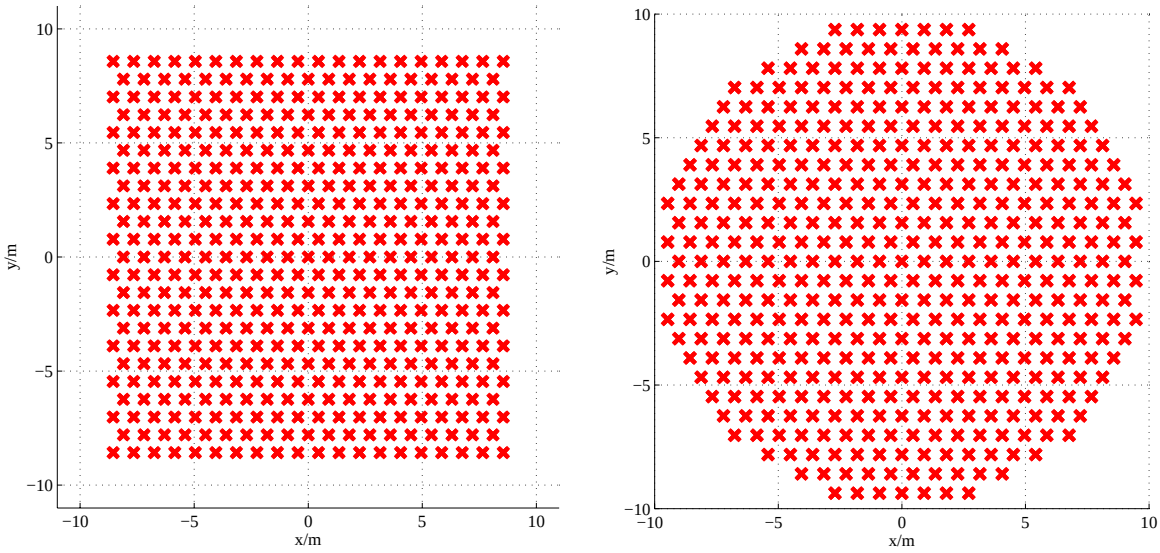

(a) Squared aperture (b) Circular aperture

Fig. 6.7. Geometry of array models with approximately 440 elements

and radiation pattern of both models may directly be compared. One may consider a difference of 0.16 dB due to the amount of array elements.
In figure 6.8 the top view radiation pattern of both aperture models are shown.
One clearly sees the different placement of sidelobes, while in figure 6.8(a) the typical

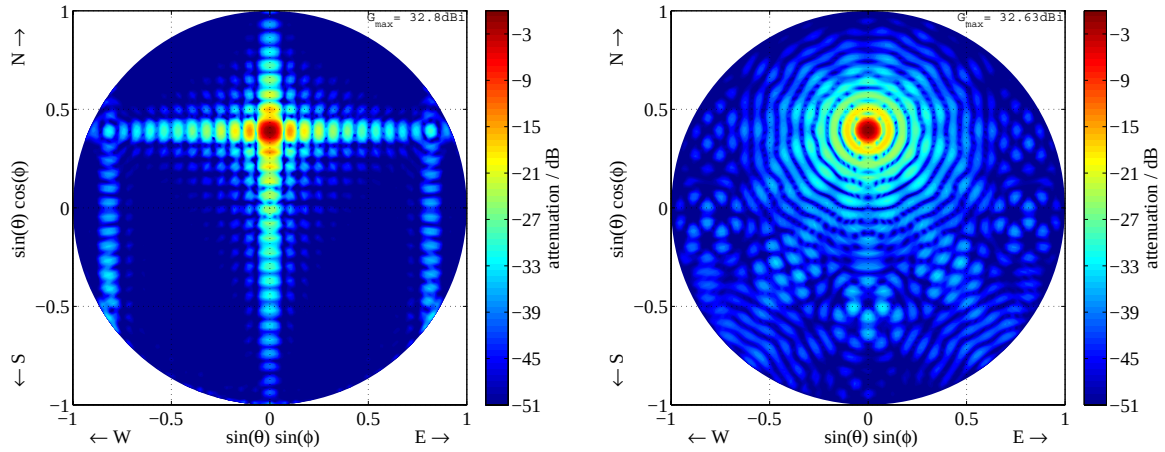

(a) Squared aperture (b) Circular aperture

Fig. 6.8. Radiation pattern in top view of arrays with approximately 440 elements

crossed sidelobe lines are visible, evoked by the squared aperture and the sidelobes from the grating lobes (described and evaluated in section 2.2 and 6.2 respectively), but in figure 6.8(b) due to the circular aperture therefore circular sidelobes in the proximity of the main lobe are generated.
Furthermore one sees the more equal distribution of sidelobe attenuation far off the main beam for a circular aperture compared to the rather steep increase of sidelobe attenuation for a squared aperture. Thus the far offside main beam sidelobe attenuation outside the cross section $\phi = 0°$ and orthogonal may be worse than for a squared aperture, but still at least 30 dB below the main beam.
But according to section 2.2 using a circular aperture one gains an at least 4.5 dB better attenuation on the first sidelobe which is most important. This can be seen and compared in figure 6.9.
Furthermore one may take out of figure 6.9 that azimuthal dependency of lower order sidelobes is far greater for a squared aperture than for the circular aperture. The attenuation on the first sidelobe vary by 1.9 dB and 0.33 dB for a squared (figure 6.9(a)) and circular (figure 6.9(b)) aperture respectively. Both structures have in common that the lowest sidelobe attenuation appears in the direction to zenith and thus to boresight, where the main beam is evoked when antennas are fed with equal phase.

As appendix an additional model is shown in figure 6.10. The analyzed array (figure 6.10(a)) consists of 475 elements arranged on an equilateral grid with approximately

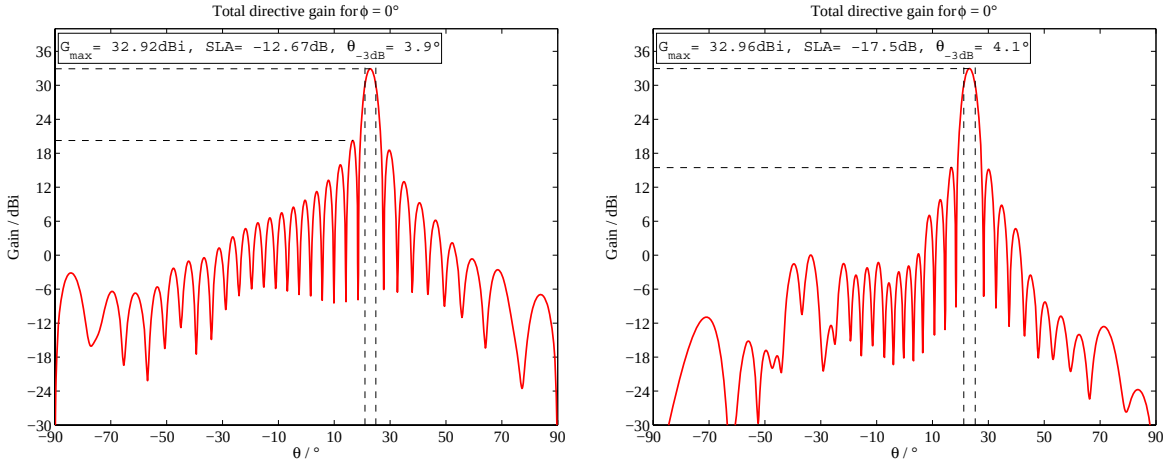

(a) Squared aperture (b) Circular aperture

Fig. 6.9. Radiation pattern in side view of arrays with approximately 440 elements

spacing of $d = 0.7\lambda$ and equals the Japanese MU-radar.

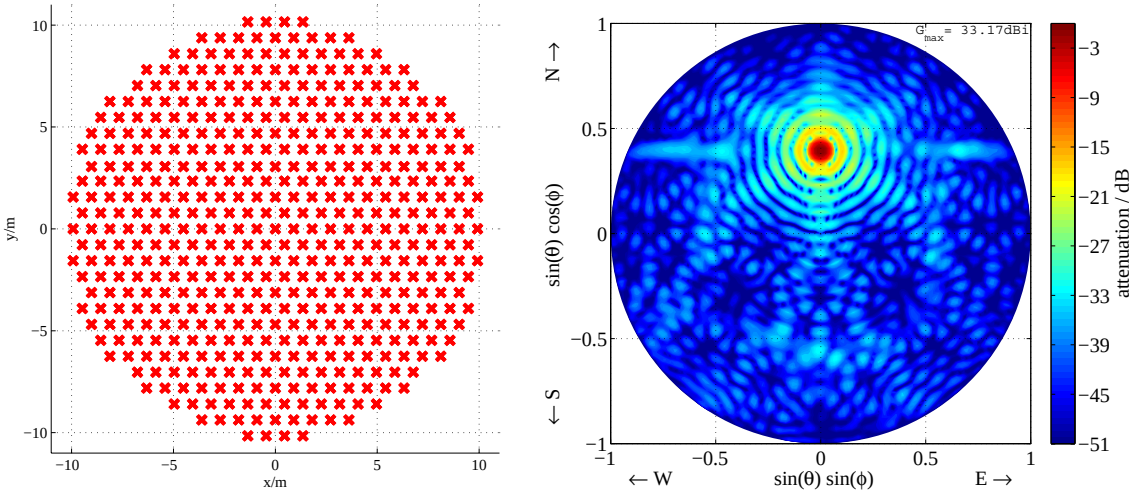

(a) Array geometry (b) Radiation pattern, top view

Fig. 6.10. Model of an array with 475 elements

The radiation pattern in top view (figure 6.10(b)) represents the typical circular evoked main beam and sidelobes due to the almost circular aperture. Rather interesting seems to be the appearance of variations in the sidelobes intensity with the azimuthal angle relative to the main beam leading to a form of a star in the radiation pattern. This variations of sidelobe attenuation are the result of actual aberration of form of the initially wanted circular aperture. The six regular angular ranges with slightly higher sidelobe attenuation, separated by the visible star, may directly be connected to six

spots at the edge of the geometry with higher density of antennas.
Obviously these variations occur about 30 dB below the main beam and thus don't have any significant influence to the pattern in terms of degradation. However it shall be underlined that every even minor deviation from the ideal geometry results in generally low but nevertheless recognizable deterioration of the radiation pattern.
As the main beam is evoked into zenith by a circular aperture array the cross sections

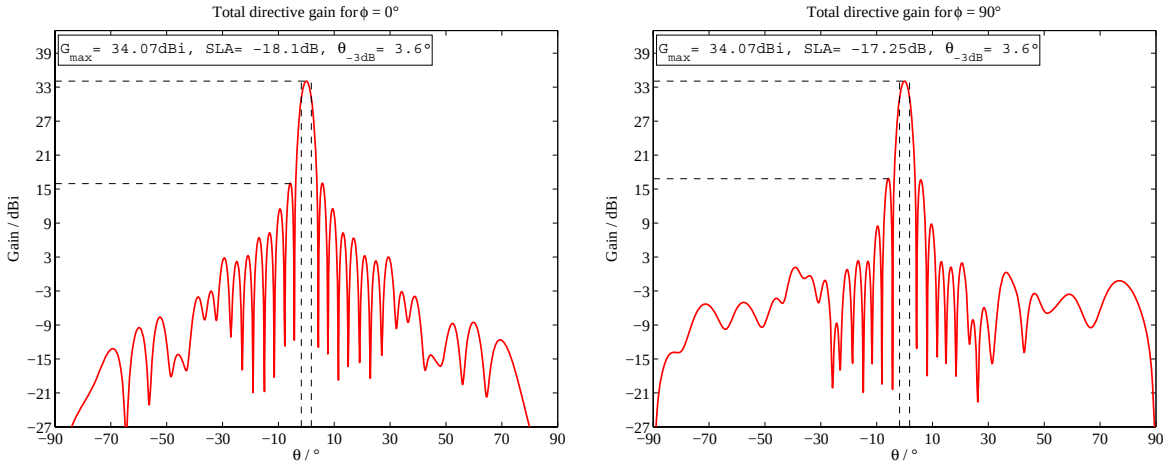

(a) $\phi = 0°$ (b) $\phi = 90°$

Fig. 6.11. Radiation pattern in side view for an array model with 475 elements

for $\phi = 0°$ and $\phi = 90°$ should therefore be equal.
Figure 6.11 presents radiation pattern in side view for the cross sections $\phi = 0°$ and $\phi = 90°$ where variations have yet been visible in the top view. In the radiation pattern for the cross section $\phi = 0°$ one sees a 0.85 dB higher attenuation on the first sidelobe compared to $\phi = 90°$. An even greater influence on the pattern is evoked for sidelobes greater order where both cross sections differ by more than 10 dB.

6.3.1 Weather effects on a planar array of approximately 440 elements

This section evaluates the influence of weather effects on the radiation pattern for an array of 449 elements as shown in figure 6.7(a).

For the simulations of the radiation pattern of this array the same parameters has been used in section 4.6, where the effects on the single array element have been discussed. Therefore analogically a 3 mm thick sheet of sweet-water ice (relative permittivity $\epsilon_r = 5$, conductance $G = 0.0004\,\frac{S}{m}$) have been simulated on every element of array.

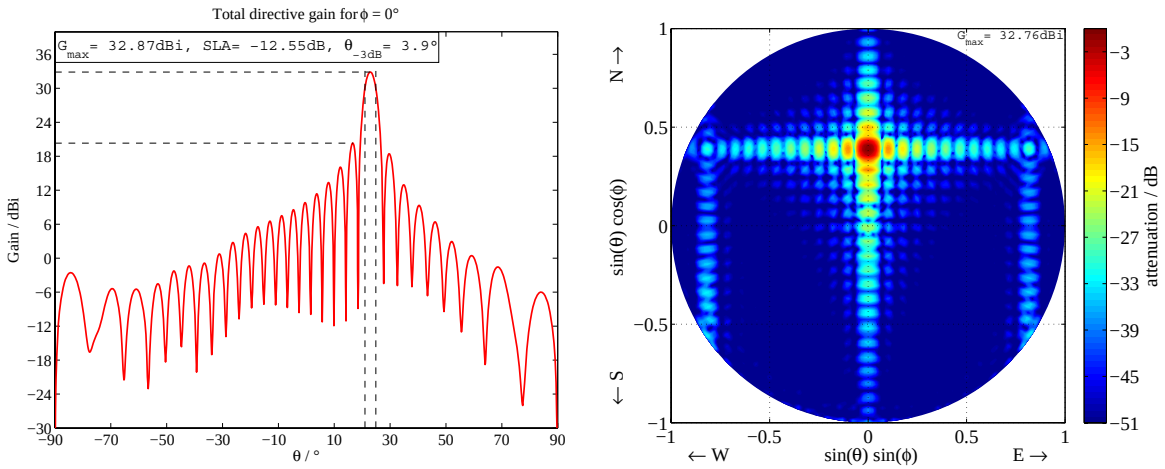

(a) Side view for $\phi = 0°$ (b) Top view

Fig. 6.12. Radiation pattern for an array model with 449 elements including ice coverage

Figure 6.12(a) shows the radiation pattern in side view for the 449 element array including a cover of sweet-water ice on each element. The shown pattern can directly be compared to figure 6.9(a) where the pattern is shown for the same array without ice coverage.
Analog in figure 6.12(b) is shown the radiation pattern in top view, which can be compared to figure 6.8(a).
It can be seen that the radiation pattern differ only very few in gain and minimum attenuation of the sidelobes. This result confirms the conclusion of section 4.6, where for the single array element only few changes in the impedance could be seen.
Thus the weather influences in terms of ice coverage on the array elements within the mentioned thickness provoke only minor changes in the impedance and radiation pattern of the array.

6.4 Thinned planar array of approximately 570 elements

In this section the term of thinned arrays seized on as the theory seems to be advantageously, especially if a squared array aperture is existing and one wants to improve the sidelobe attenuation within limited effort.
The basic for the afterwards evaluated array has been introduced in section 6.3 and depicted in figure 6.7(a).
The motivation for the further considerations have been the improvement of sidelobe

attenuation and half-power beamwidth θ_3 while keeping the necessary efforts to establish such array as low as possible.
As pointed out in section 2.5 a thinned array depending on the degradation of the amount of array elements would provide almost the beamwidth and radiation pattern of a complete array of same aperture. The main degradation for such a structure arises in gain loss. Figure 6.13 shows the geometry and the resulting radiation pattern in

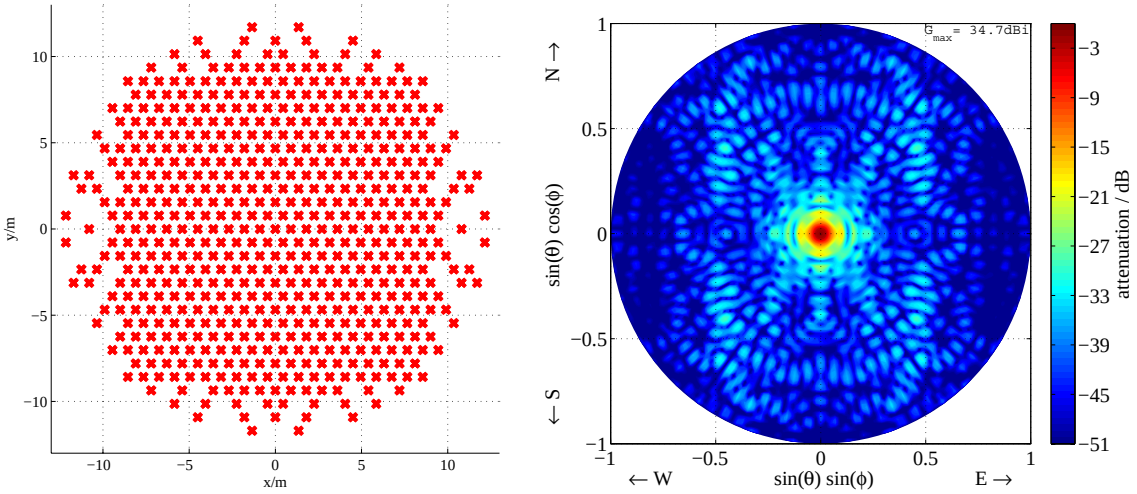

(a) Array geometry (b) Radiation pattern, top view

Fig. 6.13. Thinned array of approximately 570 elements

top view, figure A.6 in side view for the typical cross sections, under the condition of feeding the array element with equal phase and amplitude.
One can see the gain of 34,7 dBi and a $\theta_3 = 3.2°$ beamwidth. Compared with the complete squared aperture array (6.7(a)) the thinned array gains about

$$g = 10\log_{10}\left(\frac{570}{449}\right) \approx 1\,dB \tag{6.8}$$

directivity and the beamwidth is decreased by 0.4° (13%) by adding 121 elements to form an almost circular aperture.
Figure 6.14 shows a comparison of radiation pattern for the chosen thinned array with formed main beams at $\theta = 0°$ and $\theta = 23°$ respectively. Furthermore one can see the achieved attenuation on the first sidelobe with almost -16.7 dB which has therefore been improved by 3.5 dB (the squared 449 element array 6.7(a) evoked almost -13.2 dB), while a completely filled circular aperture array would provide an only 1 dB better attenuation, but with a significantly higher effort in the terms of array elements.
For the same completely filled aperture ($\approx 500\,m^2$) the array would consist of approximately 720 elements. To the original 449 elements of the squared aperture are in the thinned array only 120 elements added to form the circular aperture which is just

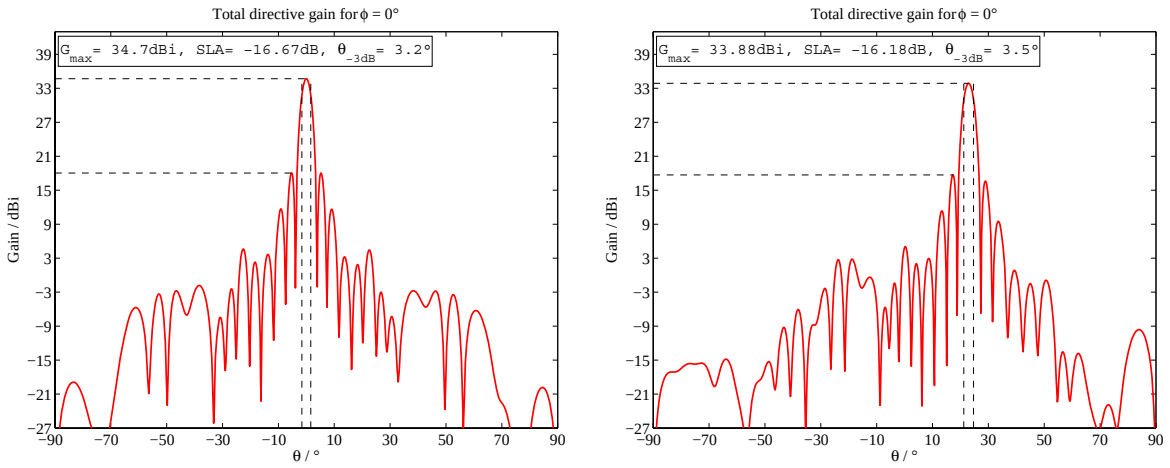

(a) $\theta = 0°$ (b) $\theta = 23°$

Fig. 6.14. Radiation pattern in side view for $\phi = 0°$ of an array with approximately 570 elements

below 45% of the needed elements compared to a completely filled array. Due to this the gain of the thinned array has to be expected to be about

$$a = 10\log_{10}\left(\frac{570}{720}\right) \approx 1\,dB \tag{6.9}$$

lower than of the completely filled array.

For further comparison an array with almost equal amount of elements (580) is afterwards presented, where the elements have been placed within a completely filled circular aperture.

By the aid of figure 6.15 one can compare the completely filled circular aperture array to the thinned array, with almost same amount of array elements, but significantly greater aperture. As predicted the simulated gain is almost equal due to an equal number of array elements. Additionally the beamwidth is almost the same, as the completely filled squared within the thinned circular aperture dictates with almost 80% the main spacing between the elements. The sidelobe attenuation of the completely filled circular aperture is as quoted earlier approximately 1 dB better than in the thinned array. Thus of course one should be advised to gain for a completely filled circular array, but nevertheless the potential of a thinned array should be considered.

The amount of added array elements and their placement in this example have been done intuitively and not been the result of an optimization as this is a very challenging aspect of array design and not been the scope for this thesis work. It should rather just present the potential of a thinned array in terms of improvement of beamwidth of the main lobe and significantly sidelobe attenuation while minimizing the efforts. As for a completely filled array the amount of elements increases with the aperture

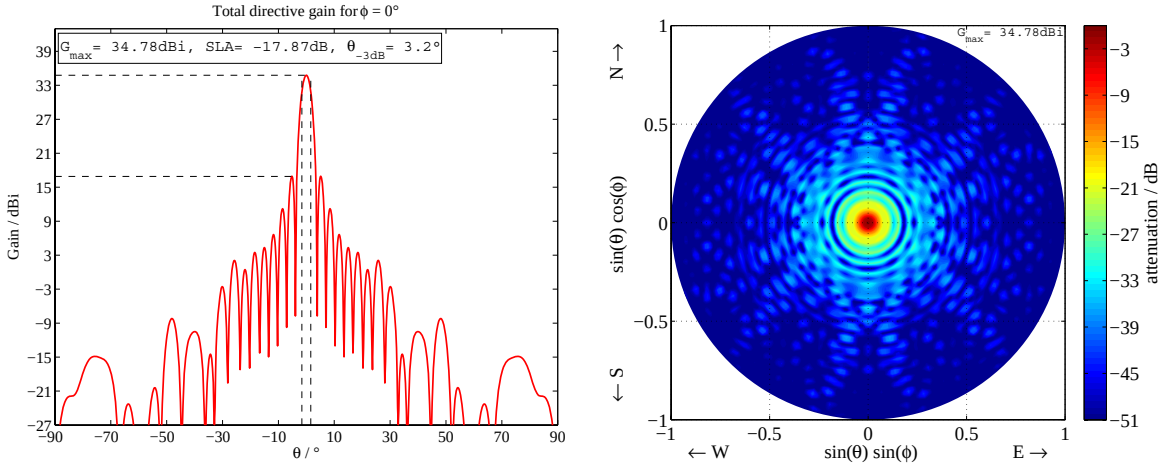

(a) Side view $\phi = 0°$ (b) Top view

Fig. 6.15. Radiation pattern for a circular aperture array with 580 elements

area and has thus square dependence, it seems very valuable to achieve e.g. an almost equal beamwidth with only linear increase of elements. Within an optimization process significantly better characteristics may be achieved than it is shown in figures 6.13 to 6.14.
The item of thinning an array is not only limited to the array antenna elements, furthermore the whole radar structure is directly affected. Thus a thinned array may significantly drop the efforts in terms of array costs due to decrease of e.g. transmit/receive-units, data acquisition, data transfer network, not to forget the necessary mechanical array building time and complexity of the control system.

6.5 Planar array of 1100 elements

In this section one of the most complex and simulation time consuming models is evaluated.
Several different models with the amount of approximately 1100 array elements have been simulated for various spacings and alignment of the elements.

The first model is presented in figure 6.16, with the general structure of the array that is used (figure 6.16(a)), actually depicted for a spacing d of almost 0.7λ on an equilateral grid and thus built by 31 columns and 36 rows.

Figure 6.16(b) shows the resulting radiation pattern in top view for a uniform illumination.

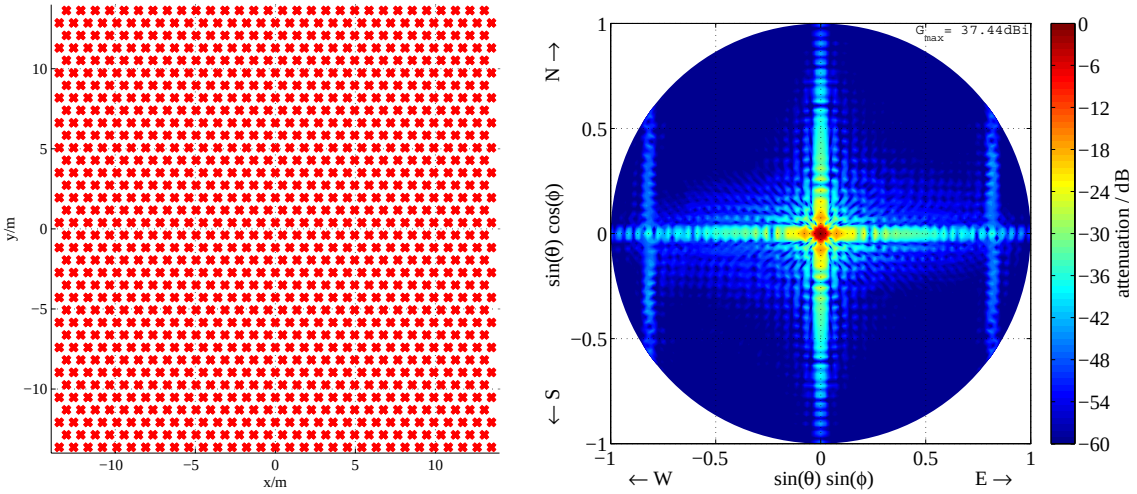

(a) Array geometry (b) Radiation pattern, top view

Fig. 6.16. Array of 1100 elements

Same radiation characteristics due to the squared aperture and equilateral grid structure, as presented earlier in the smaller structures, are recognizable. The suggestions made in earlier sections to improve the radiation pattern in terms of sidelobe distribution and attenuation are equally valid for the herein evaluated model.
The gain of the array due to the amount of elements may be estimated to approximately 37.5 dBi, which is achieved and underlined well in the radiation pattern.
Figure 6.17 presents the radiation pattern of the array with beam-forming at off-zenith angle $\theta = 40°$ for a spacing of approximately $d = 0.7\lambda$ and $d = 0.75\lambda$.

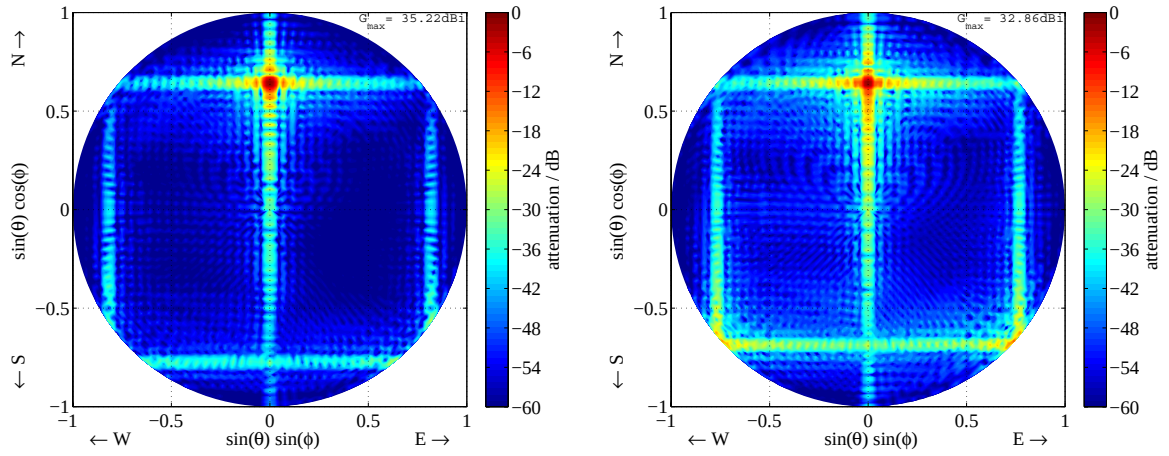

(a) Spacing $d = 0.7\lambda$ (b) Spacing $d = 0.75\lambda$

Fig. 6.17. Radiation pattern in top view of an array of 1100 elements for $\phi = 0°$, main beam at $\theta = 40°$

In figure 6.17 one clearly sees the introduction of 2 grating lobes, which is underlined

by the approach of their sidelobes evoked by the squared aperture. As an off-zenith beaming to $\theta = 40°$ is wanted without evoking grating lobes a spacing significantly greater than $d = 0.7\lambda$ should not be used.
Figure 6.18 respectively shows the side view pattern in form of cross section $\phi = 0°$ where the approach of the grating lobe sidelobes can qualitatively be proved.
Additional radiation pattern for spacings of $d = 0.6\lambda$ up to $d = 0.8\lambda$ are shown in the appendix and on the attached CD.

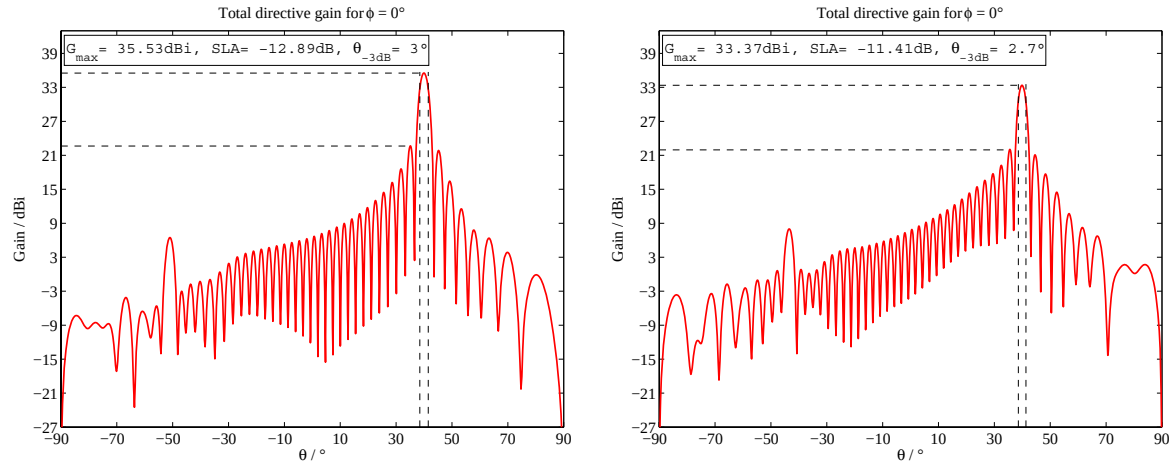

(a) Spacing $d = 0.7\lambda$ (b) Spacing $d = 0.75\lambda$

Fig. 6.18. Radiation pattern in side view of an array of 1100 elements for $\phi = 0°$, main beam at $\theta = 40°$

6.5.1 Array with mechanically tilted antennas

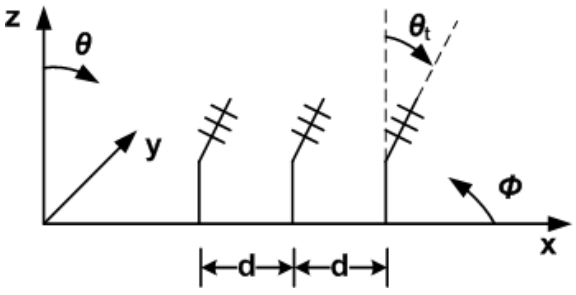

Fig. 6.19. Array elements oriented off-zenith

In the section 5 has been pointed out, mechanically tilted antennas, e.g. aligned to $\theta_t = 23°$ show higher mutual coupling than equally zenith aligned array elements. However, as it is an interesting and partially advantageous idea, simulation results of such

an array structure shall be presented.
The main advantage of arranging the array elements tilted to an off-zenith direction is achieving the maximum directivity of the array in the specific chosen off-zenith direction.
Depending on the angular distance to the zenith the advantage becomes more or less significant. For a rather great angular distance to the zenith the achieved directivity for a tilted array becomes significant.
Figures 6.20 and 6.21 show radiation plots in top and side view for an array of 1100

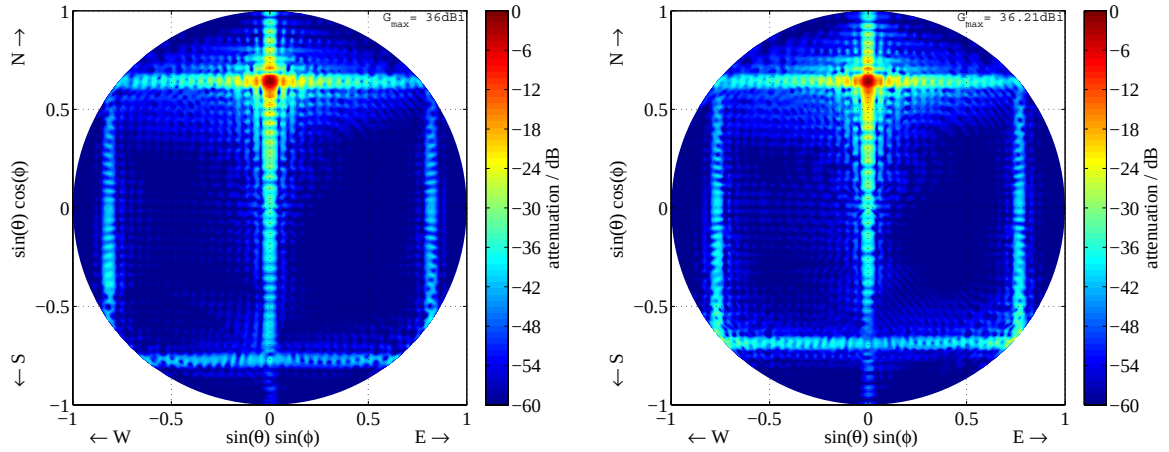

(a) Spacing $d = 0.7\lambda$ (b) Spacing $d = 0.75\lambda$

Fig. 6.20. Radiation pattern in top view for an array of 1100 tilted elements, main beam at $\theta = 40°$, $\phi = 0°$

tilted elements aligned to $\theta_t = 23°, \phi = 0°$, main beam formed at $\theta = 40°, \phi = 0°$ and compared with the same spacings as it's been evaluated right before.
As claimed earlier the array of tilted elements aligned to $\theta_t = 23°$ show higher gain for beam-forming at $\theta = 23°$ and $\theta = 40°$ compared to the zenith aligned elements, see figure 6.21 and 6.18. For $\theta = 40°$ the difference in gain appears to be 0.8 dB for beaming at $\theta = 23°$ and $\theta = 40°$ respectively.
Furthermore one may recognize a higher attenuation on the grating lobes sidelobe in directions of $\phi = 90...270°$ for elements tilted in opposite direction as for array elements aligned to zenith. This variation refers to the radiation pattern of the single element. The group characteristic of the array, formed by C_{g_r} and C_{g_c}, is unchanged for the array characteristic due to the similar amount and relative position of elements. However the element characteristic itself within the array characterisistic is angularly shifted by the degree of mechanical tilt, furthermore now asymmetric to zenith, determines the described additional attenuation.
This consequently results in variant radiation pattern with ϕ-dependency, which concerns the gain at a certain angular spot. Thus for equal off-zenith beaming various

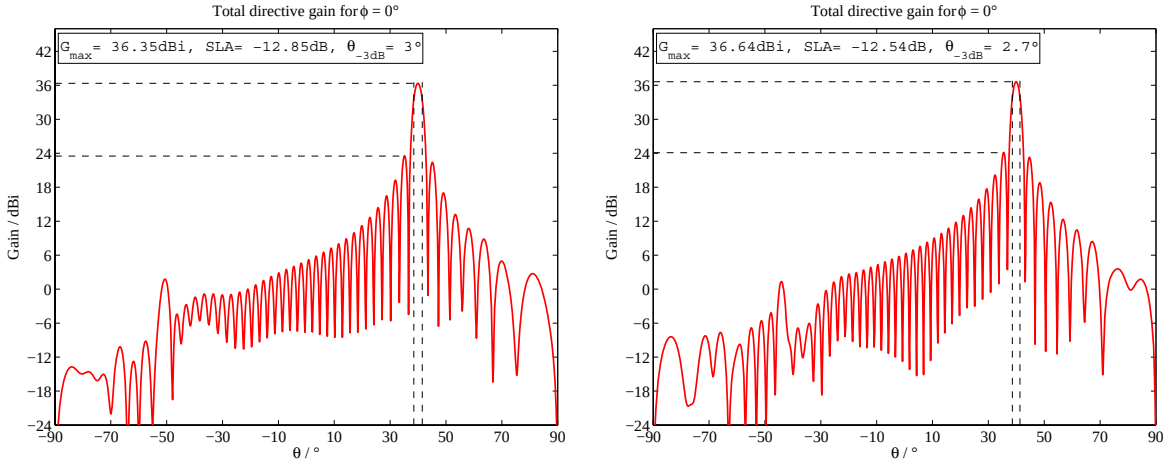

(a) Spacing $d = 0.7\lambda$ (b) Spacing $d = 0.75\lambda$

Fig. 6.21. Radiation pattern in side view of an array of 1100 tilted elements for $\phi = 0°$, main beam at $\theta = 40°$

azimuth-dependent directivity is evoked.

The directivity in the desired main direction ($\theta = 23°$) is improved by 0.8 dB (20%), compared to zenith aligned elements. However the additional effects of asymmetric azimuth-dependent pattern and significant increase of mutual coupling (section 5) are a high price for the additional gain.

6.6 Planar array of 2500 elements

This section evaluates the results of the largest model that have been simulated with NEC. Keeping the resolutions of the earlier models would lead to a total complexity of more than 100000 Segments, which is an extraordinary amount. Thus the model have been simplified in the first step to a limit of roughly 50000 Segments and finally to 45200 Segments to get contemporary results.

The model consists of a general structure as shown in figure 6.16(a) but with 47 rows and 54 columns instead. Figure 6.22 presents the resulting radiation pattern in top view.
In both parts of the figure, the sidelobes, due to squared aperture, evoked by grating lobes, are superposed severely in the axis of $\phi = 90°$ relative to the main lobe on both sides of the main lobe. The derived attenuation to these superposed sidelobe spots is only -9.4 dB which seems to be unbelievable low.

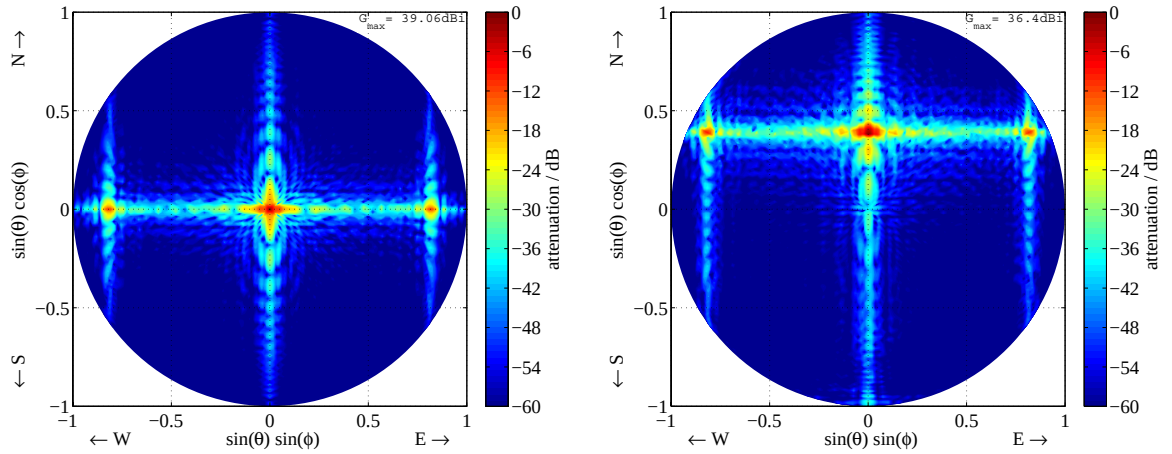

(a) Elements and main beam aligned to zenith (b) Elements and main beam aligned to $\theta = 23°$

Fig. 6.22. Radiation pattern in top view for an array of 2500 elements

Additional remarkable is the gain drop from figure 6.22(a) when main beam is formed at zenith to figure 6.22(b) with main beam formed at $\theta = 23°$ of 2.6 dB. Even in the raw data for the cross sections $\phi = 0°$ one can only see a gain of roughly 36.7 dBi. This results in a untypical degradation of almost 2.4 dB for the beam forming 23° from the broadside. Typically less than 1 dB loss have been evaluated in the earlier models for this angular difference of the main beam. This enormous abnormality seems to be the result of decreasing the model accuracy by a factor of 0.64 to the earlier evaluated array of 1100 elements, while the gain in figure 6.22(a) is still rather plausible, but the off-zenith bearing is definitely faulty.

According to equation 2.21 one may calculate for this array a half-power beamwidth of

$$\theta_3 = \arcsin\left(0.886 \cdot \frac{1.2757\,m}{42.3\,m}\right) \approx 1.53° \tag{6.10}$$

and futhermore with the relative amount of elements and the gain of the single element one may estimate the gain of the array to

$$g = (10\log_{10}(2100))\,dBi + 7\,dBi \approx 40.2\,dBi \tag{6.11}$$

which is not really fitting but is still rather close to the low accuracy NEC model with main beam evoked in zenith than for the off-zenith beaming.

Due to this results no further models with 2500 elements or more have been evaluated with NEC, as the simplified models yet needed a calculation time of more than 2 days on the IAPs mainframe.

6.7 Planar array of 10000 elements

In this section the planar array with the total number of 10000 elements is evaluated.

As shown before, it turned out that any simulation with NEC of an array composed of 10000 elements, especially as crossed single elements, is currently far out of any possibility. Thus it had to be decided to abstain from NEC simulations including its mutual coupling and edge effect consideration. Alternatively the superposition described in section 2.7.1 has been used to derive the radiation pattern for beam-forming at zenith and off-zenith angles.
For the calculation of the overall pattern the surface radiation pattern of the single array element has been simulated by NEC. The resulting raw data by NEC have been imported as $C_e(\phi, \theta)$, introduced in section 2.7.1 as characteristic of the single element, and multiplied by the array characteristic $C_a(\phi, \theta)$. The array characteristics have been calculated under the parameters of the amount of 100 single elements each column and row with a spacing of 0.7λ, the necessary phase-offset for off-boresight beamforming and the gain correction as introduced in section 4.9.
To enhance the accuracy for the superposition it has been tried to use NEC-computed radiation pattern of smaller arrays. However the resulting superposed radiation pattern of the NEC-computed arrays show severe in reality nonexistent sidelobes. These sidelobes are introduced due to the considered spacing in the superposition equation 2.84. Therefore in the following results the radiation pattern of the single array element have been superposed.
The results from the calculations of superposition equation are shown in figure 6.23 to

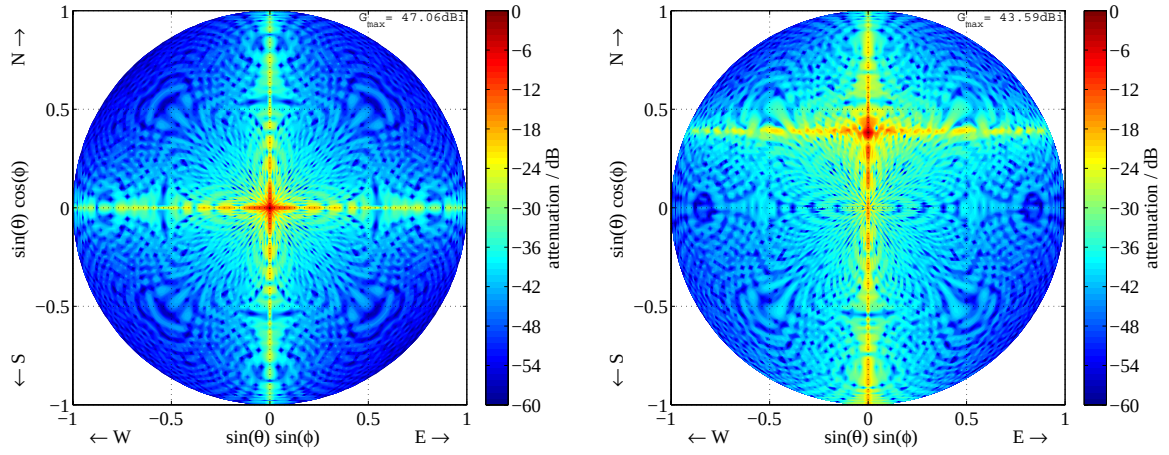

(a) Top view, main beam at $\theta = 0°$ (b) Top view, main beam at $\theta = 23°$

Fig. 6.23. Radiation pattern in top view for an array of 10000 elements

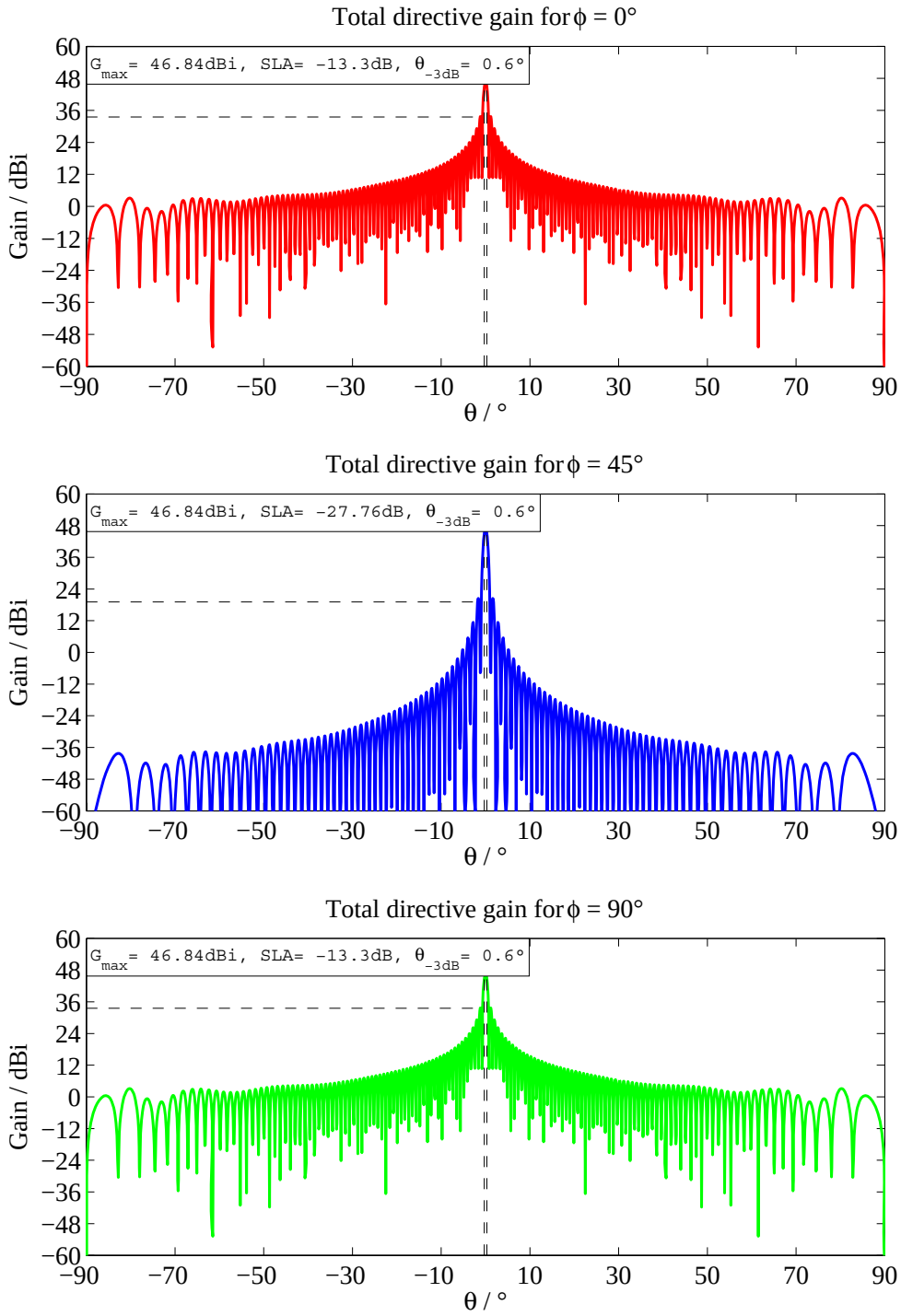

Fig. 6.24. Radiation pattern in side view for a planar array of 10000 elements, main beam at $\theta = 0°$

6.25. Figure 6.23 depicts the radiation pattern in top view with main beam at broadside and formed 23° off-zenith. In the pattern the crossed sidelobes can be seen, which are evoked due to the rectangular aperture.
Figure 6.24 depicts the resulting radiation pattern in the three cross sections $\phi = 0°$, $\phi = 45°$ and $\phi = 90°$ for an uniformly illuminated array of 10000 elements, resulting in an main lobe evoked at broadside.
The gain of 46.84 dB shown in the figure is quite similar to the estimates earlier made. However the half-power beamwidth of 0.6° is too few, the reason has been explained earlier.
The resulting beamwidth can be estimated by equation 2.21 analogically to section 6.1 and leads to

$$\theta_3 = \arcsin(0.01238132) \approx 0.71° \tag{6.12}$$

The result of the superposition shows realistic gain of the maximum, correct positions of nulls in the pattern and a sidelobe attenuation according to section 2.2.
The attenuation on the first sidelobe of 13.3 dB as depicted in the figure corresponds to the earlier evaluated characteristics.
The radiation pattern resulted from the superposition of 10000 array elements with phase- or time-delay to evoke the main beam at a zenith angle $\theta = 23°$ and is shown in figure 6.25.

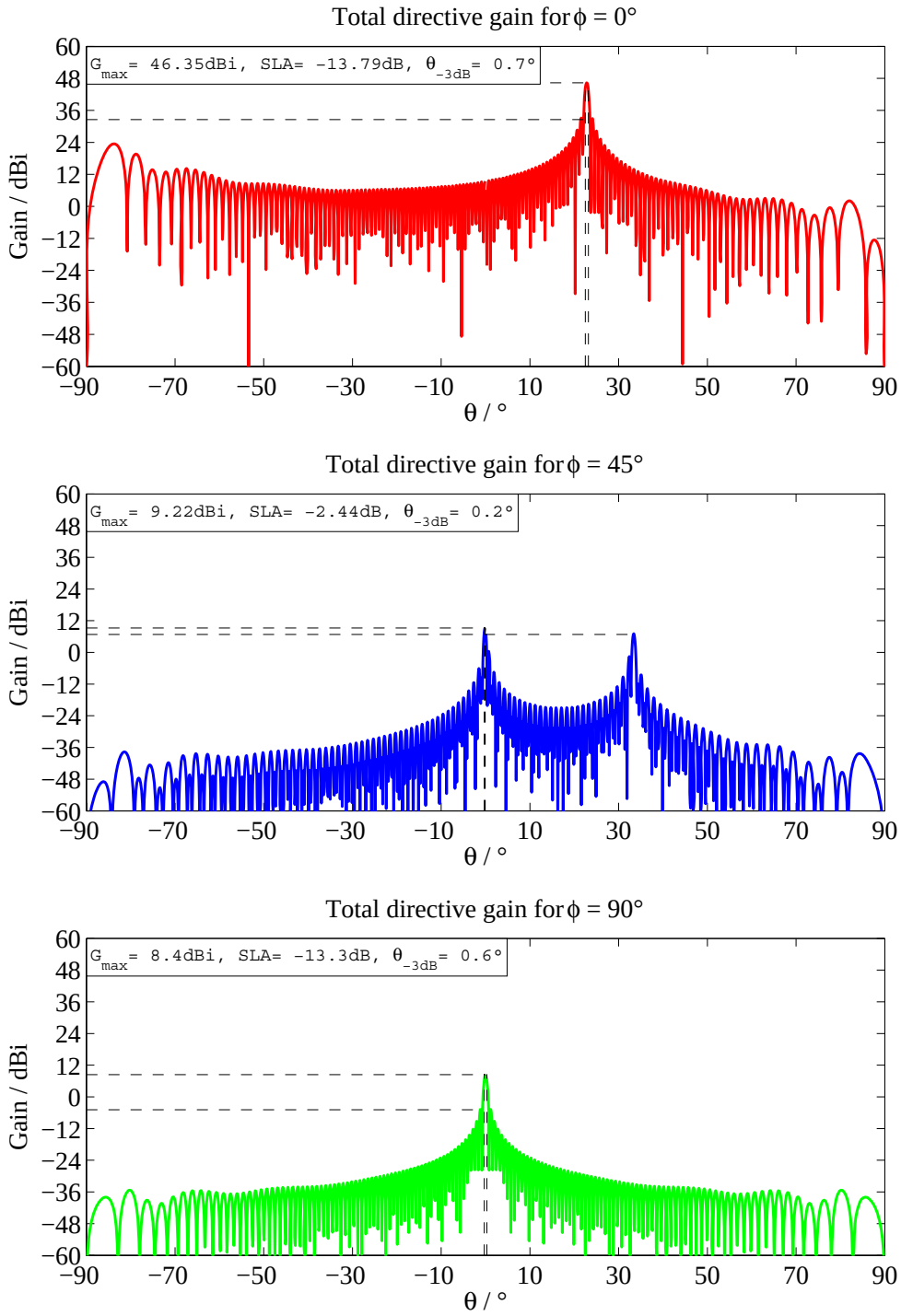

Fig. 6.25. Radiation pattern in side view for a planar array of 10000 elements, main beam at $\theta = 23°$

Chapter 7

Summary

In this thesis work the array structure and its individual array element have been evaluated in respect of the requirements for the planned EISCAT_3D.

7.1 Characteristics of the chosen individual array element

In chapter 4 the individual antenna, planned to be used in the array, has been evaluated for the frequency 235 MHz.
Three different designs for the potential single array element have been created with respect to the given requirements:

- Feed-point impedance 50+j0 ohms at center frequency

The chosen individual array element has an impedance $z = (200 + j0)\,\Omega$ at the center frequency, which may be transformed to $Z = 50\,\Omega$ by a half-wave balun, as described in section 4.3.

- Gain at angles $> 75°$ off-boresight as low as possible, but at least -16 dB

In the design tasks the gain for greater zenith angles ($> 75°$) shall be attenuated by at least 16 dB. The requirement of such high attenuation couldn't be realized with any of the evaluated designs.
This is related to the amount of elements of each single array element and thus its complexity. With a small and rather simple 3-element yagi antenna no deep nulls can be evoked in the pattern. A possible solution would be the use of a 4- or even more element yagi antenna. On the other hand a more complex and thus also more focussing antenna would lead to narrowing the half-power beamwidth associated with a higher attenuation at off-zenith angle, which is unwanted as it is still in the important scan angle range.
The highest attenuation on the radiation at $\theta = 75°$ could be reached to 7.8 dB, which is clearly less than originally required.

- Maximum relative gain at 40° off-boresight

The earlier requirement for high attenuation for zenith angles greater than $> 75°$ is contrary to the demand of low attenuation within angles 40° off zenith. An attenuation of 2.5 dB relative to the maximum gain could be achieved, which is yet significant. Considering an even more complex antenna structure and reducing the half-power beamwidth, as it might be claimed due higher necessary attenuation at $> 75°$, would lead to a far higher attenuation at 40°. Thus both requirements are directly contrary. Additionally it has to be quoted that the bandwidth of an antenna is also connected to the directivity. For highly optimized yagi antennas the bandwidth is reduced, which is obviously not wanted either.

- Bandwidth (specified as $s_{11} <$ -20 dB) > +/- 6 MHz

The bandwidth required in the design tasks for the single array element of ± 6 MHz could be realized and even improved to $+11.25$ MHz and -12.75 MHz respectively with the design, presented in section 4.1.2, due to its folded dipole. Thus the required bandwidth could be expanded to almost the double, which employs the possibility of broadband usage and provides an additional immunity to a weather-related resonance shift.

- Element lengths $< 0.4\lambda$ while maintaining all other characteristics

The requirement for the design process, limiting the size of the element for the individual antenna to less than 0.4λ, could not be reached with the finally chosen antenna. It has been achieved to reduce the length of each element by thickening. Each element has been designed with a diameter of 20 mm, which is considering the wavelength, quite a lot. However the resulting length of the antenna element has still been above 0.4λ. Therefore a design with angulated elements has been created and thus the needed radius around the antenna boom for the elements could be reduced below 0.4λ. Unfortunately this design could not really achieve any of the other requirements and thus had to be declined. The other designs need a radius of approximately 0.52λ for the reflector.

- Circularity better than -1 dB out to 30° off-boresight, in all azimuth directions and over full bandwidth,

It could be simulated that the polarization vector changes in phase for $\theta = 0°$ by up to 4%, however for off-zenith $\theta = 30°$ the polarization vector mutates up to 6.5%. These results appear very uncritical.

Additional criteria have been a good front/back-ratio, which the design with angulated element could not satisfy.

Out of the best compromise of all required parameters the design with a folded dipole, presented in section 4.1.2 has been chosen.

7.2 Results of the mutual coupling examination

After the selection of the single array element, the grid structure for the arrangement of the array elements has been studied.

An equilateral grid structure provides an extended angular range for beamforming without evoking grating lobes (section 2.4).
Using a squared grid structure and forming the main beam at $\theta = 40°$ without generation of grating lobes would need a narrow spacing of the array elements of maximum 0.6λ resulting in a higher mutual coupling between the elements. For an equilateral grid a spacing of 0.7λ can be used without introduction of any grating lobes.
Therefore simulations of mutual coupling for various orientations of the chosen single array element and different grid structure are discussed in chapter 5.
The results have shown a significant higher coupling for 23° tilted array elements, as it has been proposed in the thesis tasks. Due to this high mutual coupling it is recommended to dismiss the initially planned structure of tilted elements. The possible increase of gain by 0.8 dB, due to tilting the array elements in the desired main direction would lead to an at least 10 dB higher mutual coupling of the array and furthermore to a recognizable mutation of impedance.
Advantageous appeared the alignment of the single array elements on an equilateral grid structure, as the coupling rates between the elements have been more equal than in a square grid structure, where the single array elements have different spacings to its eight neighboring antennas.

The azimuthal orientation of the single array elements for $\phi_e = 45$ and $\phi_e = 60$ did not show significant differences in the coupling rates and thus both may be used. However an orientation of the elements $\phi_e = 0°$ should not be considered as it yet has shown significant varying coupling rates for a squared grid structure.

Summarizing the results of mutual coupling, the chosen array elements placed on a equilateral grid structure and oriented vertical to zenith with elements aligned to either $\phi = 45°$ or $\phi = 60°$ show in general the lowest mutual coupling. Spacings of 0.65λ to 0.75λ should be preferred.

7.3 Optimum array structure

Finally various array models have been simulated for different amount of array elements and various array structures. Within the NEC-models the influences of grid structure and array aperture to the radiation characteristics have been evaluated.
In section 2.2 and 2.7.6 the attenuation of the first sidelobe has been evaluated. The result of this evaluations led to the profitable structure of a circular aperture, as the sidelobe attenuation is improved by more than 4 dB. Additionally this array aperture evokes an equal radiation pattern for every azimuthal angle for a given zenith angle.

The previously derived results could be proved within the presented array models.

The desired maximum off-zenith beamforming of $\theta = 40°$ may be achieved without any direct grating lobe introduction above the horizon for an element spacing of 0.7λ.
However sidelobes, induced by the closest grating lobes, even if grating lobes are still not emitted, may be detected within the radiation pattern. However the influence of these grating lobe induced sidelobes can be limited by using a circular aperture and thus limiting the sidelobes. This is evaluated in section 6.3 and resulting radiation pattern are shown in figures 6.8(a) and 6.8(b).
Furthermore it has been shown, that for a circular aperture also a circular main beam is evoked, which therefore leads to a cylindrical or accurately cone shape of volume in the atmosphere instead of a frustum of a pyramid for a squared aperture.

In case of practical limits for the realization of the array, leading to the need to establish a rectangular or squared aperture, it is however recommended to create a circular aperture by the aid of a thinned array, as it is presented in section 6.4. In this case an additional evaluation of this challenging theme with an optimization of array elements placing has to be investigated in greater detail.

In section 6.3.1 it could be proved that the required weather immunity (3 mm sweet-water ice sheet on the elements) for an array with the chosen single array element is achieved.
No significant deterioration of the radiation pattern have been discovered.

At least it has to be quoted that the planned simulation of the whole array, consisting of 10000 elements, could not be realized with NEC. However the main determining parameters of the array could be derived within the above mentioned smaller models. Nevertheless it has to be quoted that only minor influence due to mutual coupling and edge effects for a such large array are to be expected, which could also be seen in the

greater NEC models. Therefore the results of the superposition for an array of 10000 element appears to be plausible.
For an array of approximately 10000 elements one can anticipate almost 47 dBi gain and a half-power beamwidth of at least $\theta_3 = 0.71°$.
Considering an element spacing $d = 0.7\lambda$ the array with the claimed parameters would require an area of approximately $8100\,m^2$. Additionally one has to be aware of the increase of array elements by 15% due to the equilateral structure, however as it has been pointed out above that the required parameters cannot be achieved without this effort.

Appendix A

Figures and tables

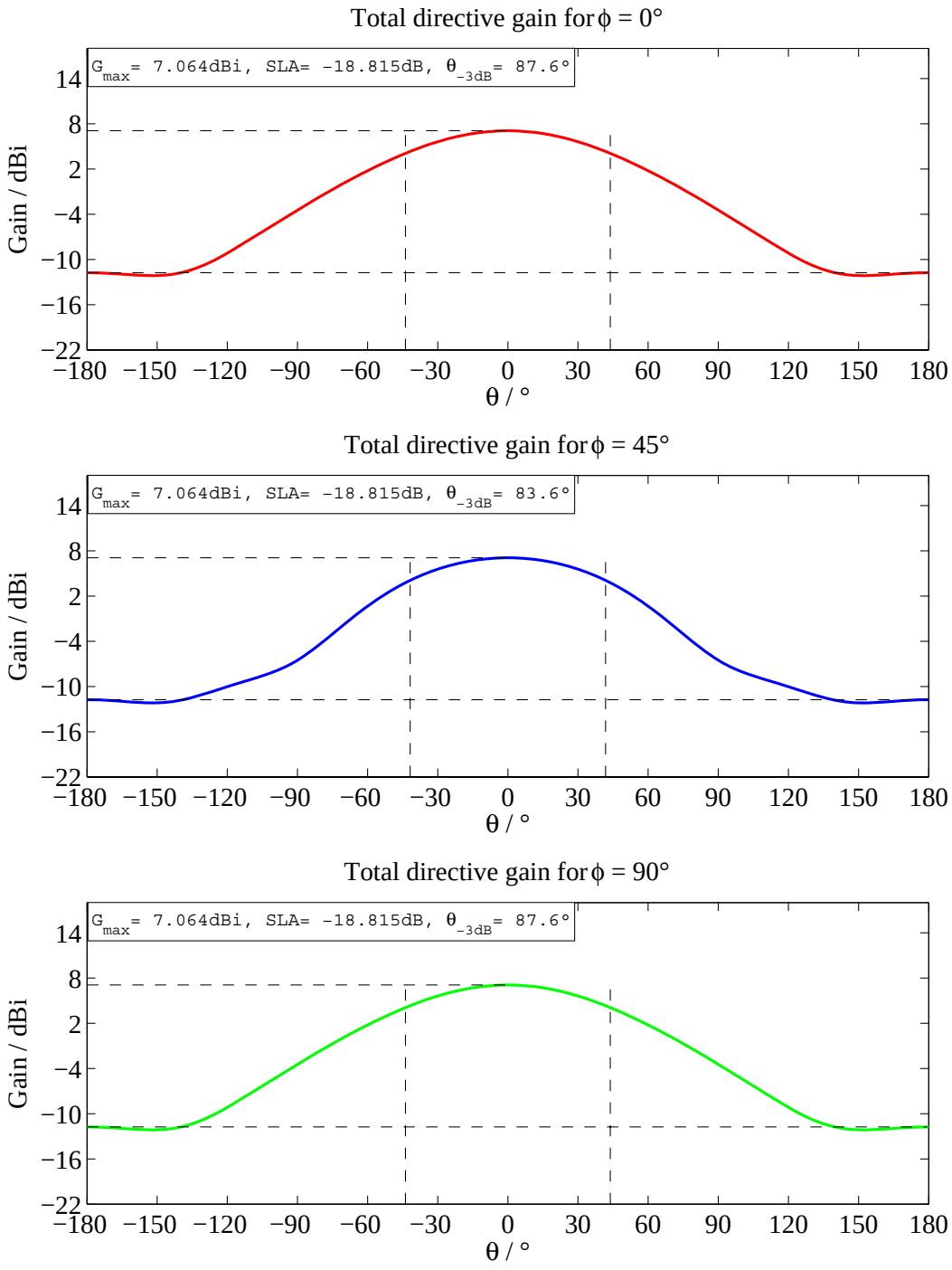

Fig. A.1. Radiation pattern of yagi design with a folded dipole

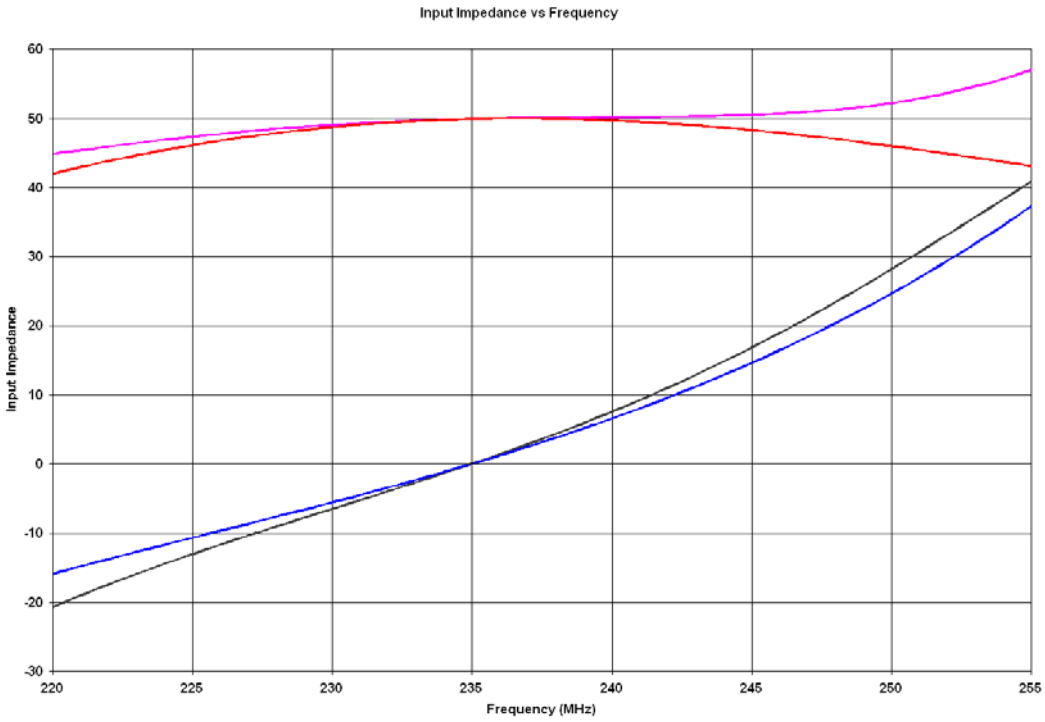

Fig. A.2. Impedance and phase of a yagi with straight dipole

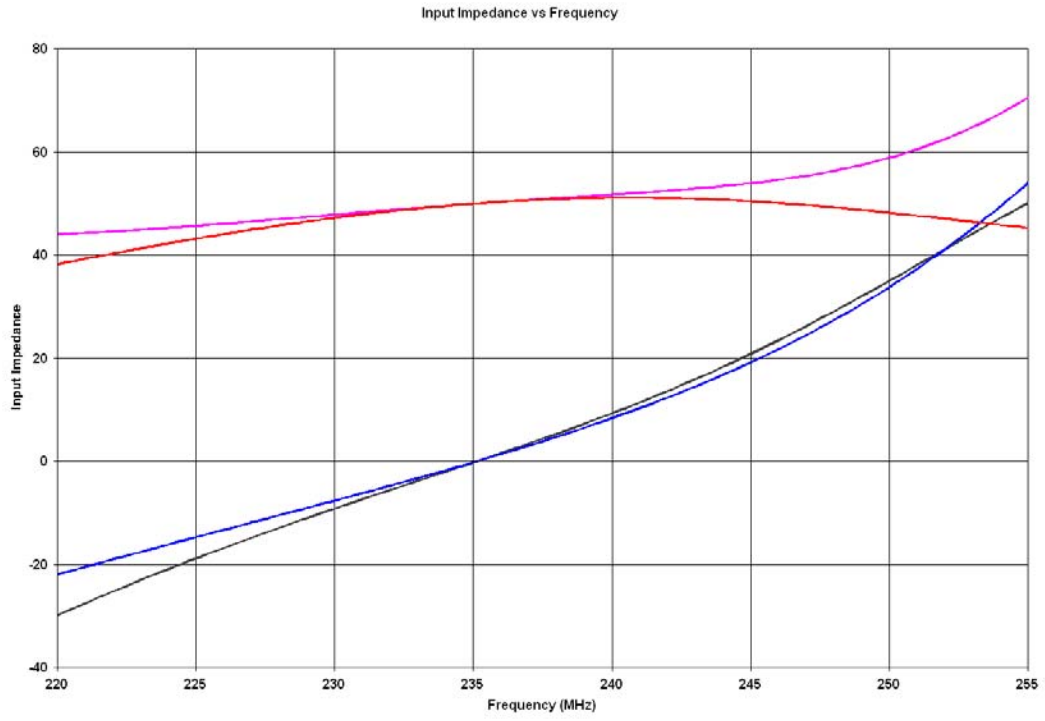

Fig. A.3. Impedance and phase of yagi design with angulated elements

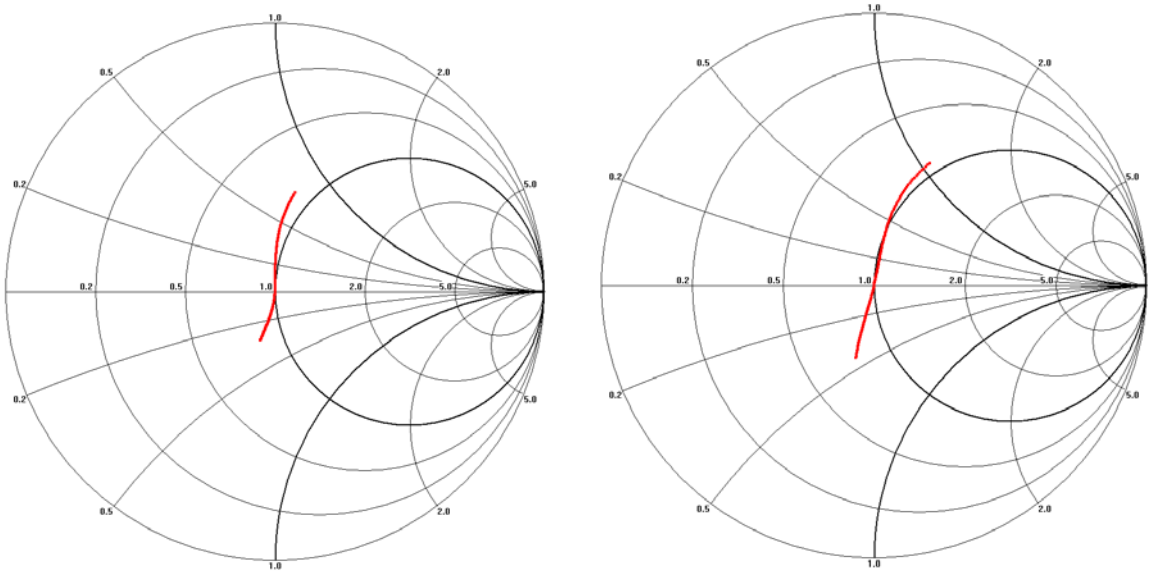

(a) Yagi design with straight dipole (b) Yagi design with angulated elements

Fig. A.4. Impedance Smith-Charts of the single antennas

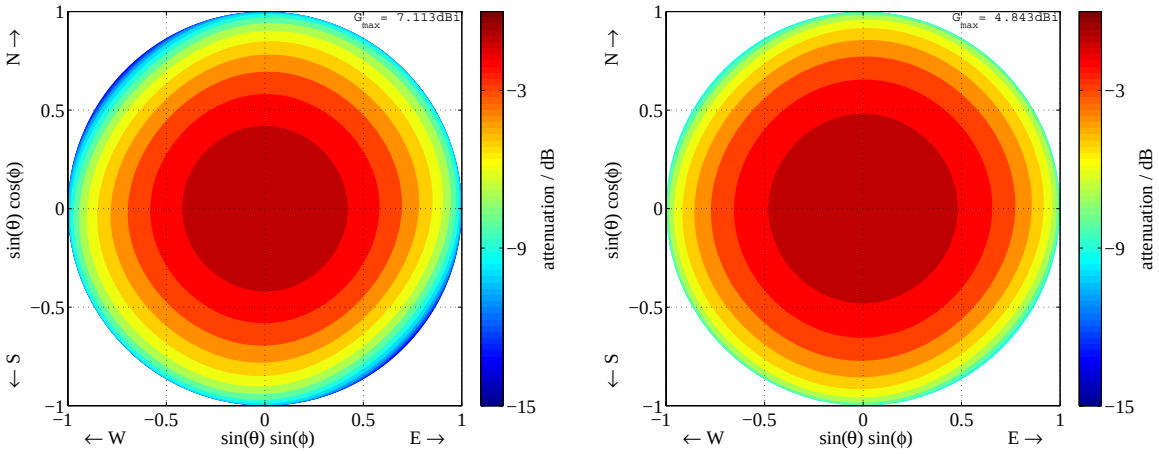

(a) Yagi design with straight dipole (b) Yagi design with angulated elements

Fig. A.5. Radiation pattern in top view of the single antennas

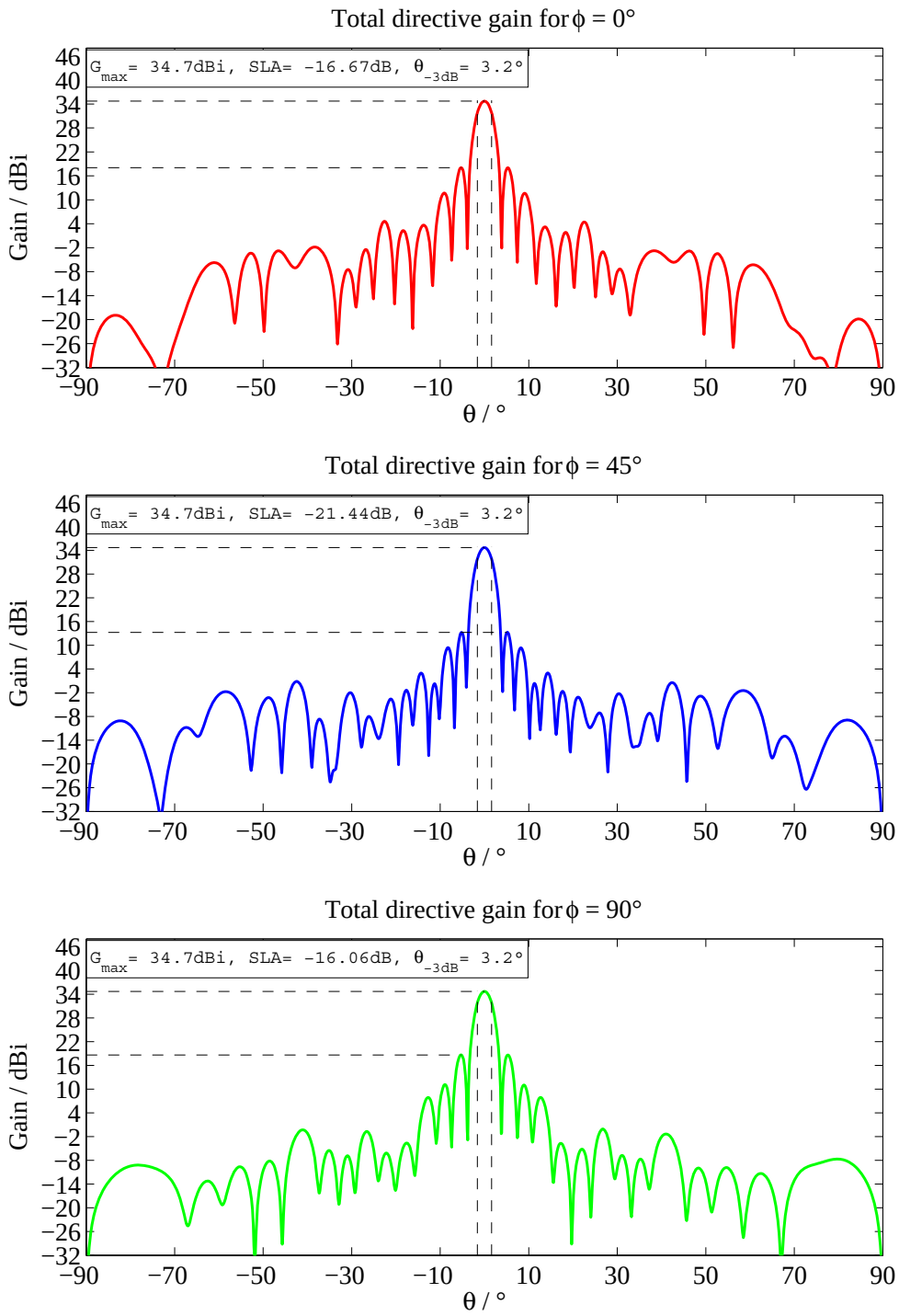

Fig. A.6. Radiation pattern in side view of a circular thinned 569 element array

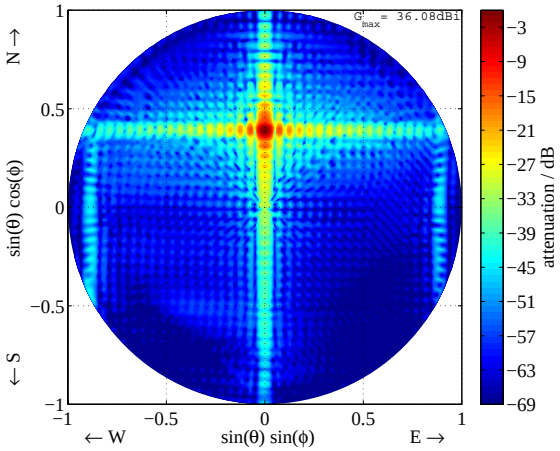

(a) Main beam at $\theta = 23°$

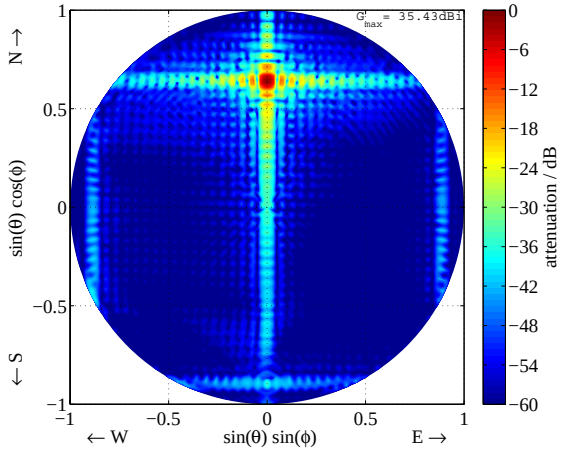

(b) Main beam at $\theta = 40°$

Fig. A.7. Radiation pattern in top view of an array of 1100 tilted elements for a spacing $d = 0.6\lambda$

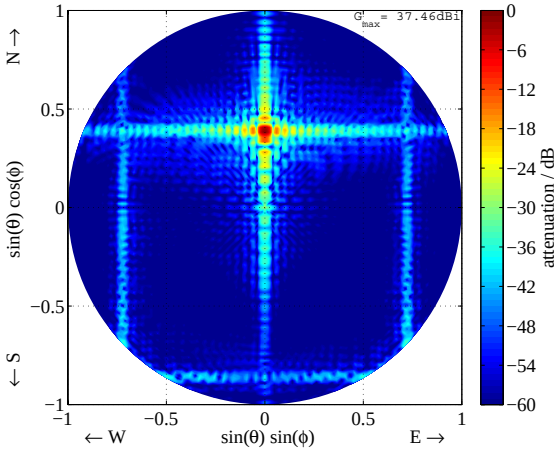

(a) Main beam at $\theta = 23°$

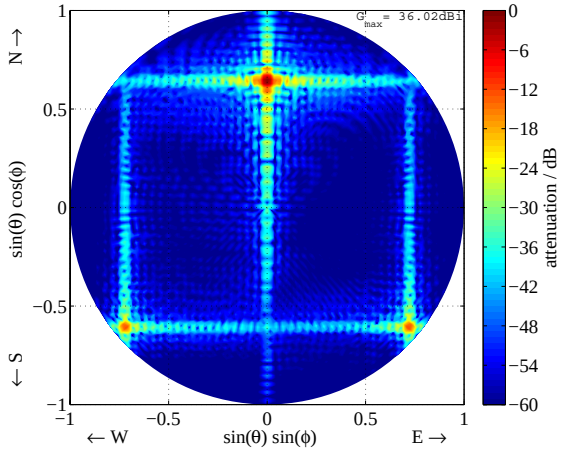

(b) Main beam at $\theta = 40°$

Fig. A.8. Radiation pattern in top view of an array of 1100 tilted elements for a spacing $d = 0.8\lambda$

Tab. A.1. Mutual coupling for squared grid, elements oriented to $\phi = 0°$

spacing	element	c_{fs}	element	c_{fs}	element	c_{fs}
0.6 λ	1	-45.3 dB	3	-36.2 dB	5	-49.1 dB
	2	-49.1 dB	4	-35.7 dB	6	-40.6 dB
	7	-35.7 dB	9	-	11	-35.7 dB
	8	-36.2 dB	10	-	12	-36.2 dB
	13	-49.1 dB	15	-36.2 dB	17	-45.3 dB
	14	-40.6 dB	16	-35.7 dB	18	-49.1 dB
0.65 λ	1	-52.4 dB	3	-38.5 dB	5	-51.2 dB
	2	-52.2 dB	4	-44.0 dB	6	-47.5 dB
	7	-44.2 dB	9	-	11	-44.2 dB
	8	-38.3 dB	10	-	12	-38.3 dB
	13	-51.2 dB	15	-38.5 dB	17	-52.4 dB
	14	-47.5 dB	16	-44.0 dB	18	-52.2 dB
0.7 λ	1	-60.5 dB	3	-40.0 dB	5	-53.7 dB
	2	-53.8 dB	4	-51.2 dB	6	-55.4 dB
	7	-51.4 dB	9	-	11	-51.4 dB
	8	-39.8 dB	10	-	12	-39.8 dB
	13	-53.7 dB	15	-40.0 dB	17	-60.5 dB
	14	-55.4 dB	16	-51.2 dB	18	-53.8 dB
0.75 λ	1	-69.6 dB	3	-40.1 dB	5	-54.7 dB
	2	-54.7 dB	4	-52.8 dB	6	-62.3 dB
	7	-53.2 dB	9	-	11	-53.2 dB
	8	-39.8 dB	10	-	12	-39.8 dB
	13	-54.7 dB	15	-40.1 dB	17	-69.6 dB
	14	-62.3 dB	16	-62.3 dB	18	-52.8 dB

Tab. A.2. Mutual coupling for squared grid, elements oriented to $\phi = 45°$

spacing	element	c_{fs}	element	c_{fs}	element	c_{fs}
0.6 λ	1	-52.7 dB	3	-48.2 dB	5	-43.2 dB
	2	-44.0 dB	4	-34.2 dB	6	-55.5 dB
	7	-32.6,dB	9	-	11	-32.6 dB
	8	-45.1 dB	10	-	12	-45.1 dB
	13	-43.7 dB	15	-48.2 dB	17	-52.7 dB
	14	-55.5 dB	16	-34.2 dB	18	-44.0 dB
0.65 λ	1	-56.5 dB	3	-51.6 dB	5	-47.0 dB
	2	-47.7 dB	4	-37.3 dB	6	-57.9 dB
	7	-35.5 dB	9	-	11	-35.5 dB
	8	-46.4 dB	10	-	12	-46.4 dB
	13	-47.0 dB	15	-51.6 dB	17	-56.5 dB
	14	-57.9 dB	16	-37.3 dB	18	-47.7 dB
0.7 λ	1	-60.2 dB	3	-54.9 dB	5	-52.0 dB
	2	-52.7 dB	4	-41.4 dB	6	-60.5 dB
	7	-39.0 dB	9	-	11	-39.0 dB
	8	-47.2 dB	10	-	12	-47.2 dB
	13	-52.0 dB	15	-54.9 dB	17	-60.2 dB
	14	-60.5 dB	16	-41.4 dB	18	-52.7 dB
0.75 λ	1	-62.9 dB	3	-55.0 dB	5	-55.8 dB
	2	-56.2 dB	4	-44.4 dB	6	-62.8 dB
	7	-41.1 dB	9	-	11	-41.1 dB
	8	-46.3 dB	10	-	12	-46.3 dB
	13	-55.8 dB	15	-55.0 dB	17	-62.9 dB
	14	-62.8 dB	16	-44.4 dB	18	-56.2 dB

Tab. A.3. Mutual coupling for equilateral grid, elements oriented to $\phi = 45°$

spacing	element	c_{fs}	c_{rg}	element	c_{fs}	c_{rg}
0.6 λ	1	-38.0 dB	-38.2 dB	3	-47.8 dB	-48.1 dB
	2	-40.9 dB	-41.1 dB	4	-37.0 dB	-37.1 dB
	5	-35.1 dB	-35.4 dB	9	-35.1 dB	-35.4 dB
	6	-51.1 dB	-51.3 dB	10	-51.1 dB	-51.3 dB
	11	-47.8 dB	-48.1 dB	13	-38.0 dB	-38.2 dB
	12	-37.0 dB	-37.1 dB	14	-40.9 dB	-41.1 dB
0.65 λ	1	-41.6 dB	-41.9 dB	3	-47.9 dB	-48.5 dB
	2	-42.2 dB	-42.6 dB	4	-40.0 dB	-40.1 dB
	5	-37.1 dB	-37.5 dB	9	-37.1 dB	-37.5 dB
	6	-59.6 dB	-59.9 dB	10	-59.6 dB	-59.9 dB
	11	-47.9 dB	-48.5 dB	13	-41.6 dB	-41.9 dB
	12	-40.0 dB	-40.1 dB	14	-42.2 dB	-42.6 dB
0.7 λ	1	-45.1 dB	-45.4 dB	3	-47.8 dB	-48.5 dB
	2	-44.0 dB	-44.6 dB	4	-43.3 dB	-43.4 dB
	5	-39.3 dB	-39.9 dB	9	-39.3 dB	-39.9 dB
	6	-65.0 dB	-61.7 dB	10	-65.0 dB	-61.7 dB
	11	-47.8 dB	-48.5 dB	13	-45.1 dB	-45.4 dB
	12	-43.3 dB	-43.4 dB	14	-44.0 dB	-44.6 dB
0.75 λ	1	-48.0 dB	-48.7 dB	3	-47.4 dB	-48.3 dB
	2	-45.7 dB	-46.3 dB	4	-46.5 dB	-46.4 dB
	5	-41.1 dB	-41.7 dB	9	-41.1 dB	-41.7 dB
	6	-60.6 dB	-60.0 dB	10	-60.6 dB	-60.0 dB
	11	-47.4 dB	-48.3 dB	13	-48.0 dB	-48.7 dB
	12	-46.5 dB	-46.4 dB	14	-45.7 dB	-46.3 dB

Tab. A.4. Mutual coupling for equilateral grid, elements oriented to $\phi = 60°$

spacing	element	c_{fs}	c_{rg}	element	c_{fs}	c_{rg}
0.6 λ	1	-33.9 dB	-34.1 dB	3	-56.3 dB	-56.9 dB
	2	-44.7 dB	-44.8 dB	4	-36.5 dB	-36.7 dB
	5	-36.2 dB	-36.5 dB	9	-36.2 dB	-36.5 dB
	6	-57.1 dB	-56.8 dB	10	-57.1 dB	-56.8 dB
	11	-56.3 dB	-56.9 dB	13	-33.9 dB	-34.1 dB
	12	-36.5 dB	-36.7 dB	14	-44.7 dB	-44.8 dB
0.65 λ	1	-38.1 dB	-38.5 dB	3	-56.5 dB	-56.9 dB
	2	-45.9 dB	46.3 dB	4	-38.8 dB	-39.0 dB
	5	-38.2 dB	-38.7 dB	9	-38.2 dB	-38.7 dB
	6	-60.5 dB	-60.3 dB	10	-60.5 dB	-60.3 dB
	11	-56.5 dB	-56.9 dB	13	-38.1 dB	-38.5 dB
	12	-38.8 dB	-39.0 dB	14	-45.9 dB	-46.3 dB
0.7 λ	1	-42.3 dB	-42.9 dB	3	-54.9 dB	-56.1 dB
	2	-47.3 dB	-47.9 dB	4	-41.3 dB	-41.5 dB
	5	-40.3 dB	-40.9 dB	9	-40.3 dB	-40.9 dB
	6	-64.1 dB	-61.1 dB	10	-64.1 dB	-61.1 dB
	11	-54.9 dB	-56.1 dB	13	-42.3 dB	-42.9 dB
	12	-41.3 dB	-41.5 dB	14	-47.3 dB	-47.9 dB
0.75 λ	1	-46.5 dB	-47.3 dB	3	-53.5 dB	-55.0 dB
	2	-48.4 dB	-49.2 dB	4	-43.8 dB	-43.7 dB
	5	-41.6 dB	-42.3 dB	9	-41.6 dB	-42.3 dB
	6	-63.1 dB	-59.7 dB	10	-63.1 dB	-59.7 dB
	11	-53.5 dB	-55.0 dB	13	-46.5 dB	-47.3 dB
	12	-43.8 dB	-43.7 dB	14	-48.4 dB	-49.2 dB

Tab. A.5. Mutual coupling for equilateral grid, elements oriented to $\phi = 45°$, tilted to $\theta = 23°$

spacing	element	c_{fs}	c_{rg}	element	c_{fs}	c_{rg}
0.6 λ	1	-39.9 dB	-40.1 dB	3	-42.7 dB	-43.0 dB
	2	-42.2 dB	-42.0 dB	4	-27.4 dB	-27.2 dB
	5	-42.4 dB	-42.4 dB	9	-21.1 dB	-20.6 dB
	6	-55.2 dB	-55.6 dB	10	-47.1 dB	-47.1,dB
	11	-43.5 dB	-43.8 dB	13	-37.5 dB	-35.6 dB
	12	-33.9 dB	-33.8 dB	14	-38.8 dB	-38.9 dB
0.65 λ	1	-45.4 dB	-45.9 dB	3	-43.2 dB	-42.0 dB
	2	-46.4 dB	46.2 dB	4	-32.9 dB	-32.4,dB
	5	-48.4 dB	-48.8 dB	9	-23.2 dB	-22.0 dB
	6	-63.2 dB	-60.0 dB	10	-50.2 dB	-50.0 dB
	11	-50.7 dB	-51.7 dB	13	-40.1 dB	-39.7 dB
	12	-39.0 dB	-38.8 dB	14	-41.4 dB	-41.2 dB
0.7 λ	1	-50.7 dB	-50.2 dB	3	-44.2 dB	-41.5 dB
	2	-49.7 dB	-50.0 dB	4	-38.0 dB	-37.9 dB
	5	-51.4 dB	-52.2 dB	9	-25.7 dB	-23.7 dB
	6	-71.7 dB	-60.3 dB	10	-52.9 dB	-48.4,dB
	11	-56.4 dB	-55.6 dB	13	-42.7 dB	-42.3 dB
	12	-43.4 dB	-43.0 dB	14	-43.6 dB	-42.1 dB
0.75 λ	1	-52.2 dB	-51.6 dB	3	-45.4 dB	-41.1 dB
	2	-50.5 dB	-49.4 dB	4	-42.1 dB	-43.2 dB
	5	-51.0 dB	-50.1 dB	9	-28.2 dB	-25.3 dB
	6	-66.6 dB	-59.6 dB	10	-53.8 dB	-45.3 dB
	11	-52.2 dB	-50.7 dB	13	-45.4 dB	-45.1 dB
	12	-45.6 dB	-45.1 dB	14	-45.5 dB	-43.8 dB

Tab. A.6. Mutual coupling for equilateral grid, elements oriented to $\phi = 60°$, tilted to $\theta = 23°$

spacing	element	c_{fs}	c_{rg}	element	c_{fs}	c_{rg}
0.6 λ	1	-37.1 dB	-37.1 dB	3	-50.1 dB	-50.0 dB
	2	-46.0 dB	-45.5 dB	4	-25.6 dB	-25.0 dB
	5	-43.8 dB	-44.0 dB	9	-26.2 dB	-25.7 dB
	6	-62.3 dB	-61.3 dB	10	-41.5 dB	-39.7 dB
	11	-50.3 dB	-50.6 dB	13	-32.2 dB	-31.3 dB
	12	-34.0 dB	-34.1 dB	14	-39.5 dB	-39.6 dB
0.65 λ	1	-43.2 dB	-43.4 dB	3	-49.8 dB	-47.9 dB
	2	-49.8 dB	49.4 dB	4	-30.5 dB	-29.6,dB
	5	-49.9 dB	-50.2 dB	9	-27.0 dB	-25.8 dB
	6	-70.6 dB	-62.2 dB	10	-46.3 dB	-43.3 dB
	11	-55.3 dB	-55.3 dB	13	-37.5 dB	-37.2 dB
	12	-39.3 dB	-39.3 dB	14	-43.9 dB	-43.9 dB
0.7 λ	1	-48.6 dB	-49.4 dB	3	-50.3 dB	-46.5 dB
	2	-52.8 dB	-52.8 dB	4	-34.9 dB	-34.2 dB
	5	-52.3 dB	-53.0 dB	9	-28.3 dB	-26.2 dB
	6	-69.8 dB	-59.1 dB	10	-51.4 dB	-46.8,dB
	11	-55.2 dB	-54.7 dB	13	-40.2 dB	-39.9 dB
	12	-43.1 dB	-43.3 dB	14	-47.1 dB	-46.0 dB
0.75 λ	1	-51.3 dB	-50.7 dB	3	-51.2 dB	-45.4 dB
	2	-52.3 dB	-50.4 dB	4	-38.4 dB	-38.5 dB
	5	-50.9 dB	-50.2 dB	9	-29.6 dB	-26.7 dB
	6	-66.0 dB	-56.3 dB	10	-52.6 dB	-49.3 dB
	11	-52.9,dB	-51.4 dB	13	-42.9 dB	-42.8 dB
	12	-44.8 dB	-44.3 dB	14	-48.6 dB	-45.5 dB

References

[Bal05] Balanis, C. A.: *Antenna Theory*. 3. Auflage. John Wiley & Sons, 2005.

[Bor05] Borucki, L.: *Leistungsanpassung in der Funktechnik*. vth, 2005.

[DA89] Davis, J. L.; Annan, A. P.: Ground-penetrating radar for high-resolution mapping of soil and rock stratigraphy. *Geophysical Prospecting*, Bd. 37, 1989, S. 531–551.

[Dan96] Daniels, D. J.: Surface-penetrating radar. *Radar, Sonar, Navigation and Avionics*, Bd. 6, 1996, S. 320.

[EIS96] EISCAT: *EISCAT Scientific Association, Incoherent Scatter*. 1996.

[Goe01] Goebel, J.: *Radartechnik : Grundlagen und Anwendungen*. VDE Verlag, 2001.

[Gra95] Grayer, G.: *VHF/UHF DX Book*. DIR Publishing, 1995.

[Gro01] Gronau, G.: *Höchstfrequenztechnik : Grundlagen, Schaltungstechnik, Messtechnik, planare Antennen*. Bd. 1 der Reihe *1.* Springer, 2001.

[Han85] Hansen, R. C.: *Microwave Scanning Antennas*. Bd. 1. Peninsula Pubishing, 1985.

[HKH+97] Hagfors, T.; Kofman, W.; Huuskonen, A.; Lehtinen, M.; Schlegel, K.; Lockwood, M.; Kamide, Y.; Richmond, A. D.; Röttger, J.: *Incoherent Scatter; Theory, Practice and Science*. EISCAT Scientific Association, 1997.

[JJ93] Johnson, R. C.; Jasik, H.: *Antenna engineering handbook*. McGraw-Hill, 1993.

[Kar06] Kark, K.: *Elektromagnetische Wellen auf Leitungen, im Freiraum und ihre Abstrahlung*. Bd. 1. 2. Auflage. Vieweg, 2006.

[Kra88] Kraus, J. D.: *Antennas*. Mc Graw-Hill, 1988.

[LBM82] Loane, J. T.; Bowhill, S.; Mayes, P. E.: Feed system design and experimental results in the uhf models for the proposed urbana phased array. *Aeronomy Report*, Bd. 107, 1982.

[Lo93] Lo, Yuen T. ; Lee, S.-W.: *Antenna theory*. Bd. 2. Van Nostrand Reinhold, 1993.

[Mai94] Mailloux, R. J.: *Phased Array Antenna Handbook*. Bd. 1. 1. Auflage. Artech House London, 1994.

[MG86] Meinke, H.; Gundlach, F. W.: *Taschenbuch der Hochfrequenztechnik: Grundlagen*. Bd. 1. 4. Auflage. Berlin: Springer-Verlag, 1986.

[Ren06] Renkwitz, T.: *Entwicklung einer zirkular polarisierten Sendeantenne (53,5 MHz) mit Strahlungsmaxima bei Zenitwinkeln von etwa 15 - 60 und des erforderlichen Speisesystems*. Bachelor-Thesis, 2006.

[Rub98] Rubach, J.: Optimierung der phased-array antenne des st-radars in kühlungsborn für senkrechte und schräge abstrahlung. Diplomarbeit, University Rostock, 1998.

[Sko64] Skolnik, M. I.: Designed density-tapered arrays. *IEEE Trans.*, Bd. AP-12, 1964, S. 408–417.

[Sko70] Skolnik, M. I.: *Radar handbook*. McGraw-Hill, 1970.

[Ste73] Steinberg, B. D.: Comparison between the peak sidelobe of the random array and algorithmically designed aperiodic arrays. *IEEE*, Bd. AP-21, 1973, S. 366–369.

[Sti84] Stirner, E.: *Antennen, Grundlagen*. Bd. 1. 2. Auflage. Hüthig, 1984.

[TMB82] Tanner, D. R.; Mayes, P. E.; Bowhill, S.: Phased array design including consideration of mutual coupling with application to the urbana choherent-scatter radar. *Aeronomy Report*, Bd. 108, 1982.

[TP76] Tai, C.-T.; Pereira, C. S.: An approximate formula for calculating the directivity of an antenna. *IEEE Transactions On Antennas And Propagation*, Bd. 24, 1976, S. 235–236.

[ZB00] Zinke, O.; Brunswig, H.: *Lehrbuch der Hochfrequenztechnik: Hochfrequenzfilter, Leitungen, Antennen*. Bd. 1. 5. Auflage. Berlin: Springer-Verlag, 2000.

Acknowledgements

Finally I wish to thank Dr. Gudmund Wannberg from EISCAT for providing me this interesting and challenging subject for my Master of Science thesis and giving me the opportunity to take part in such an amazing project as EISCAT_3D definitely is.
Not less thanks are spread to Prof. Tobias Weber from University Rostock and Dr. Werner Singer from the Leibniz-Institute of Atmospheric Physics (IAP) who essentially supported this M. Sc. thesis.
Additional thanks are aimed to Prof. Anthony van Eyken (EISCAT) and Prof. Franz-Josef Lübken (IAP) who have been decisive involved making this thesis work possible.
Furthermore I have to thank the IAP in general for supporting this work and the department of radar sounding and sounding rockets in particular e.g. for providing the latest NEC simulation software package. Connected to this I have to thank the IAPs computer center, led by Thomas Linow, for providing access and support for the usage of the simulation software on IAPs scalar computer.
Thanks are especially addressed to Dr. Ralph Latteck and again Dr. Werner Singer for all their contribution.
Further thanks are directed to Dr. Norbert Engler from IAP for his TEX-support and Nico Palleit from University Rostock for his benefit on the way to and during this thesis work.
Last but not least of course special thanks to my family for permanent support!

Erklärung

Ich erkläre, diese Arbeit selbstständig angefertigt und die benutzten Unterlagen vollständig angegeben zu haben.

Rostock, 25. April 2008

Toralf Renkwitz